SYNTHESIS AND ELECTRIC FIELD-MANIPULATION OF

HIGH ASPECT RATIO BARIUM TITANATE

A Thesis

by

JUNJIA LI

Submitted to the Office of Graduate Studies of
Texas A&M University
in partial fulfillment of the requirements for the degree of

MASTER OF SCIENCE

May 2011

Major Subject: Aerospace Engineering

Synthesis and Electric Field-manipulation of High Aspect Ratio Barium Titanate

SYNTHESIS AND ELECTRIC FIELD-MANIPULATION OF

HIGH ASPECT RATIO BARIUM TITANATE

A Thesis

by

JUNJIA LI

Submitted to the Office of Graduate Studies of
Texas A&M University
in partial fulfillment of the requirements for the degree of

MASTER OF SCIENCE

Approved by:

Co-Chairs of Committee,	Zoubeida Ounaies
	Dimitris Lagoudas
Committee Members,	James Boyd
	Gregory Huff
Head of Department,	Dimitris Lagoudas

May 2011

Major Subject: Aerospace Engineering

ABSTRACT

Synthesis and Electric Field-Manipulation of High Aspect Ratio Barium Titanate.

(May 2011)

Junjia Li, B.S., Nanjing University;

M.S., Nanjing University

Co-Chairs of Advisory Committee: Dr. Zoubeida Ounaies
Dr. Dimitris Lagoudas

The objective of this thesis is to develop high dielectric constant nanoparticle dispersion for switchable aircraft antenna systems. Two steps were designed to achieve the objective. First, obtain high dielectric, high aspect ratio nanoparticles and disperse them in dielectric oil medium. Second, manipulate the particle-oil dispersion using an external alternating current (AC) electric field to increase the effective dielectric constant.

In order to obtain high dielectric dispersions, different sizes and shapes of titanium dioxide (TiO_2) and barium titanate ($BaTiO_3$) nanoparticles were purchased and measured. However, after a number of experiments detailed in the thesis, it was found that none of the commercially available nanoparticles could satisfy our requirements for a minimum effective dielectric constant. Thus, to achieve the goals above, we synthesized high aspect ratio $BaTiO_3$ nanowires with BaC_2O_4 and TiO_2 powders as precursors using a molten salt method. The as-synthesized $BaTiO_3$ nanowires were characterized using scanning electron microscopy (SEM), X-ray diffraction (XRD), and

energy dispersive spectroscopy (EDS) mapping. The nanowires have a diameter ranging from 100 nm to 300 nm, and their lengths range from 1.5 μm to 5 μm. Mechanical stirring and bath sonication were used to obtain even colloidal dispersions. Different concentrations of $BaTiO_3$ nanoparticles well dispersed in the oil medium were successfully manipulated using AC electric field. To monitor the change in microstructure of $BaTiO_3$ nanoparticles, optical microscopy was used to observe the alignment of particles in the sample under the applied electric field. Various parameters including the magnitude, frequency, and duration of the electric field, and the concentration of $BaTiO_3$ nanoparticles were investigated to achieve the optimal alignment of nanoparticles. The experimental results were validated by theoretical analysis using Maxwell-Garnett mixing rule. It was demonstrated that the effective dielectric constant of the colloidal dispersions would increase with the increase of the magnitude, frequency and duration of applied electric field. Synthesized $BaTiO_3$ nanowire-based dispersions exhibit significant enhancement of the effective dielectric constant compared to other colloidal materials. The effective dielectric constant of 5 wt% $BaTiO_3$-oil dispersions could reach up to 10 when aligned at 1000 V/mm electric field at 1 kHz frequency for 1 hour.

DEDICATION

To my wife and my parents

vi

ACKNOWLEDGEMENTS

I would like to acknowledge several people for their help in completing this thesis. First and foremost, I would like to thank my research co-advisors, Dr. Zoubeida Ounaies and Dr. Dimitris Lagoudas, for the guidance, advice, discussion and support given in the past two years. I am very grateful for their encouragement during some very trying times of our project. Without their help, I couldn't complete this thesis. In my mind, they are the best advisors in the world. I also want to extend my thanks to my committee members, Dr. Gregory Huff and Dr. James Boyd, for their guidance and support throughout my research.

I would like to give my thanks to all my group members at Electroactive Materials Characterization Laboratory (EMCL). They gave me great help in research and life, and I really enjoy spending my graduate studying time with them. Thanks also go to my friends and colleagues and the department faculty and staff for making my time at Texas A&M University a great experience. This work was possible due to the financial support of the Air Force Office of Scientific Research (AFOSR).

Last, but not least, thanks to my parents for their encouragement, sacrifices and being with me in my difficult times. Finally, thanks to my wife Min Qu for her patience, understanding and love.

NOMENCLATURE

AC	Alternating Current
EMCL	Electroactive Materials Characterization Laboratory
AFOSR	Air Force Office of Scientific Research
TiO_2	Titanium Dioxide
$BaTiO_3$	Barium Titanate
SEM	Scanning Electron Microscopy
XRD	X-ray Diffraction
EDS	Energy Dispersive Spectroscopy
FCC	Face Centered Cubic
AFM	Atomic Force Microscope
STM	Scanning Tunneling Microscope
DEP	Dielectrophoresis
SWNTs	Single-Wall Carbon Nanotubes
HRSEM	High-Resolution Scanning Electron Micrographs
$Ba(CH_3COO)_2$	Barium Acetate
$Ti((CH_3)_2CHO)_4$	Titanium Isopropoxide
TEM	Transmission Electron Microscopy
$BaTi[OCH(CH_3)_2]_6$	Barium Titanium Isopropoxide
$SrTi[OCH(CH_3)_2]_6$	Strontium Titanium Isopropoxide
FE-SEM	Fieldemission Scanning Electron Microscopy

NanoAmor	Nanostructured & Amorphous Materials, Inc
ISK	Ishihara Corporation USA
BaC_2O_4	Barium Oxalate
NaCl	Sodium Chloride
NP-9	Nonylphenyl Ether
DMAc	Dimethylacetamid
OM	Optical Microscopy
BSTO	Barium Strontium Oxide
ε'	Dielectric Constant
V	Volume Fraction
N_j	Depolarization Factor
e	Eccentricity
α	Aspect Ratio

TABLE OF CONTENTS

LIST OF FIGURES

Page

LIST OF TABLES

CHAPTER I

INTRODUCTION AND

LITERATURE REVIEW

1.1   Problem Statement

Electric field-mediated manipulation of colloidal-based materials has received considerable attention from the scientific community in recent years. In particular, electric field manipulation of dielectric colloids is an effective means of tuning properties. The objective of this thesis is to focus on developing high dielectric constant nanoparticle dispersions for switchable aircraft antenna systems by investigating the effect of AC electric field on the alignment of titanium dioxide (TiO_2) and barium titanate ($BaTiO_3$) in dielectric oil medium.

The TiO_2 colloids and spherical $BaTiO_3$ nanoparticles are commercially available whereas the high aspect ratio $BaTiO_3$ nanowires are synthesized using a molten salt method. Molten salt method is a relatively easy and cost-effective method. This technique also offers other advantages such as relatively low processing temperature and high purity. These advantages make molten salt method a preferred method compared to solid-state methods or chemical methods. The resulting nanowires are characterized using scanning electron microscopy (SEM), X-ray diffraction (XRD), and energy dispersive spectroscopy (EDS) mapping. The effect of processing time, processing temperature and crystalline phase are also studied.

This thesis follows the style of *Advanced Functional Materials.*

The TiO_2 and $BaTiO_3$ particles are dispersed in oil using mechanical stirring and sonication to achieve uniform colloidal dispersions. The TiO_2 and $BaTiO_3$ colloidal dispersions are then subjected to an AC electric field to study the alignment and chain formation of the particles. The alignment and chain formation are found to be a function of the applied electric field magnitude, frequency and time duration. Dielectric constant of the colloidal dispersions is studied as a function of applied electric field magnitude, frequency and duration. The effect of different shapes and sizes of the particles on the dielectric properties is also investigated. Significant improvement in the dielectric constant of $BaTiO_3$ nanowires is observed in the aligned case compared to that in the random case. Besides, the dielectric constant of aligned $BaTiO_3$ nanowires is significantly higher than that of other colloidal materials. Maxwell-Garnett mixing rule is used to validate the experimental results. Furthermore, different concentrations of $BaTiO_3$-epoxy nanocomposites are processed and the effect of electric field manipulation on the $BaTiO_3$ particles is studied in the presence of epoxy matrix.

1.2   High Dielectric Nanoparticles

1.2.1   Titanium Oxide (TiO_2)

Titanium oxide is one of the most important materials in the optical, electronic, and chemical fields. TiO_2 is known to crystallize in three different crystallographic structures: anatase, rutile, and brookite [1]. Each of these phases has useful physical and chemical properties. Anatase is a metastable phase of TiO_2 and rutile is thermodynamically stable after high temperature annealing. Anatase and rutile phases

crystallize in tetragonal structure while brookite crystallizes in orthorhombic structure [2]. In all of the three crystal modifications, the titanium atoms are surrounded octahedrally in a distorted fashion by six oxygen atoms. The unit cell of anatase is shown in Figure 1.1 [3]. O^{2-} is cubic close packing and half of the tetrahedral spaces are filled with Ti^{4+}. The unit cell of rutile is shown in Figure 1.2 [3]. O^{2-} is hexagonal close packing and half of the octahedral spaces are filled with Ti^{4+}.
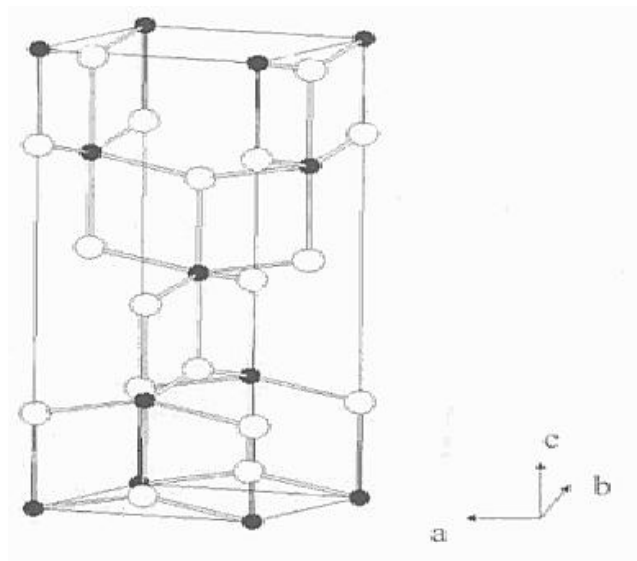
Figure 1.1   Elementary cell of anatase. Black spheres: titanium atoms; white spheres: oxygen atoms [3].
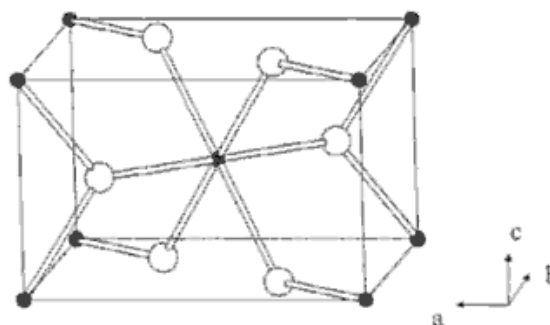
Figure 1.2   Elementary cell of rutile. Black spheres: titanium atoms; white spheres:

oxygen atoms [3].

TiO$_2$ can be synthesized in nano-sized configurations such as nanoparticles, nanorods, nanotubes, nanofibers, etc [4].

1.2.2   Barium Titanate (BaTiO$_3$)

Barium titanate (BaTiO$_3$), one of the "classical" high dielectric constant materials, is one of the first piezoelectric ceramic developed and is still widely utilized in electrical and electronic fields [5]. The unusual dielectric properties of this material were first discovered during World War II [6].

BaTiO$_3$ is isostructural with the mineral perovskite (CaTiO$_3$). The perovskite-like structure, is a ternary compound of formula ABO$_3$ where A and B are different sizes cations [7]. The larger A cation and oxygen get together to form a face centered cubic (FCC) lattice while the smaller B cation occupies the octahedral interstitial sites in the FCC array. In the perovskite structure, the coordination number of A is 12, while the coordination number of B is 6. The unit cell of perovskite cubic structure is shown in Figure 1.3 [8]. The BaTiO$_3$ unit cell consists of a corner-linked network of oxygen

octahedra with Ti^{4+} ion and the Ba^{2+} ions situated in the interstices. If an electric field is applied to this unit cell, the Ti^{4+} ion would move to a new position along the direction of the applied field. The reason of the reversibility of the polarization is the displacement of the central Ti^{4+} ion. "Polarization up" and "polarization down" in Figure 1.3 show two of the six possible permanent polarization positions.

The relation of lattice parameter change with temperature is shown in Figure 1.4 [9]. Above its Curie temperature (approximately 130°C), $BaTiO_3$ ceramic is a isotropic cubic structure. Below the Curie point, the structure is slightly distorted to the tetragonal phase where the c-axis is elongated and the two other a-axes are shortened. With further cooling, another two polymorphic transitions occur at temperatures close to 0°C and -90°C. Below 0°C, orthorhombic structure is formed by the polar axis paralle to a face diagonal. Then, below -90°C, the structure transforms to rhombohedral with the polar axis along a body diagonal. The structure variation of $BaTiO_3$ unit cell is shown in Figure 1.5 [10].

The values of the dielectric constant of $BaTiO_3$ are dependent on many factors, including the type of synthesis, which influences the purity, density, grain size etc. [11], along with temperature, frequency, dopants etc. Temperature dependence of the dielectric constant of $BaTiO_3$ is shown in Figure 1.6 [12]. It has to be pointed out that only the values in the tetragonal phase have a clear meaning in this figure, because they were measured on selected single domain crystals having proper orientations [13].
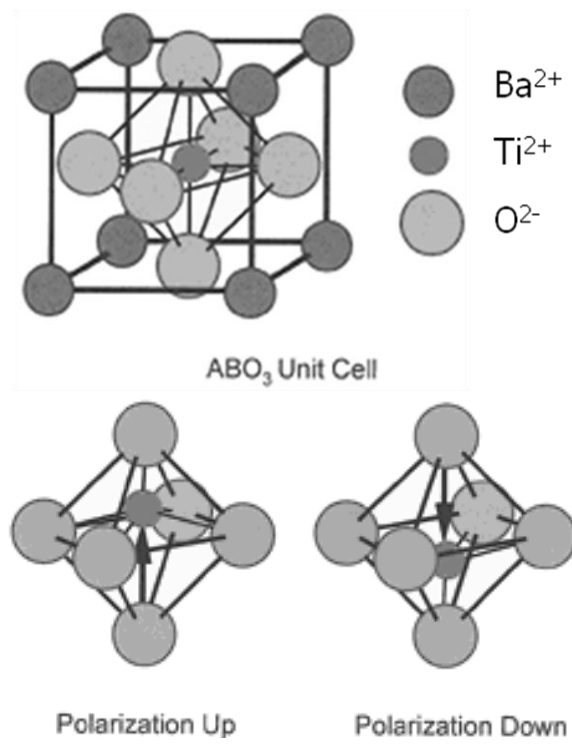
Figure 1.3   Perovskite unit cell for BaTiO$_3$ and polarization reversal model [8].
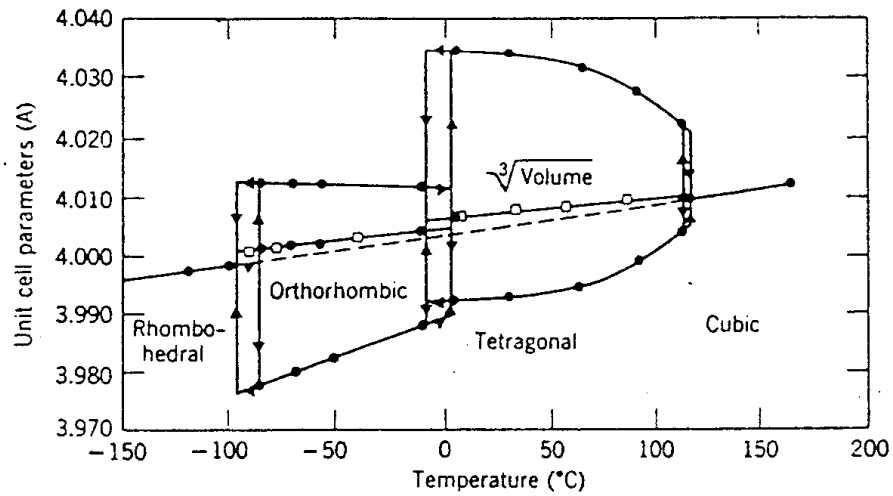
Figure 1.4   Lattice parameters of BaTiO$_3$ as a function of temperature [9].

Cubic

$a=b=c;$
$\alpha=\beta=\gamma=90^{\circ};$

Tetragonal

$a=b\neq c;$
$\alpha=\beta=\gamma=90^{\circ};$

Monoclinic

$a=b;$
$\alpha\neq90^{\circ};$
$\beta=\gamma=90^{\circ};$

Rhombohedral

$a=b=c;$
$\alpha\neq90^{\circ};$
$B\neq90^{\circ};$
$\gamma\neq90^{\circ};$
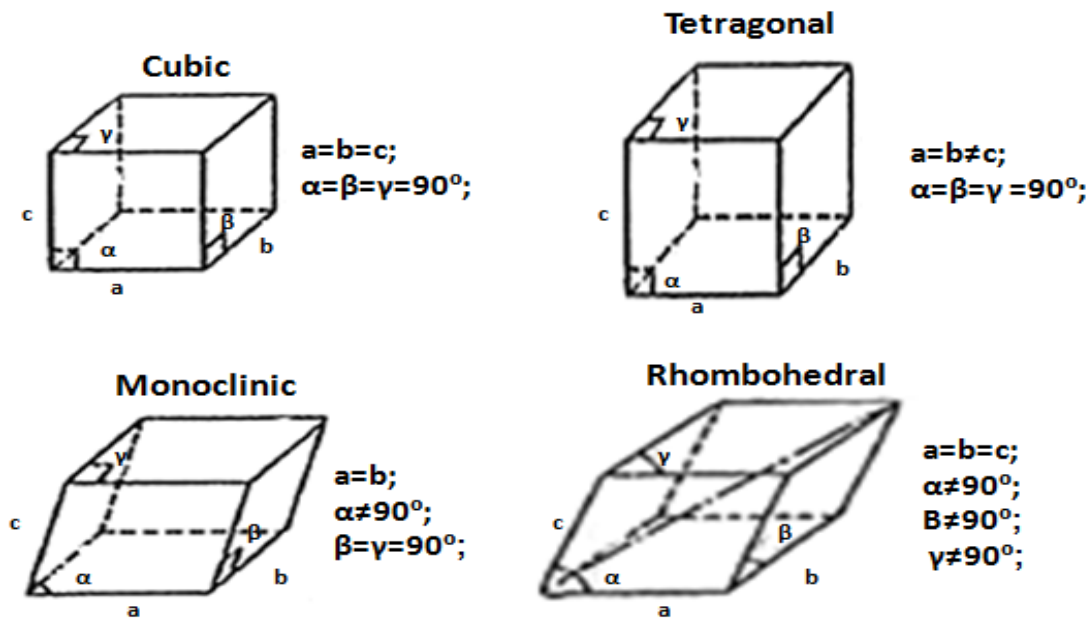
Figure 1.5   Crystallographic changes of $BaTiO_3$ unit cell [10].
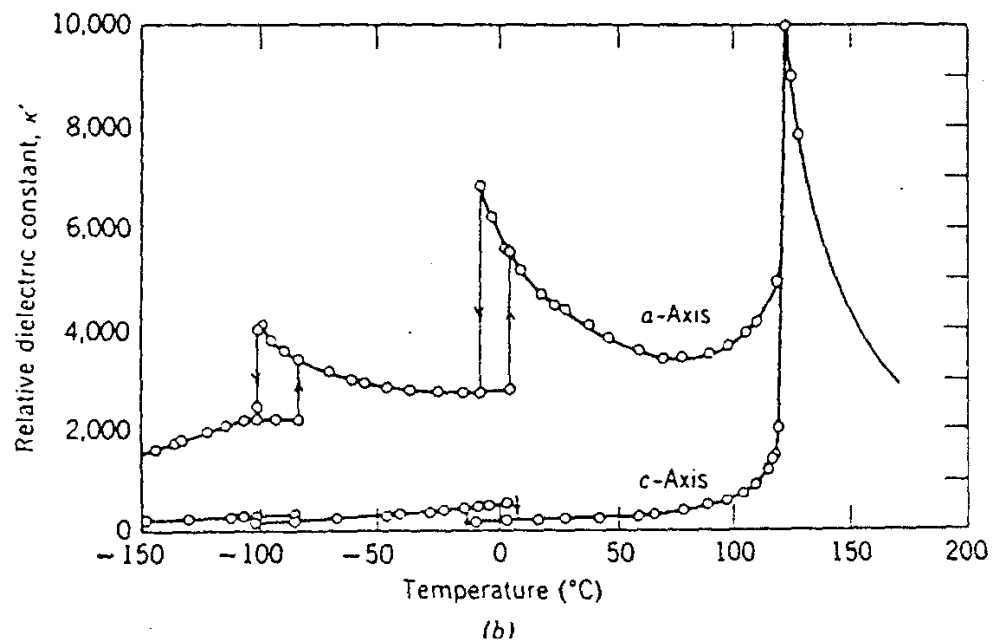
Figure 1.6   Dielectric constants of $BaTiO_3$ as a function of temperature [12].

1. 3   Principle of Dielectric

1.3.1   Dielectric Constant

Capacitance is the ability of a body to hold an electrical charge and a capacitor is a device in an electric circuit for storing electrical charge. A simple capacitor made with parallel brass electrodes is shown in Figure 1.7 [13].
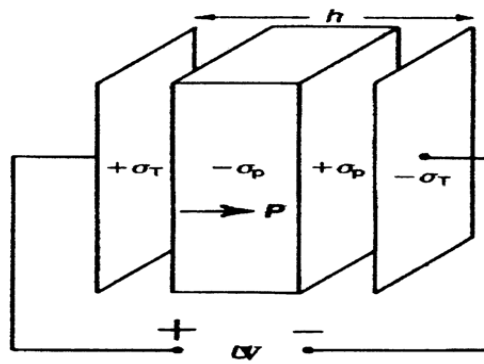
Figure 1.7   A parallel capacitor with a dielectric [13].

Normally, a complex dielectric permittivity ε is used to define the dielectric properties of a material,

$$\varepsilon = \varepsilon' + i\varepsilon''$$ 1.1

The real part ε' is the relative dielectric permittivity (dielectric constant) and the imaginary part ε'' is known as dielectric loss. Dielectric loss is the primary criterion for the usefulness of a dielectric as an insulator material, which is a measure of the heat-related loss of the material. The dielectric constant is the ability of an insulator to store electrical charges, and can be calculated by,

$$\varepsilon' = C * t / \varepsilon_0 * A \qquad\qquad 1.2$$

where C is capacitance, ε_0 is the dielectric constant in vacuum ($\varepsilon_0 = 8.85 \times 10^{-12}$ F/m), t is the thickness of material and A is the area of plate capacitor.

1.3.2 Polarization

Polarization of the dielectric material occurs when the dielectric is placed in an electric field. The dielectric constant increases with increase in the polarizability. It is important to understand the polarization mechanisms in dielectric materials, because both the dielectric constant and the dielectric loss are dependent on it. There are four main types of polarization mechanisms observed in ceramics: electronic polarization, ionic polarization, orientation polarization and interfacial polarization, as shown in Figure 1.8 [7]. In a dielectric material, the total polarizability of the dielectric can be represented as the sum of these mechanisms [14, 15],

$$a = a_e + a_i + a_o + a_s \qquad\qquad 1.3$$

where a_e, a_i, a_o and a_s are electronic, ionic, orientation and space charge contributions respectively.

No Field   Field Applied   No Field

$P_{electronic}$

P_{ionic}

(a)

(b)

No Field   Field Applied   No Field   Field Applied

$P_{dipolar}$

$P_{interfacial}$

(c)

(d)
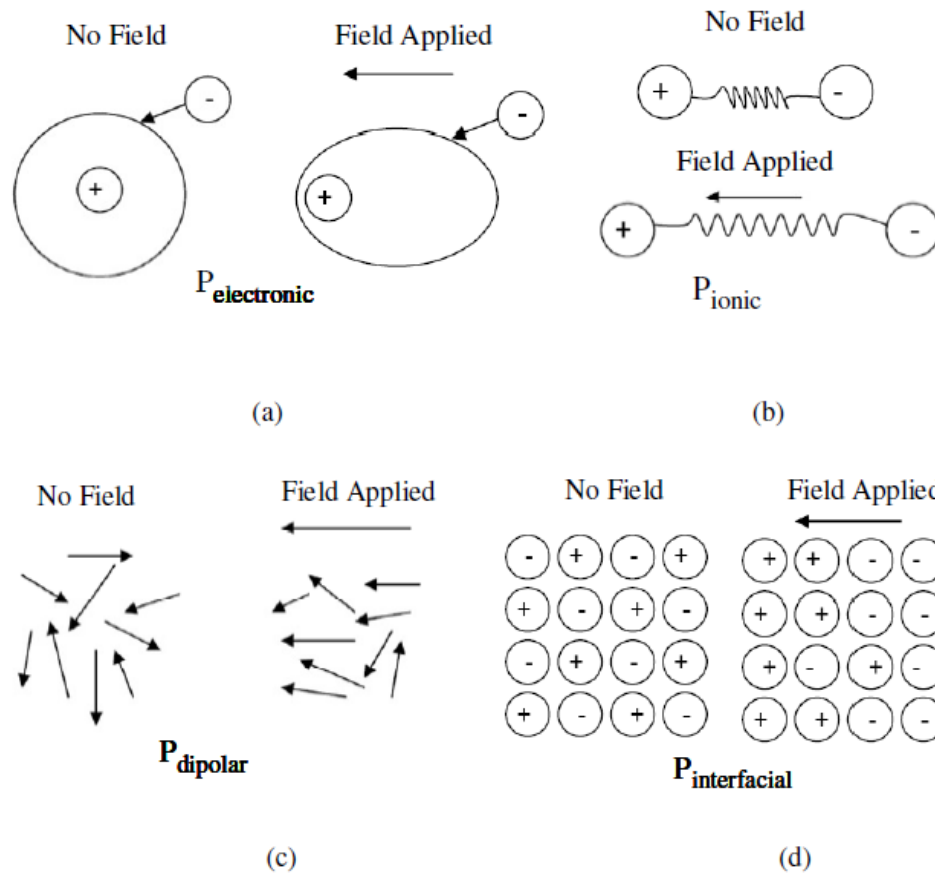
Figure 1.8   Different mechanisms of polarization.

1. 4   Manipulation of Nanoparticles

Current technologies for large-scale nanoparticle manipulation have employed Atomic Force Microscope (AFM) and Scanning Tunneling Microscope (STM) techniques [16]. The nanoparticles can be manipulated by pushing, pulling, picking, placing and positioning them using the AFM tip [17]. However, these methods based on manipulating the particles towards a desired location are difficult to use in parallel manipulation systems required for manufacturing. Some chemical methods of sorting particles are also developed, but they are usually slow and sometimes the particles can

be contaminated during manipulation [18]. Alternatively, manipulating the nanoparticles dispersed in a matrix has been considered promising by applying an external force, such as a mechanical, a magnetic or an electric field. Detailed reviews on some of these different nano-manipulation methods have been discussed by Sitti [17] and Li [19].

Electric field is commonly used to manipulate nanoparticles [20-24]. Numerous studies on nanoparticle electric field manipulation have been carried out in the colloids community. Investigation of colloidal dispersions in electric fields can be used to characterize the size and surface charge of the nanoparticles [25], control display devices [26], understand fundamental phase behavior [27], assemble irreversible nanowires [28] and so on [29]. These applications of colloidal dispersion in electric field are dependent on voltage, frequency and duration of the applied field, and the surface charge of the particles.

Abe et al. have reported controlling silica particles dispersed in aqueous solution using alternating electric fields [30]. They chose two flat electrodes (400 μm apart) to align particles. The particle samples were three different kinds of monodispersed spherical particles (average diameters of 2.0, 4.9, and 9.9 μm respectively). Small silica particles (2.0 and 4.9 μm) dispersed in aqueous solution aligned perpendicular to the applied field. The alignment in an alternating electric field (1000 Hz) is shown in Figure 1.9. On the other hand, Figure 1.10 shows that relatively large particles (9.9 μm) aligned to form strings in the direction parallel to the electric field due to their dielectric polarization.
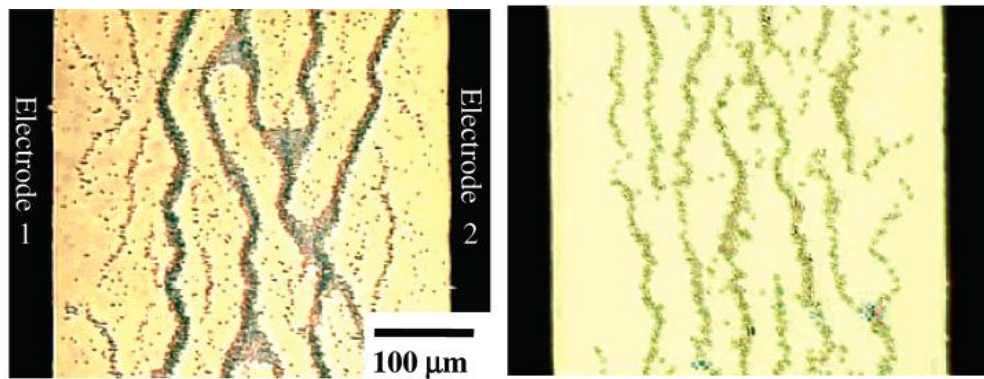
Figure 1.9   Alignment of silica particles suspended in water between the two flat

electrodes. Diameter of silica particles: (left) 2.0; (right) 4.9 μm [30].
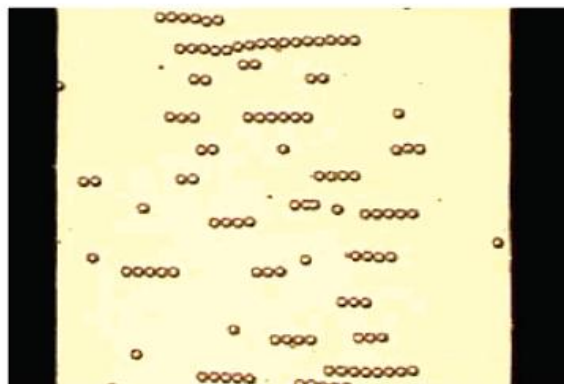
Figure 1.10   Alignment of silica particles suspended in water between the two flat

electrodes. Diameter of silica particles: 9.9 μm [30].

Particle alignment depends on the balance between the electro-osmotic flow and

dielectric polarization acting on the particles. The force causing parallel particle

alignment is electrostatic force resulting from electric charges on the particles induced

due to dielectric polarization. The electrostatic force is proportional to the dipole

moment of the particles which depends on its size (radius in the case of spherical

nanoparticles). Hence, large silica particles would be affected by dielectric polarization more than small silica particles. Alignment of silica particles in different solutions, concentrations and applied electric field frequencies were also investigated.

Velev et al. have reported the use of alternating current (AC) and direct current (DC) electric fields for manipulating the nano-size colloidal particles suspended in water using planar electrodes[31-34]. The effect of electrophoresis, dielectrophoresis and AC electrokinetics have been discussed in the detailed review [33]. Electrophoresis allows charged particles in DC fields to move towards charged electrodes. In dielectrophoresis, particle mobility in AC fields, allows precise manipulation of particles through a range of parameters including the magnitude, frequency of applied fields and electrode geometry. The structures assembled in this research are conductive microwires from metallic nanoparticles and switchable two-dimensional crystals from polymer microspheres. Optical micrographs illustrating the two-stage mechanism of crystallization for latex particles are shown in Figure 1.11 [34].

In the study by Bahukudumbi et al, nanowires were assembled from colloidal gold nanoparticles between planar electrodes [29]. Different microstructures were observed under applied different AC field. The results showed that assembly of gold nanoparticles had a strong dependence on the electric field frequency. Three dominant transport regimes were formed due to various electrokinetic forces acting on the gold particles. For ω (frequency of electric field) = 1–100 Hz, electrophoresis produced oscillatory colloidal motion between the electrodes. For ω = 0.1k–100k Hz, AC electroosmosis produced 3D periodic, recirculating flows on the electrodes within the

confined microfluidic geometry. The electroosmosis flows ejected colloids from the electrode gaps and in combination with sedimentation reconcentrate colloids in stagnation regions on top of the electrodes. For $\omega > 100k$ Hz, line wire structures occurred as a result of AC electric fields inducing dipoles in colloids, transporting colloids via dielectrophoresis (DEP). Increasing the applied voltage increased the number of chains, rate of formation and chain bundling. Optical microscope images of the alignments are shown in Figure 1.12.
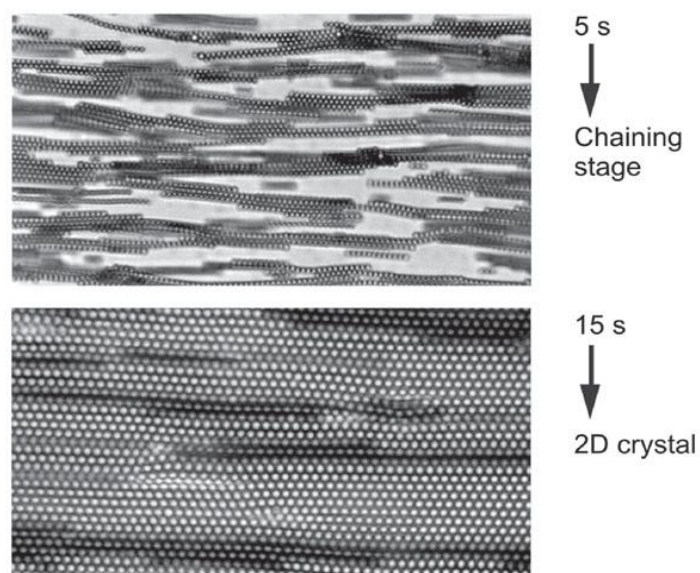
Figure 1.11   Assembly process of polystyrene microspheres in a thin experimental cell under an AC electric field. (Upper) Shortly after the field is applied, the particles align in chains due to dipolar attraction. Simultaneously, the DEP force due to the field gradient attracts the particles to the high field intensity region. (Below) The particle chains confined on the surface form 2D-hexagonal crystals aligned with one axis in the direction of the field [34].
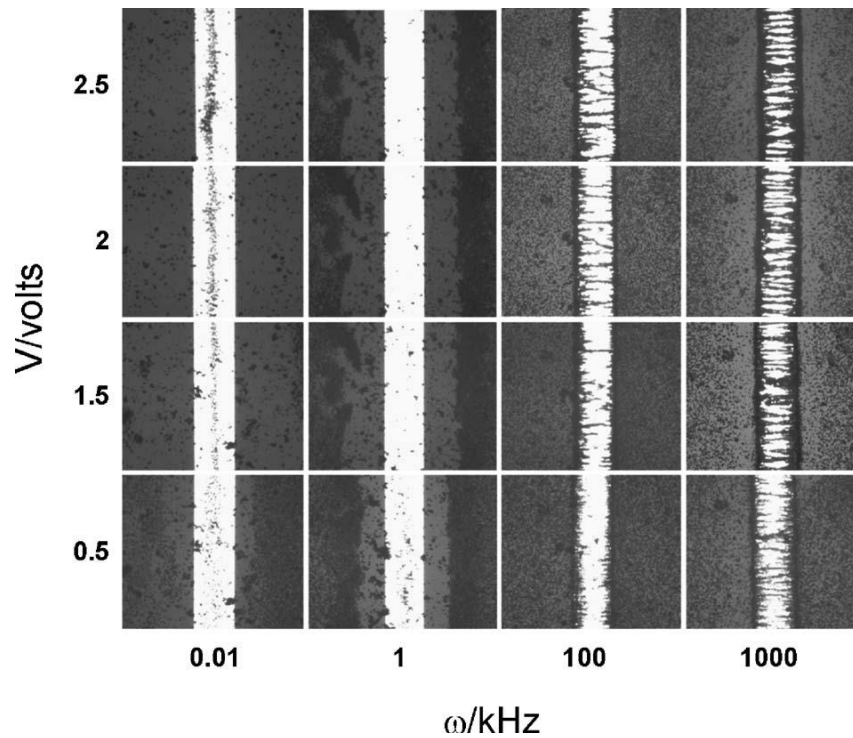
Figure 1.12   Steady-state configurations of 800 nm gold colloids within a 30 μm gap

between interdigitated coplanar gold film electrodes as a function of applied AC electric

field frequency and amplitude [29].

AC electric field was also used to align single-wall carbon nanotubes (SWNTs)

in polymers [35, 36]. Park et al. improved the mechanical properties of SWNT- acrylate

polymer composites by aligning SWNTs under an AC electric field [35]. Optical

microscope images and High-Resolution Scanning Electron Micrographs (HRSEM) of

SWNTs network are shown on Figure. 1.13. Electric field strength and frequency

influence the degree of alignment of the SWNTs. The optical microscope images of

SWNTs alignment using different controllable parameters, obtained by Banda et al, is

shown on Figure 1.14 [36]. After alignment, a blue light gun was used to cure the polymer and the aligned SWNTs were immobilized. Both electrical conductivity and dielectric constant were measured to quantify the improvement of SWNT alignment in the acrylate polymer. With the electric field strength increasing from 10 V to 250 V, the electrical conductivity increased five orders while dielectric constant increased by two orders. Similar results were observed by increasing the electric field frequency from 0.01 Hz to 100 kHz. In all cases, the electrical conductivity and dielectric constant values in the parallel direction were much greater than the values in the perpendicular direction. The results indeed indicated that the aligning SWNTs can enhance the electrical and dielectric properties of the SWNT based composites.

(a)   (b)
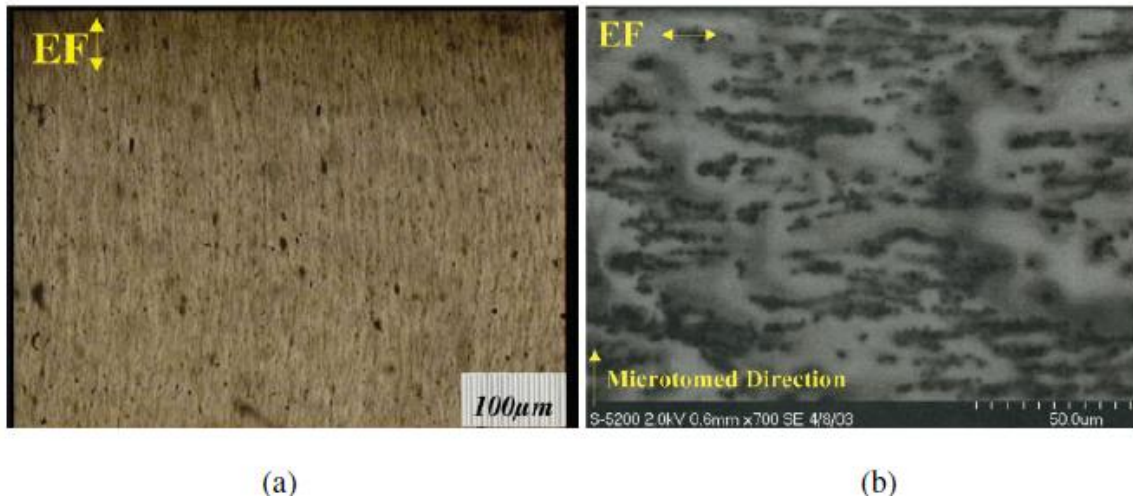
Figure 1.13   SWNT network formation by applying AC electric field in polymer.

(a) Optical microscope micrograph and (b) HRSEM micrograph [35].
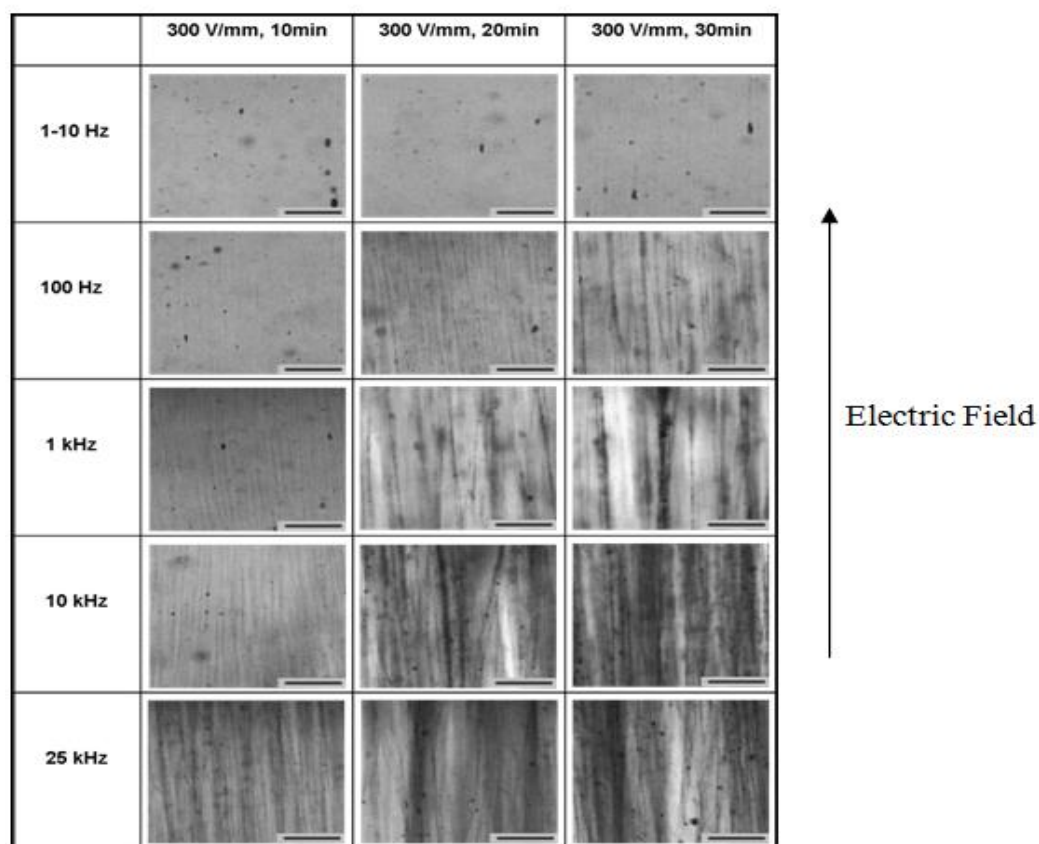
Figure 1.14   In-situ microscopy images of 0.03 wt% SWNT-acrylate system at an

applied electric field of 300 V/mm, different frequencies (1 Hz to 25 MHz) and different

time intervals (0-30 min) [36].

Although there have already been some experimental analysis of the electric

field manipulation of nano or micro particles in colloids, few of the studies have focused

on high dielectric constant nanoparticles in dielectric medium. The effect of different

electric field controlled parameters on aligning and network formation of different shape

and size of nanoparticles needs to be studied. Besides, there still exists a need to

understand the various mechanisms driving the particle manipulation by the external electric field and by the medium.

1.5   Synthesis of Barium Titanate (BaTiO$_3$)

1.5.1   BaTiO$_3$ Synthesis Methods

BaTiO$_3$ has been synthesized using a variety of methods by different researchers. The techniques used include solid-state reaction methods, chemical methods and molten salt methods [37-39]. Along with the type of synthesis, the quality of the precursors also influences the quality and quantity of the powders. The selection of techniques for synthesizing barium titanate depends on cost as well as target applications [8, 38].

In a typical solid-state reaction synthesis, BaCO$_3$ or BaO and TiO$_2$ are mixed as reactors. Normally, solid-state reaction methods require calcination of the reactors at high temperature, approximately from 800 ℃ to 1200 ℃ [40, 41]. Size control of BaTiO$_3$ is possible in solid-state reaction by changing the size of TiO$_2$ and milling conditions of BaCO$_3$ [42]. Using smaller size TiO$_2$ particles with high surface area can result in a faster initial reaction. Also, mechanically milled BaCO$_3$ particles can accelerate the diffusion process and decrease the calcinations temperature. Due to high reaction temperature, heterogeneous solid phase reaction and other reasons, BaTiO$_3$ powders prepared by this method may be highly agglomerated, resulting in large particle size and high impurity contents [43].

Chemical methods can produce BaTiO$_3$ directly from the solution at relatively low temperatures and are able to synthesize crystallized powder with high purity [44].

Different techniques, including sol-gel method, hydrothermal method, co-precipitation method, combustion synthesis, and so on, have been employed for synthesis of $BaTiO_3$ powder. Different synthesis techniques for $BaTiO_3$ result in different properties of the powder [45]. However, chemical methods are limited by high cost and difficulties in controlling the process.

Sol-gel method was developed to process $BaTiO_3$ by hydrolyzing the chemical precursor to form a sol and then a gel-like diphasic system containing both liquid and solid phases. Amorphous $BaTiO_3$ can be obtained by drying and pyrolysis of the gel [38, 46]. This technique exhibits several advantages such as fine particle size, simple compositional control and low processing temperature [47].

Highly crystallized $BaTiO_3$ powders can be processed from barium–titanium–acetate precursors by hydrothermal synthesis [40]. This technique crystallizes substances from aqueous solutions at vapor pressures. The hydrothermal method is attractive for synthesizing $BaTiO_3$ powder. Combined effects of solvent, temperature and pressure on the ionic reaction equilibrium can result in the production of particles with a narrow size distribution, and less impurities[48].

Coprecipitation method is a simple and convenient method for achieving chemical homogeneity through intimate contact and mixing of constituent ions on the molecular level under controlled conditions [49]. Complex compound can form between Ba and Ti with the same atomic ratio, then the Ba and Ti will be mixed at atomic level and may convert to $BaTiO_3$ with or without a minimum of diffusion. This is a very

successful method that has been used commercially to prepare high purity $BaTiO_3$ [50, 51].

Combustion synthesis has also been studied and is applicable to the synthesis of $BaTiO_3$. This method started with intimately mixed. A combustion reaction, which could convert spray-dried mixture in an aqueous solution to process $BaTiO_3$, occurs when heating the product to a relatively low temperature [50]. The synthesized particles were well crystallized tetragonal $BaTiO_3$ with nano-scale median diameter of the particles [52].

The molten salt synthesis method is an alternative simple method for formation of fine powders under relatively low temperature with a shorter soaking time [53]. The molten salt is used as a reaction aid that provides an alternative to aqueous chemistry. This occurs due to change in the solubility and/or the reactivity of the reactants and increase in the reaction temperature [54]. The molten salt method exhibits several advantages by coupling the salt intervention to the formation reaction and the mechanism of the solid-state reaction [55]. In the molten salt synthesis, reactions are usually controlled by chemical equilibria, while in other methods such as coprecipitation and sol-gel methods, they are controlled by the chemical and crystallographic constraints. Also, molten salt method process is much faster than the diffusion-controlled solid-state reaction method.

1.5.2   Synthesis of High Aspect Ratio Nanoscale $BaTiO_3$

Nanoscale structures, including nanorods, nanowires, nanocubes, and nanotubes, have attracted extensive synthetic attention as a result of their novel size-dependent

properties [56]. Many efforts have been made to probe the electronic, optical and magnetic properties of these nanostructures since they exhibit properties different from the bulk materials.

Yuanbing et. al [56] prepared single-crystal $BaTiO_3$ nanowires using molten salt method in the presence of NaCl and a nonionic surfactant (NP-9) at 820 °C. The nanowires have around 50-80 nm diameter, and their lengths lie between 1.5 μm to as high as 10 μm. The SEM image of the $BaTiO_3$ nanowires is shown in Figure 1.15. They also reported the purity and crystallinity of the as-prepared samples using TEM and EDS.
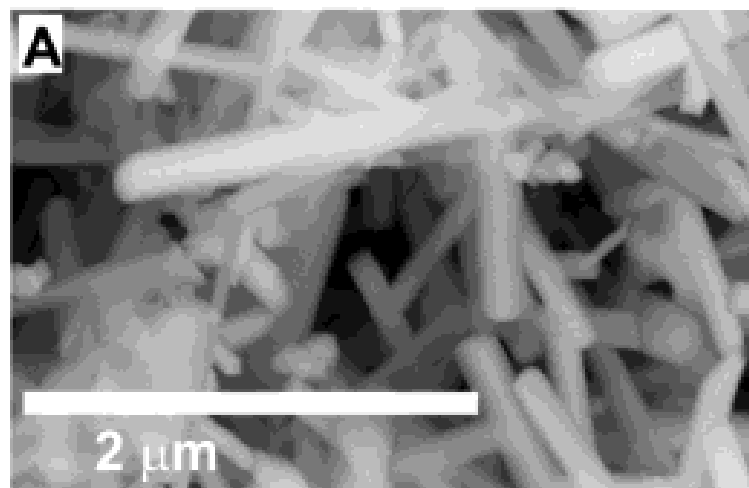
Figure 1.15   SEM images of as-prepared $BaTiO_3$ nanowires [56].

Junhan et. al [57] have reported the synthesis of $BaTiO_3$ nanofibers via electrospinning using barium acetate $[Ba(CH_3COO)_2]$ and titanium   isopropoxide $[Ti((CH_3)_2CHO)_4]$ as the precursors. Nanofibers were obtained with an average crystallite size of about 20 nm. Furthermore, single crystal $BaTiO_3$ nanofibers with 50

nm in diameter and lengths up to 1 μm were obtained. The SEM images of prepared nanofibers are shown in Figure 1.16. Fiber morphology and phase evolution were investigated by using various heat treatment conditions. Perovskite tetragonal structures of BaTiO$_3$ nanofibers were confirmed by XRD, TEM and Raman spectroscopy.
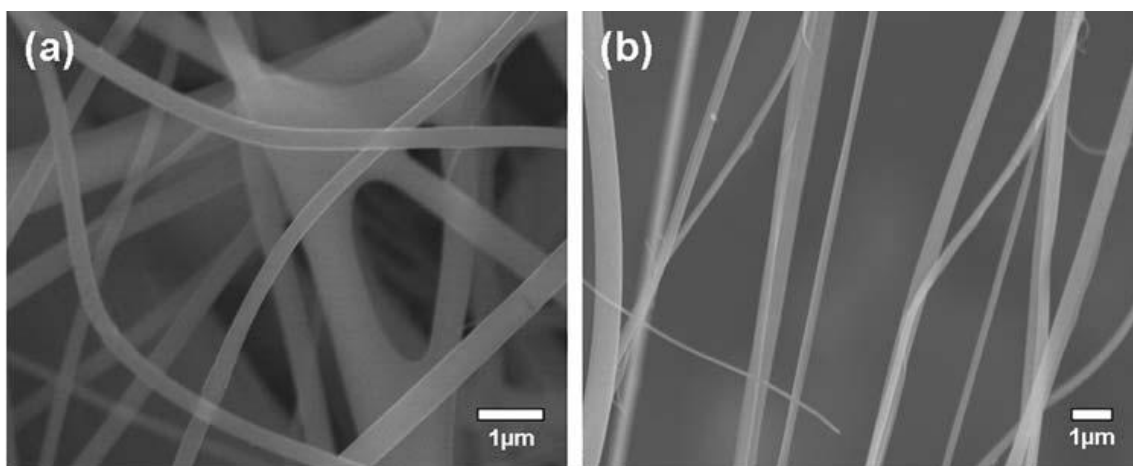
Figure 1.16   SEM images of as-prepared BaTiO$_3$ nanofibers. (a) as-synthesized and dried at 120 ℃, 1 hour; (b) after polymer burnout at 450 ℃, 3 hours [57].

Jeffrey et. al [58] synthesized single-crystal nanorods composed of BaTiO$_3$ and Strontium titanate (SrTiO$_3$) by a solution-based decomposition of bimetallic alkoxide precursors. The precursors were barium titanium isopropoxide (BaTi[OCH(CH$_3$)$_2$]$_6$) and strontium titanium isopropoxide (SrTi[OCH(CH$_3$)$_2$]$_6$). The range of the diameters of well-isolated nanorods is between 5 to 60 nm. The lengths of the nanorods can be as high as 10 μm. The TEM image of prepared nanorods is shown in Figure 1.17. The

analysis of TEM and XRD data demonstrate that the synthesized nanorods were composed of crystalline $BaTiO_3$ and $SrTiO_3$ with a cubic perovskite structure.
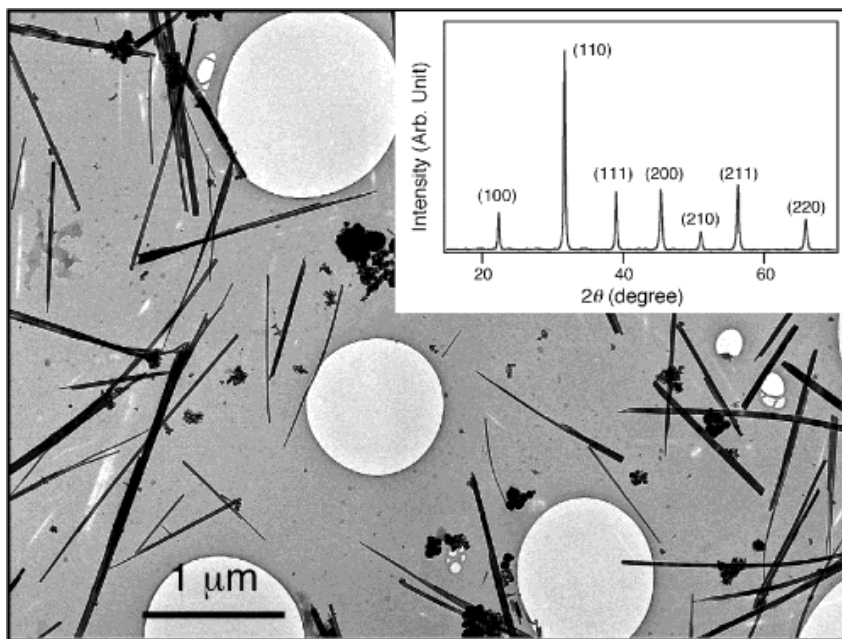
Figure 1.17   TEM image of as-prepared $BaTiO_3$ nanorods. Inset: XRD of the reaction

product composed of randomly oriented $BaTiO_3$ nanorod ensembles [58].

Changlong et. al [59] reported a facile and low-cost synthesis of single-crystalline $BaTiO_3$ nanowires at very low temperature (50 °C) in ethanol solution. The inorganic raw materials included $Ba(OH)_2$ $8H_2O$ and H_2TiO_3 powders. The prepared $BaTiO_3$ nanowires have a diameter ranging from 50 nm to 120 nm and a length up to 10 μm. The SEM images of synthesized nanowires are shown in Figure 1.18. SEM and fieldemission scanning electron microscopy (FE-SEM) were applied to investigate the

morphology. XRD and TEM were used to confirm the tetragonal phase of $BaTiO_3$ nanowires.
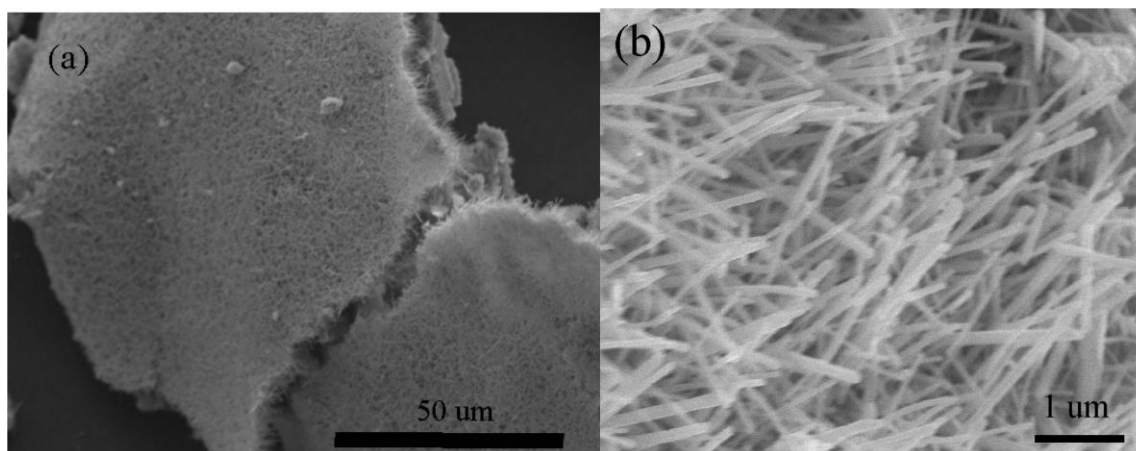
Figure 1.18   Representative SEM images of as-synthesized $BaTiO_3$ nanowires. (a) An overview image of the $BaTiO_3$ nanowires on large scale; (b) high-magnification photo of the nanowires [59].

1.6   Organization of Sections

This study on synthesis and electric field-manipulation of high aspect ratio barium titanate has been organized into four chapters. Chapter I covers problem statement, introduction of high dielectric nanoparticles: TiO_2 and $BaTiO_3$ and principles of dielectric spectroscopy. This chapter also contains the literature review of electric field manipulation of nanoparticles, $BaTiO_3$ synthesis and synthesis of nano-scale high aspect ratio $BaTiO_3$ particles.

Chapter II is the experimental section which introduces the processing and experimental characterization techniques used in this study. Experimental approach and

materials are described along with processing information of high aspect ratio $BaTiO_3$ nanowires, random colloidal-based dispersions for electric field manipulation and $BaTiO_3$-epoxy nanocomposites. Electric field manipulation set up and experimental characterization tools employed are also discussed. Finally, Maxwell-Garnett mixing rule is introduced for theoretical analysis.

Chapter III presents the results of processing and experimental characterization of the high aspect ratio $BaTiO_3$ nanowires. The effect of time, temperature and crystalline phase of reactor in preparation process are also studied. The chapter also presents the results of electric field manipulation of the particles and $BaTiO_3$-epoxy nanocomposites. The influence of various parameters on alignment of nanoparticles, including electric field magnitude, frequency, concentration and time, is studied. Experimental results, such as optical microscopy, SEM, XRD, EDS mapping and in-situ dielectric spectroscopy, are also discussed.

Chapter IV offers conclusions of the study and recommendations for future follow up work.

CHAPTER II

EXPERIMENTAL

This chapter introduces the processing and experimental characterization techniques employed for: (a) high aspect ratio BaTiO$_3$ nanowires, (b) random colloidal-based dispersions for electric field manipulation and (c) BaTiO$_3$-epoxy nanocomposites. The experimental conditions and the description of different characterization tools like Optical Microscopy (OM), Scanning Electron Microscopy (SEM), LCR Meter and Dielectric Spectroscopy, and Energy Dispersive Spectroscopy mapping (EDS mapping) are described in the later part of this chapter.

2.1   Materials Used

Titanium Oxide (TiO$_2$) and barium titanate (BaTiO$_3$) particles with different sizes and shapes are used in this study.

2.1.1   Titanium Oxide (TiO$_2$)

Titania nanowhiskers and aciculars were obtained from Nanostructured & Amorphous Materials, Inc (NanoAmor) and Ishihara Corporation USA (ISK) respectively.

Titania nanowhiskers (Rutile, 98%+) have average diameter around 10 nm and length around 40 nm, with a density of 4.23g/cm^3. Figures 2.1 (a) and (b) show the scanning electron microscopy (SEM) image and wide angle x-ray diffraction (XRD) data of the titania nanowhiskers. Three different types of titania acicular are also used,

namely FTL-100, FTL-200 and FTL-300. Figure 2.2 shows the SEM images of the three

different FTL series samples. The properties of FTL series are listed in Table 2.1.
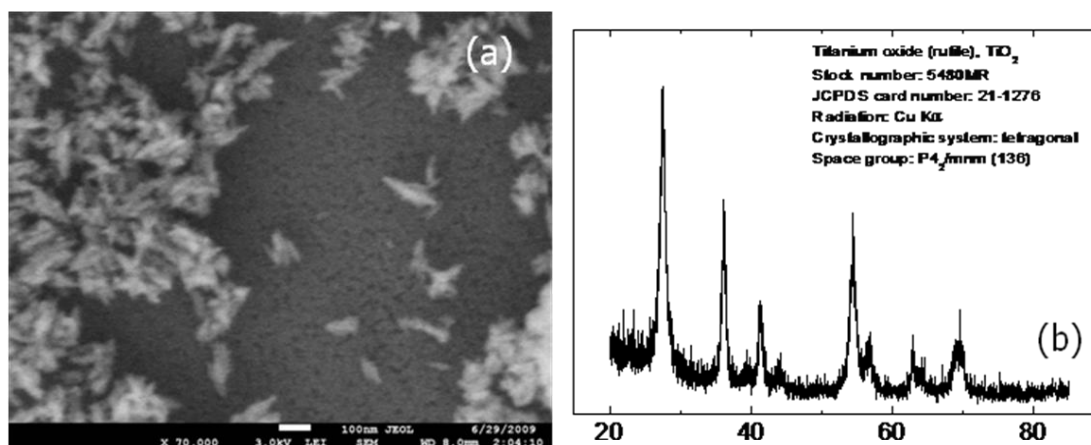
Figure 2.1   (a) SEM image of Titania nanowhiskers; (b) XRD of Titania

nanowhiskers (http://www.nanoamor.com/).

Table 2.1   Physical properties of Titania Acicular.

	FTL-100	FTL-200	FTL-300
Composition / Crystal	TiO_2 / Rutile	TiO_2 / Rutile	TiO_2 / Rutile
Shape / Color	Acicular/White	Acicular/White	Acicular/White
Particle Length (μm)	1.68	2.86	5.15
Particle Diameter (μm)	0.13	0.21	0.27
Specific Gravity	4.2	4.2	4.2

http://www20.inetba.com/
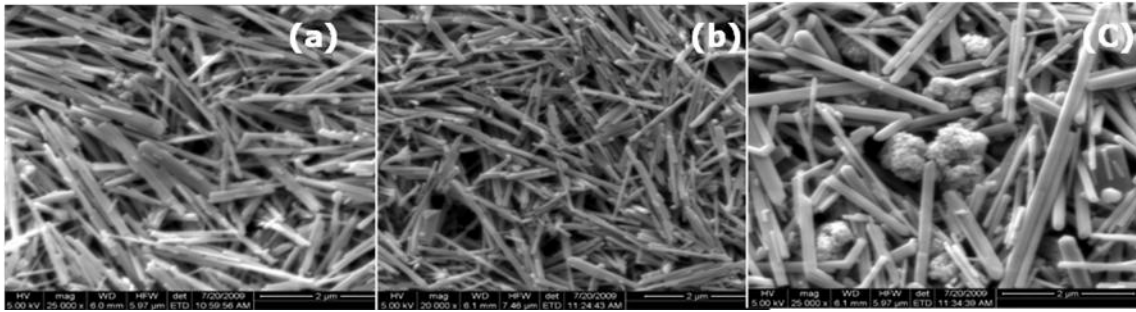
Figure 2.2   SEM images of FTL series samples. (a) FTL-100; (b) FTL-200;

(c) FTL-300.

2.1.2   Barium Titanate (BaTiO$_3$)

High aspect ratio BaTiO$_3$ nanowires were synthesized in our lab using a molten salt method while barium strontium titanate (BSTO) spherical nanoparticles (diameter around 50 nm) were obtained from TPL, Inc. The processing and properties of BaTiO$_3$ nanowires will be discussed in the following sections.

2.2   Processing of High Aspect Ratio BaTiO$_3$ Nanowires

To obtain high aspect ratio BaTiO$_3$ nanowires, low-cost facile molten salt laboratory method is used [56]. First, barium oxalate (BaC$_2$O$_4$, Alfa Aesar), TiO$_2$ (anatase, 15 nm, NanoAmor), sodium chloride (NaCl, >99.5%, Sigma-Aldrich), and NP-9 (nonylphenyl ether, Sigma-Aldrich) were mixed in the molar ratio of 1:1:20:3. The mixture was ground using agate mortar pestle for 30 minutes and probe sonicated for 5-10 minutes and poured into a high temperature zirconia crucible. The mixture was then

annealed in a high temperature oven for 3.5 hours at 820 ℃ and subsequently cooled to room temperature. Next, the sample was centrifuged at 2000 rad/min a total of 20 times and water washed 50 times using distilled water. Finally, the sample was dried in a vacuum oven overnight at 120 ℃. The processing steps are summarized in the flow chart shown in Figure 2.3.
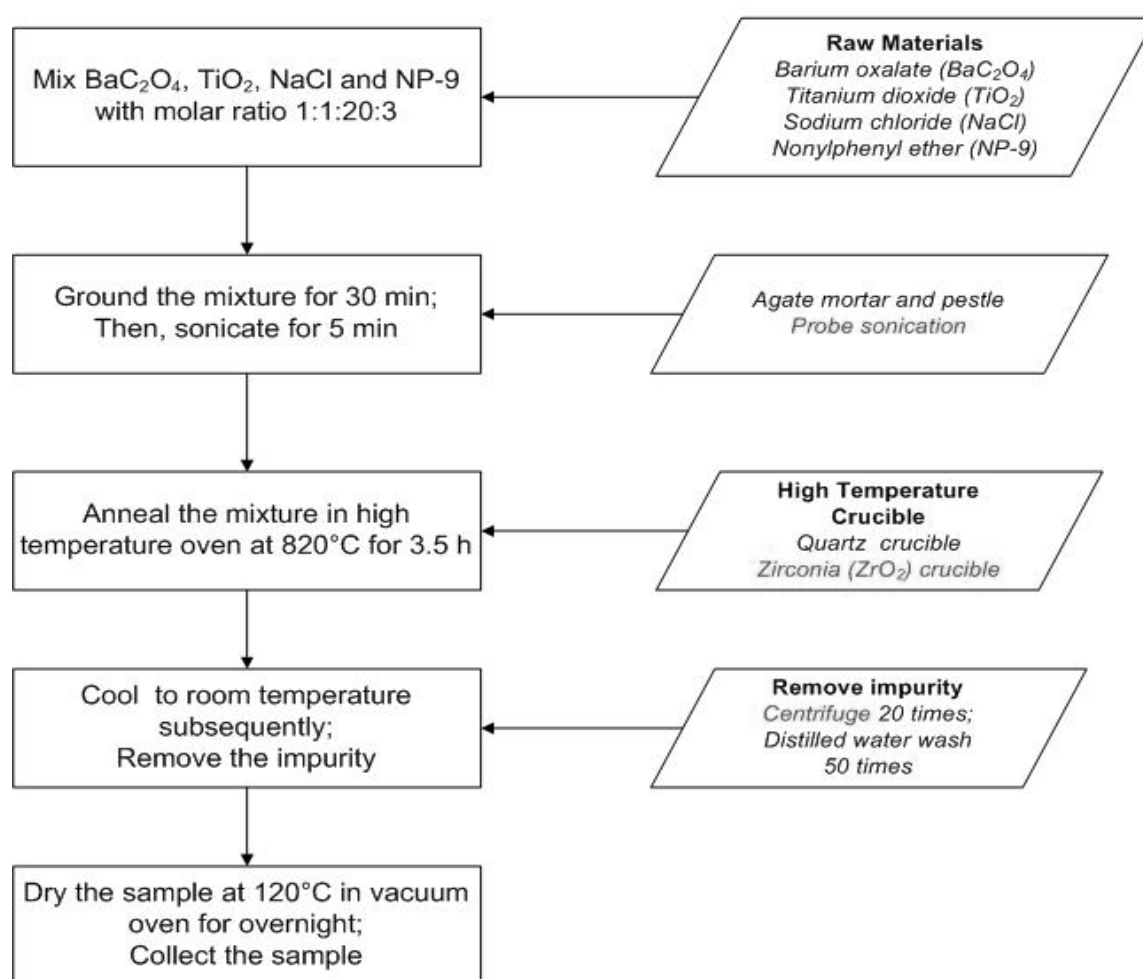
Figure 2.3 Flow chart showing processing of BaTiO$_3$ nanowires.

2.3   Processing of Random Colloidal-based Dispersions

3-IN-ONE® multi-purpose oil is chosen as the solvent to disperse the TiO_2 and $BaTiO_3$ nanoparticles. The mixture is stirred in a round neck flask with a Fisher scientific mechanical stirrer at 160 rpm for 6 hours. A bath sonicator was used to ensure good dispersion of the nanoparticles in oil. Different concentration dispersions were processed by this method.

2.4   Processing of $BaTiO_3$-Epoxy Nanocomposites

Epon 862 epoxy and curing agent 'W' were purchased from Miller Stephenson inc. Chemical structures of Epon 862 and curing agent 'W' are shown in Figure 2.4. The weight ratio of prepared Epon 862 and 'W' was 100:26.4. Dimethylacetamid (DMAc) was used to aid the dispersion of $BaTiO_3$ nanowires in epoxy. First, $BaTiO_3$ nanowires and DMAc were mixed using a mechanical stirrer and bath sonicator for 3 hours. Epon 862 was then added to the mixture followed by further mechanical stirring and bath sonication for another 3 hours. Next, the mixture was placed in vacuum oven to evaporate DMAc at 80 °C until all solvent is removed. Curing agent 'W' was added to the mixture followed by another hour of stirring and sonication. The viscosity of the solution increased after mixing the curing agent. The viscous solution was then degassed at 60 °C in the vacuum oven again until all air bubbles disappeared. Finally, the sample is poured into a metal mold and thermally cured in a Sun environmental chamber. The curing cycle is carried out in two steps: the sample is first held at 122 °C for 2 hours and then at 177 °C for another 2 hours. Different concentrations of $BaTiO_3$-epoxy

nanocomposites were prepared using this technique. Figure 2.5 shows an overview of the processing steps.
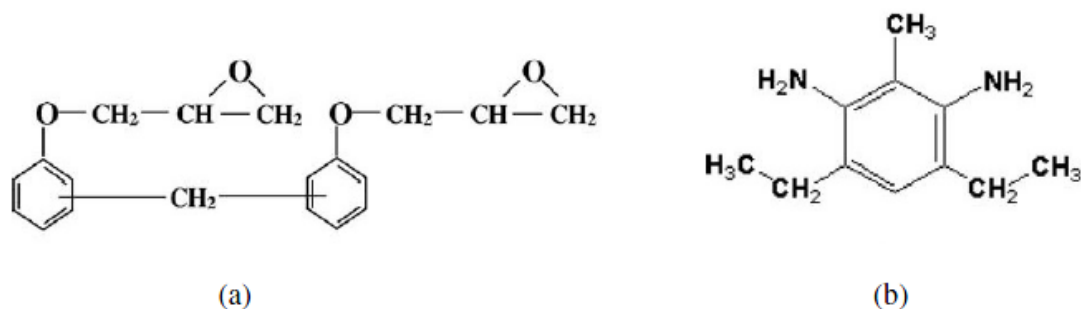
Figure 2.4   Chemical structures of (a) Epon 862 epoxy and (b) curing agent 'W'[60].

2.5   Electric Field Manipulation Experimental Set-up

AC electric field is used to manipulate colloidal-based oil and epoxy polymer dispersions. An HP 33120A function generator is used in combination with a TREK 609D-6 high voltage amplifier to apply voltages in the range of 100 V to 2 kV. An optical microscope is used to assess the uniform dispersion and alignment of composites. Copper electrodes are placed parallel to each other and fixed on a microscope slide as shown in Figure 2.6. The state of dispersion is observed under the microscope when AC electric field is applied. It is noted that the polymer solution is not cured using this set up. a schematic of the set-up is shown in Figure 2.7.
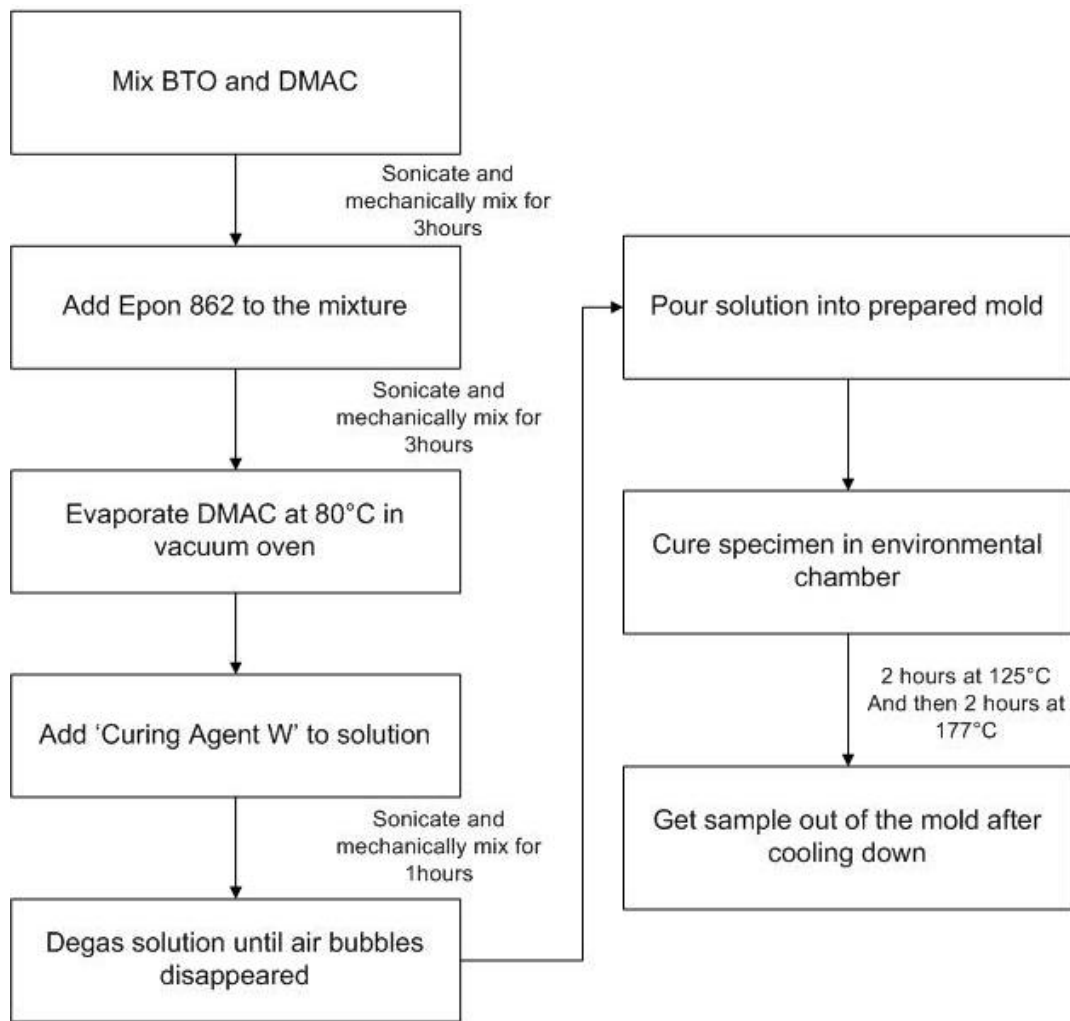
Figure 2.5   Flow chart showing of processing BaTiO$_3$-epoxy nanocomposites.

Figure 2.6   Parallel copper electrodes with a gap size 1mm.
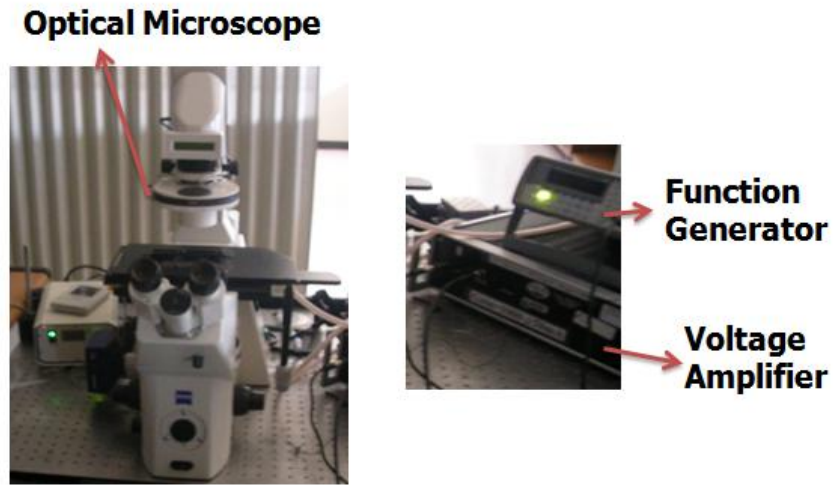
Figure 2.7   Experimental set up for electric field manipulation.

2.6   Experimental Characterization Techniques

2.6.1   Optical Microscopy (OM)

The OM images in the experiment are captured using an inverted Zeiss[®] transmission optical microscope. In a transmission optical microscope, light is transmitted through the sample, which allows us to probe dispersion and alignment in-situ.

2.6.2   Impedance Spectroscopy

QuadTech 7600 precision LCR meter and Novocontrol[®] broadband high impedance analyzer are used to measure the dielectric constant and electrical conductivity of the samples. With the LCR meter, the measurement frequency range used is from 10 Hz to 2 MHz with a measurement accuracy of 0.05%. The measurement

frequency range of the Novocontrol is 10^{-2} Hz to 10^7 Hz. Circular silver electrodes are vapor deposited onto polymer nanocomposites samples.

2.6.3 SEM and EDS mapping

SEM imaging was performed using a JEOL-JSM 6400 scanning electron microscope, operated at 15 kV. The SEM samples were coated with a thin layer of Au/Pd of approximately 30-40 nm thickness using a Cressington 308 coater to prevent charging [61]. Energy dispersive spectroscopy (EDS) is employed for the elemental analysis or chemical characterization of the sample. EDS mapping can validate the existence of possible element in the synthesized particles.

2.7 Theoretical Analysis

2.7.1 Maxwell-Garnett Mixing Rule

For a two-phase mixture with isotropic dielectric components and spherical inclusion geometry, the effective dielectric properties of materials can be calculated by the most common mixing rule, i.e., Maxwell Garnett formula [62],

$$\varepsilon_e = \varepsilon_1 + 3V\varepsilon_1 \frac{\varepsilon_2 - \varepsilon_1}{\varepsilon_1 + 2\varepsilon_1 - V(\varepsilon_2 - \varepsilon_1)} \tag{2.1}$$

ε_e is effective dielectric constant, ε_1 is dielectric constant of medium, ε_2 is dielectric constant of inclusions (particles), V is the volume fraction of particles. It satisfies the limiting processes for both vanishing inclusion phase $V{\rightarrow}0$ and vanishing background $V{\rightarrow}1$.

We can also consider ellipsoidal shapes for the inclusions to study the shape effect of inclusions on the dielectric constant [63]. Many practical cases, such as discs and needles, can be considered as special ellipsoids. Cylinders can be similar to ellipsoids if they have high aspect ratio or are infinite. For an ellipsoid, we have to consider an important parameter, namely, its depolarization factor. If the semi-axes of an ellipsoid in the three orthogonal directions are a_x, a_y, and a_z, as shown in Figure 2.8, the depolarization factor N_x (the factor in the a_x -direction) is,

$$N_x = \frac{a_x a_y a_z}{2} \int_0^\infty \frac{ds}{(s+a_x^2)\sqrt{(s+a_x^2)(s+a_y^2)(s+a_z^2)}} \tag{2.2}$$

And the three depolarization factors for any ellipsoid satisfy,

$$N_x + N_y + N_z = 1 \tag{2.3}$$

So, for prolate spheroids ($ax>ay=az$), we can have

$$N_x = \frac{1-e^2}{2e^3}(\ln\frac{1+e}{1-e} - 2e); \tag{2.4}$$

and

$$N_y = N_z = 0.5(1-N_x) \tag{2.5}$$

where the eccentricity is,

$$e = \sqrt{1-a_y^2/a_x^2} \tag{2.6}$$

Different from spherical particles, the ellipsoid dispersion has two different situations according to the orientation of inclusions. The random and aligned mixtures are shown in Figure 2. 8. For random orientation, all the ellipsoids in the mixture are

randomly oriented, that means they no longer exist in any macroscopically preferred direction in the mixture. The mixture is isotropic and the effective permittivity would be a scalar. Maxwell Garnett formula will change to,

$$\varepsilon_e = \varepsilon_1 + \varepsilon_1 \frac{\dfrac{V}{3} \sum\limits_{j=x,y,z} \dfrac{\varepsilon_2 - \varepsilon_1}{\varepsilon_1 + N_j(\varepsilon_2 - \varepsilon_1)}}{1 - \dfrac{V}{3} \sum\limits_{j=x,y,z} \dfrac{N_j(\varepsilon_2 - \varepsilon_1)}{\varepsilon_1 + N_j(\varepsilon_2 - \varepsilon_1)}} \quad (2.7)$$

For aligned orientation, all the ellipsoids in the matrix are assumed to be aligned and the orientations are the same. Then the effective permittivity of the mixture is anisotropic, in other words, the mixture may have different permittivity components in the three different principal directions. For orientation in the x-direction, the Maxwell Garnett formula for this mixture will change to,

$$\varepsilon_e = \varepsilon_1 + V\varepsilon_1 \frac{\varepsilon_2 - \varepsilon_1}{\varepsilon_1 + (1-V)N_j(\varepsilon_2 - \varepsilon_1)} \quad (2.8)$$

Similarly, for a_y and a_z direction, by replacing N_x by N_y and N_z, we will get the effective dielectric constant.

37
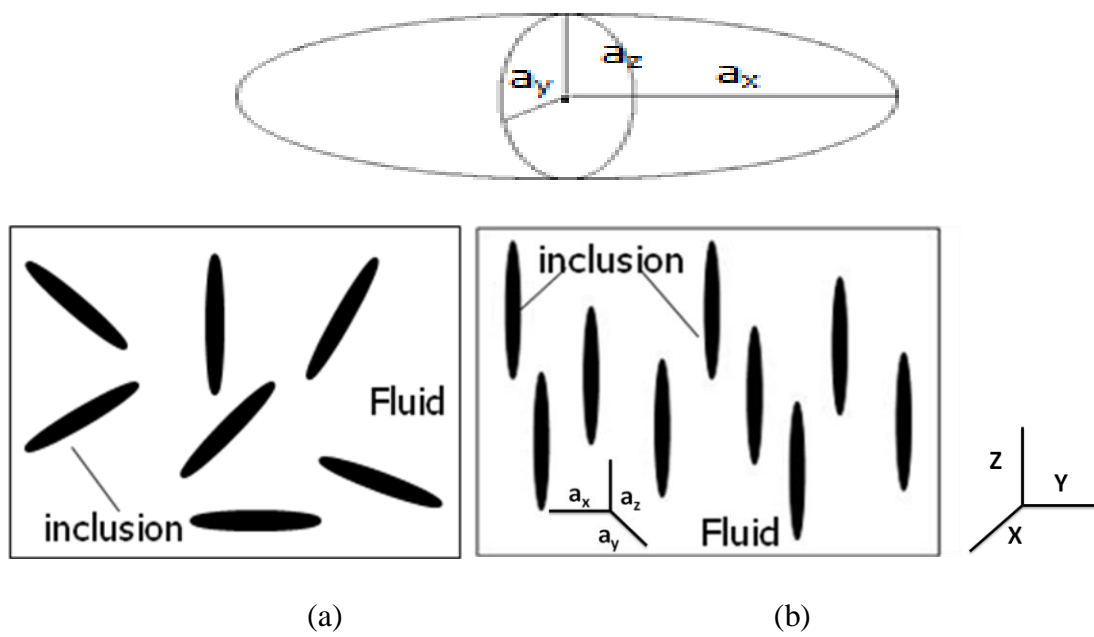
Figure 2.8   Different inclusion orientation (a) random orientation

(b) z-aligned orientation.

CHAPTER III

RESULTS AND DISCUSSIONS

3.1   Characterization of Alignment of Titanium Dioxide

3.1.1   Titania Nanowhiskers

3.1.1.1 Particle Alignment

Titanium dioxide was chosen for this study as it can be obtained in different shapes and sizes with relatively high dielectric constant (around 100) value. First, using the steps described in Section 2.4, 0.2 wt% titania nanowhiskers (anatase, 10 nm x 40 nm) were dispersed in oil. The dispersion was then poured into the gap between the parallel electrodes (shown in Figure 2.6) and an AC electric field was applied. The amplitude and frequency of the applied electric field was adjusted using a function generator and a voltage amplifier. The entire process was observed under the transmission OM. Upon application of AC electric field, titania nanowhiskers rotated and aligned in the direction of applied electric field. As the applied electric field was increased from 100V/mm to 1000V/mm, more chains formed. The alignment of the particles was related to the time duration and frequency of applied field.

A summary of OM images (alignment matrix) documenting the dependence of chain formation on time duration and frequency of electric field are shown in Figure 3.1. The external AC electric field applied was 1000 V/mm with frequency ranging from 100 mHz to 1 kHz. The top row in Figure 3.1 shows the random dispersion prior to application of electric field. The images show that we indeed achieved a uniform

dispersion through mechanical shear mixing and bath sonication. The nanoparticles response to applied electric field depended on the frequency of the field. At low frequencies, between 100 mHz and 1Hz, no visible chains formed within the first 30 minutes of the application of electric field. After 30 minutes however, the particles started forming long chains parallel to the applied electric field. One hour after the application, thin parallel chains were formed between the electrodes. As the frequency of the applied field increased to 10 Hz, visible chains formed at 30 minutes, and the chains became clearer and thicker at 1 hour from the time of application of the field. It was also noticeable that the gap between the chains became wider as the duration of the electric fields increased. At high frequency electric fields (up to 1 kHz), the particles could form visible chains more quickly, at around 10 minutes. After 30 minutes the chains became thicker and the distance between the chains also increased. At the end of 1 hour, very thick and highly dense chains were formed which presumably were comprised of many thin chains. For all samples, the alignment became stable after 1 hour application of the electric field. This indicated that our system achieved equilibrium with no significant variation of the microstructure after 1 hour of the electric field application. From the experimental results shown in Figure 3.1, the chain formation of the nanoparticles dispersion was dependent on the frequency and duration of the applied electric field. The increase in each of the two variables , namely frequency and duration, could achieve increased thickness and clarity of the chains leading to enhanced alignment stability.
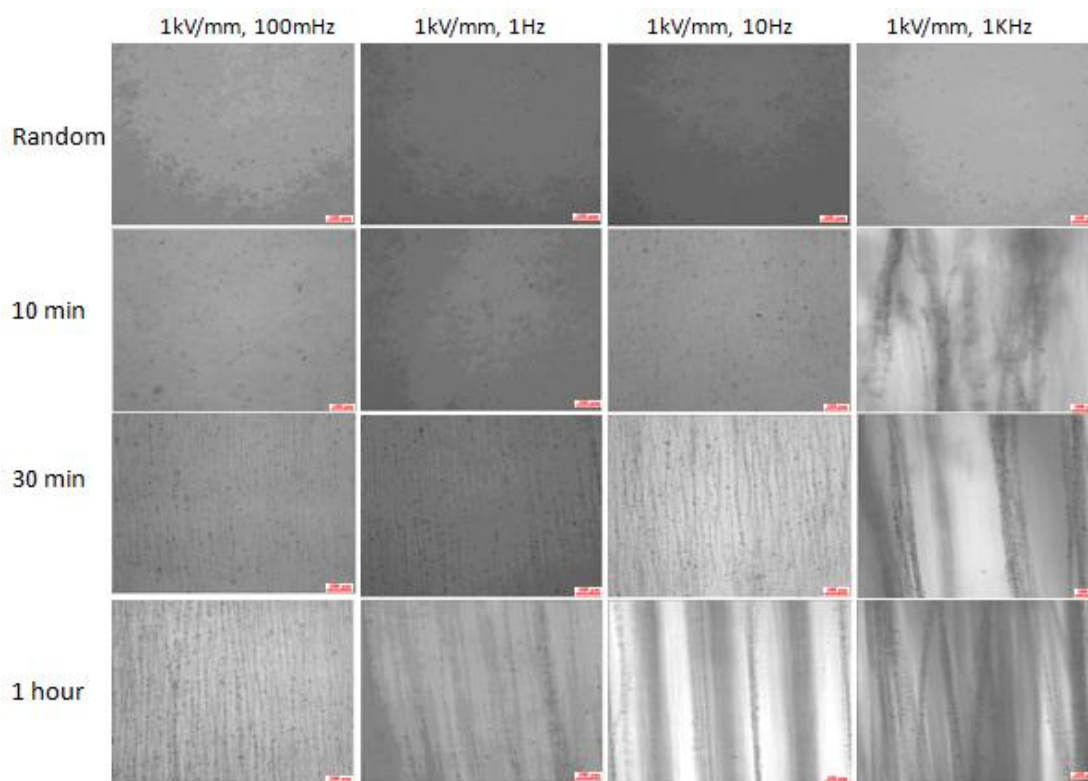
Figure 3.1   Optical microscopy images of 0.2 wt% titania nanowhiskers-oil system under an applied electric field of 1000 V/mm, different alignment frequencies (100 mHz to 1 kHz) and different time intervals (0-1 hour). The scale bar is 100 μm.

3.1.1.2 In-situ Measurement of Dielectric Constant

The dielectric constant was measured for the aligned nanoparticle dispersions using LCR meter. The alignment can be qualified by these in-situ electrical measurements. The results indicate that the aligning conditions have substantial impact on the dielectric properties. Dielectric constant of 0.2 wt% titania nanowhiskers-oil dispersion under applied electric field of 1000 V/mm, 100 mHz to 1 kHz, 1 hour, are

shown in Figure 3.2. It should be pointed out that the dielectric constant of 3-IN-ONE®
oil is around 2 while the dielectric constant of TiO_2 powder is around 100 (about 50
times higher).

Figure 3.2   In-situ dielectric constant of 0.2 wt% titania nanowhiskers-oil system
under an applied electric field of 1000 V/mm, at different alignment frequencies (100
mHz to 1 kHz), at 1 hour. The random case is shown for comparison.

We also investigated the relationship between the dielectric constant with both
the frequency of measurement and the frequency of external applied electric field used
for alignment. From the results shown in Figure 3.2, the dielectric constants of the
nanoparticle dispersion in both random case (without applied electric field, E=0) or

aligned case (E≠0) decreased as the measurement frequency increased in the range of 100 Hz to around 10 kHz. The dielectric constant values showed little variation at higher measurement frequencies (from 10 kHz-1 MHz). If we compared the dielectric constant of the sample under different frequencies of applied electric fields, there was almost no increase compared with the random case when low frequency electric field (100 mHz and 1 Hz) was applied. A small increase in dielectric constant was observed when the frequency of applied field was increased to 10 Hz. And a relatively high dielectric constant, around 2.4, was detected when the applied electric field was 1 kHz.

Figure 3.1 helps us understand the mechanism of the variation of the dielectric constant at different electric field frequencies. From Figure 3.1, only few thin chains can be seen under low frequency (100 mHz and 1Hz). This will lead to little variation of dielectric constant in the low alignment frequency cases compared to that in random case observed in Figure 3.2. On the other hand, there were thicker chains formed in the case where the applied electric field frequency was 10 Hz. This is the reason that caused the dielectric constant increase. In Figure 3.1, it can be seen that the thickest chains were formed when the alignment frequency was 1 kHz. These thick chains contribute to the largest change in dielectric constant which is consistent with the results shown in Figure 3.2.

3.1.2   Titania Acicular

3.1.2.1 Particle Alignment

0.2 wt% titania acicular (FTL-100) dispersion in oil was prepared as per the steps described in Section 2.4. Electric field manipulation of dispersion was carried out using

the steps explained in Section 3.1.1.1. A summary of OM images of particle alignments at different applied electric field frequency and time duration are shown in Figure 3.3. A 1000 V/mm AC electric field was applied to the sample at frequencies ranging between 100 mHz and 1 kHz. The top images show the random dispersions without applied electric field. In this case, as expected, the nanoparticles were dispersed uniformly in the oil. Under the application of the electric fields at the different frequencies, the chains of particles were clearly formed after around 20 minutes from application. The chains became clearer as duration time increasing. Also, from Figure 3, we observed thick chains with large gaps between them. However, width of visible chains and gaps got smaller with increase in the frequency of applied field.

3.1.2.2 In-situ Measurement of Dielectric Constant

Dielectric constant of 0.2 wt% FTL-100-oil dispersion under 1000 V/mm, 100 mHz applied electric field for 1 hour, are shown in Figure 3.4. The dielectric constant in random case and in case of aligned samples with low electric field frequency (100 mHz and 1 Hz) did not any significant difference. When the applied electric field frequency was increased to 1 kHz, the effective dielectric constant significantly increased up to around 2.8. Compared with titania nanowhiskers-oil system, the same concentration of FTL-100-oil dispersion exhibited higher effective dielectric constant.
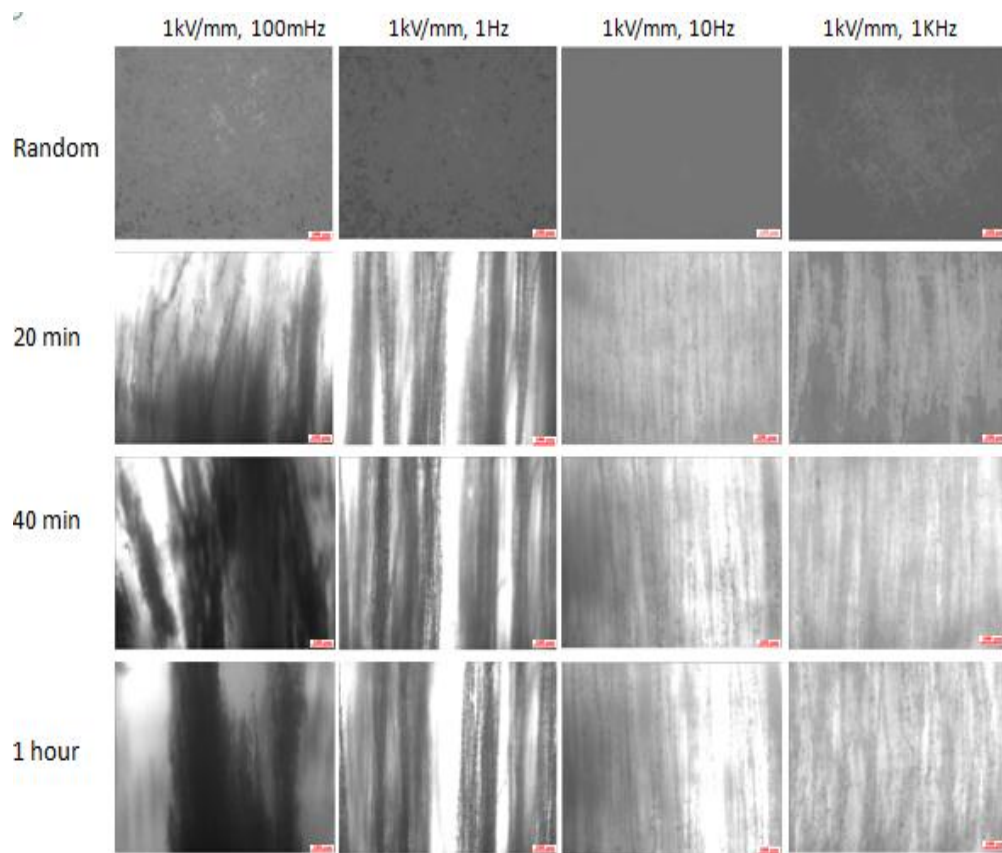
Figure 3.3   Optical microscopy images of 0.2 wt% FTL-100-oil system under an

applied electric field of 1000 V/mm, different alignment frequencies (100 mHz to 1 kHz)
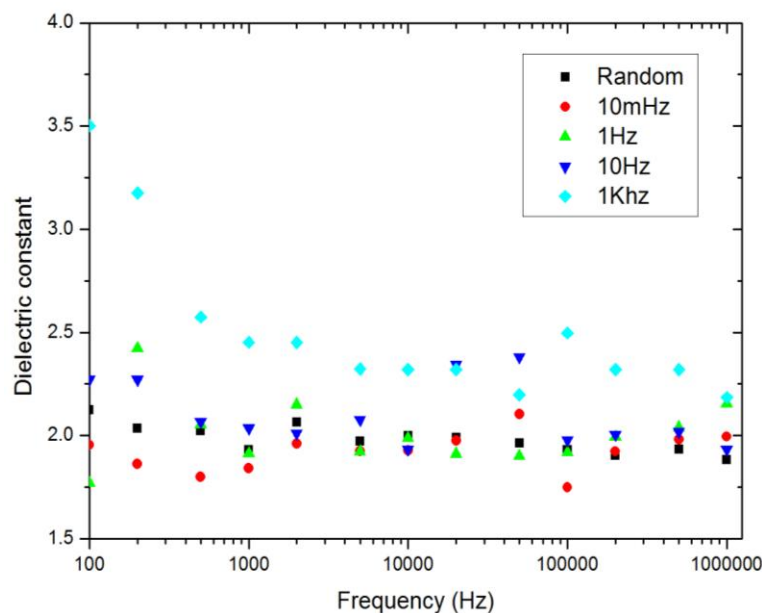
and different time intervals (0-1 hour). The scale bar is 100 μm.
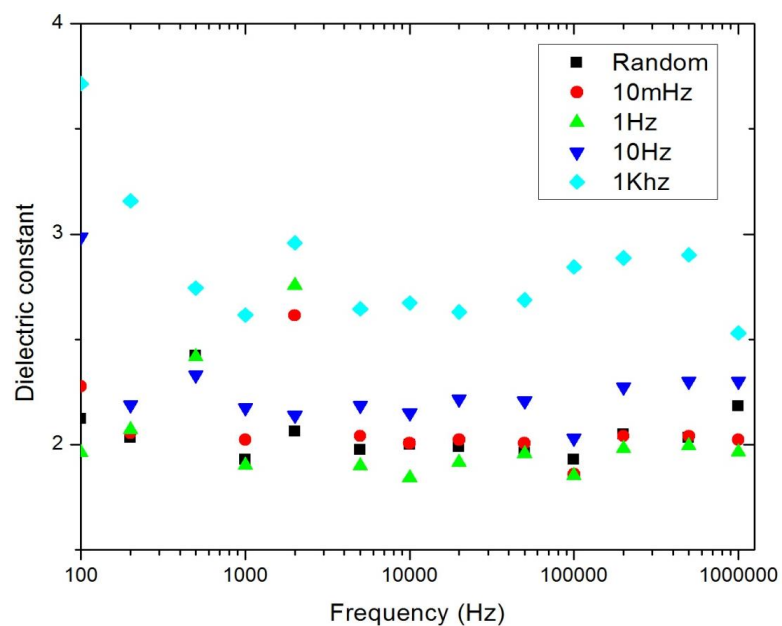
Figure 3.4   In-situ dielectric constant of 0.2 wt% FTL-100-oil system under an

applied electric field of 1000 V/mm, at different alignment frequencies (100 mHz to 1

kHz), at 1 hour. The random case is shown for comparison.

3.1.2.3 Comparison of Dielectric Constant of Different Concentrations

Four different concentrations of FTL-100-oil dispersions were prepared: 0.2%, 1%, 2.5% and 5% weight percent. Comparison of the dielectric constant these dispersions under applied 1000 V/mm, 100 mHz applied electric field for 1 hour, are shown in Figure 3.5 (a), (b), (c) and (d). The effective dielectric constant of each sample shows the highest value for 1 kHz applied electric field frequency. For 1 kHz application, the dielectric constant increased from 2.8 to 3.4 when the nanoparticles content increased from 0.2 wt% to 5 wt%. These results indicate that the concentration of dispersions played an important role in the variation of effective dielectric constant along with magnitude, frequency and duration of applied electric field.

High concentration of nanoparticles is a good way to achieve high dielectric constant. Unfortunately, the high concentration of TiO_2-oil dispersion is limited by processing challenges. Although efforts have been made to process high concentration dispersion by increasing rotation speed of the mechanical stirrer and extending the time of bath sonication, nanoparticle agglomeration still remains a major hurdle. It is challenging to obtain homogeneous dispersion at concentration higher than 10%.
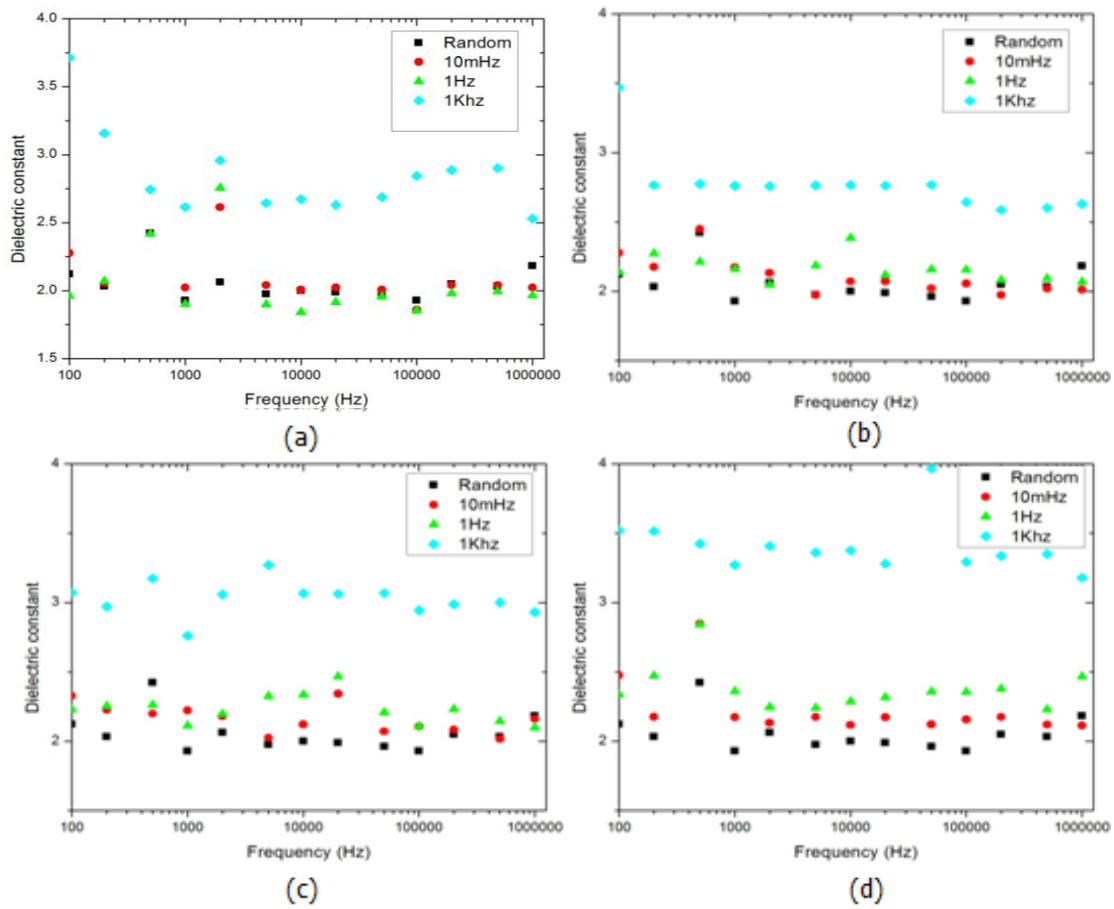
Figure 3.5   Comparison of dielectric constant of different concentrations of 0.2 wt% Titania acicular-oil system under an applied electric field of 1000 V/mm, different frequencies (100 mHz to 1 kHz), 1 hour and random case. (a) 0.2 wt% FTL-100, (b) 1 wt% FTL-100, (c) 2.5 wt% FTL-100, (d) 5 wt% FTL-100.

3.2   Modeling Using Maxwell-Garnett Mixing Rule for TiO_2

According to the experimental data shown in Section 3.1, the titanium dioxide (TiO_2) might not satisfy the requirement to provide relatively high dielectric constant required for switchable antenna system. In order to verify this hypothesis, modeling using Maxwell-Garnett mixing rule was used to simulate the dielectric property of the colloidal base materials.

First, the aligned orientation was considered, and the simulation results were shown in Figure 2.9 (b). The aspect ratio of titania nanowhiskers is around 4 and that of FTL-100 is around 13. Because both weight percent and density of TiO_2 were already known, we could convert the weight percent of the dispersion to volume fraction. Based on the volume fraction, the depolarization factors of inclusions were calculated using Equation (2.4) and (2.6). Because the experimental data in Section 3.1 has indicated that it is very hard to get very high concentration dispersion, we assumed the dielectric constant of particles was 100, weight percent of FTL-100 was 0-20%, and aspect ratio were between 4 to 20. The dielectric constant was calculated at different weight percent and aspect ratio using Equation (2.8) in Matlab. The dependence of dielectric constant on weight percent and aspect ratio is shown in Figure 3.6 (a). Then, results for dielectric constant were calculated by changing the dielectric constant of particles to 80-100, weight percent to 5 wt%, and aspect ratio to 4-20, as shown in Figure 3.6 (b).

From the simulation results shown in Figure 3.6, it is clear that the maximum effective dielectric constant of solution is much less than 6 even if the TiO_2 can be prepared to having 20 aspect ratio, 100 dielectric constant and 20 wt% dispersion.

Although there are many assumptions used in the derivation of Equation (2.8), and the aligned orientation used in our simulation is an ideal case, the simulation demonstrate that TiO_2 cannot provide high enough dielectric constant as is needed for the switchable antenna system. The better solution for this problem is to find another material to replace TiO_2 which can provide high enough dielectric constant and work for a switchable antenna system. $BaTiO_3$ exhibits a much higher dielectric constant (around 1000-1500) as compared to TiO_2. The preparation methods and basic properties of $BaTiO_3$ were described in detail in Section 1.1. The simulation results for dielectric constant of $BaTiO_3$ were calculated based on the basic properties of $BaTiO_3$ using Maxwell-Garnett mixing rule. Figure 3.7 compares the dielectric constant values for $BaTiO_3$ and TiO_2 in the aligned configuration. The dielectric constant in the case of both materials under different aspect ratios and volume fractions are displayed in the graph. From Figure 3.7, it is clear that the effective dielectric constant of $BaTiO_3$ dispersion is much higher than that of TiO_2 dispersion and especially for the high aspect ratio case. Therefore, our requirements for colloidal base materials of high effective dielectric constant can be satisfied by $BaTiO_3$ particles.
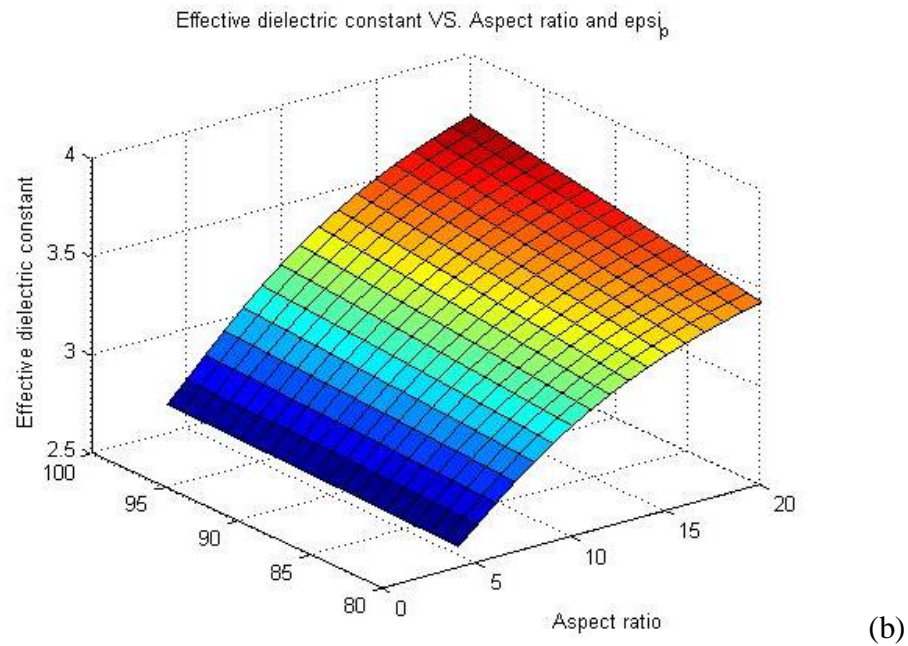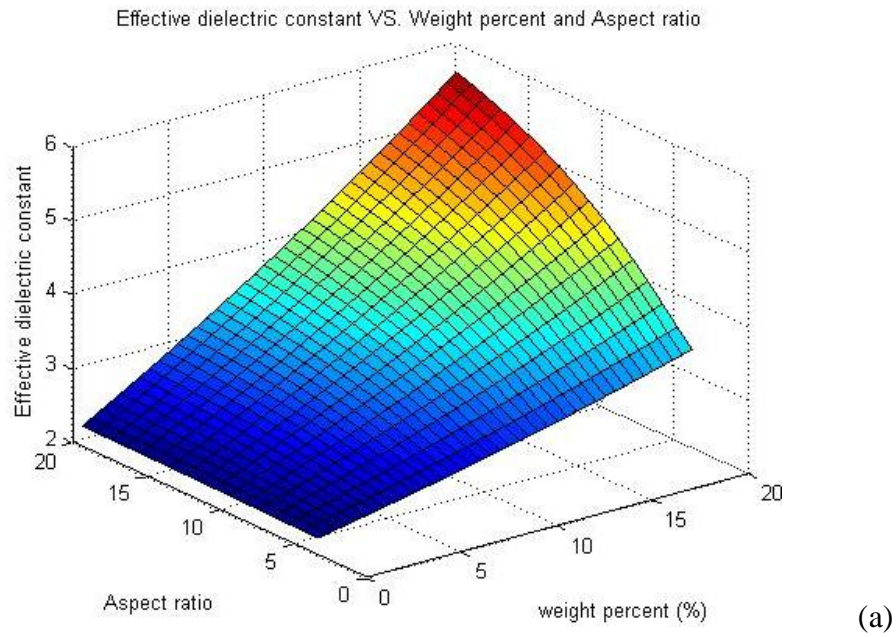
Figure 3.6   3-D simulation of TiO_2 using Maxwell-Garnett Mixing Rule. (a)

Dielectric constant of particles is 100, weight percent is 0-20%, and aspect ratio is 4-20,

and (b) dielectric constant of particles is 80-100, weight percent is 5%, and aspect ratio

is 4-20.

Effective dielectric constant
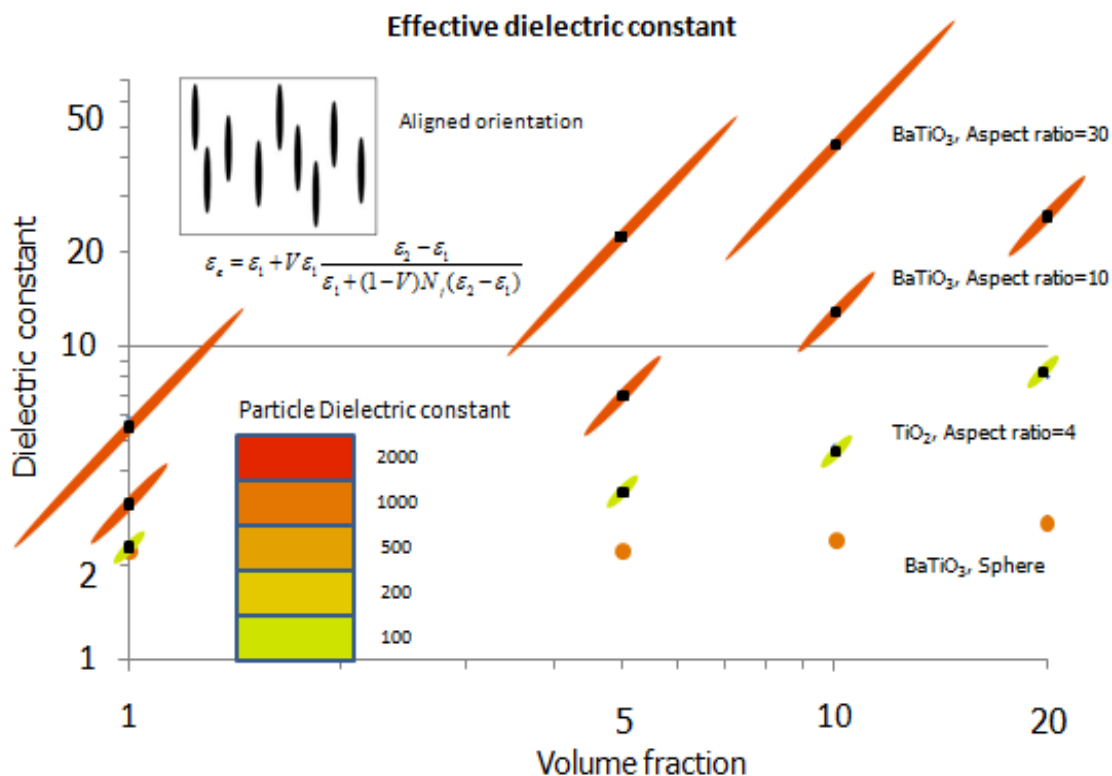
Figure 3.7   Simulation of effective dielectric constant of different TiO$_2$ and BaTiO$_3$.

The black square dots are the real value. The shape and color show the particle

properties.

3.3   Characterization of Alignment of Barium Strontium Oxide (BSTO)

BSTO spherical nanoparticles can demonstrate higher dielectric constant as compared to spherical BaTiO$_3$ particles. Therefore, BSTO spheres were selected for our experiment. Samples with 1 wt% BSTO spheres dispersed in oil were prepared. A summary of OM images of the particle alignment under different conditions of applied electric field frequency and time duration are shown in Figure 3.8. A 1000 V/mm AC

electric field was applied to the samples. The frequencies of the applied electric fields ranged from 100 mHz to 1 kHz. From Figure 3.8 it can be seen that the nanoparticle chains become clearer, at all frequencies, as the time duration of the applied electric field. It should be mentioned that at higher frequency the chain formation process was faster. Therefore, higher frequency and longer duration of the applied electric fields improve the alignment. Figure 3.9 shows the dielectric constant as a function of test frequency for 1 wt% BSTO-oil dispersion (1000 V/mm applied electric field, at 100 mHz to 1 kHz and 1 hour duration). The effective dielectric constant can be as high 3.5 under 1 kHz applied electric field. Although the BSTO-oil dispersion used was only 1 wt%, its effective dielectric constant is higher than the 5 wt% FTL-100-oil dispersion. This confirms that aligned BSTO dispersion exhibits higher effective dielectric constant as compared to TiO_2 and can be a more suitable material for our requirements. The 5 wt% BSTO-oil dispersion was prepared for further study of this material. Dielectric constant values of 5 wt% BSTO-oil dispersion under applied electric field of 1000 V/mm, 100 mHz to 1 kHz frequencies and 1 hour time duration are shown in Figure 3.10. The effective dielectric constant of 5 was achieved for 1 kHz applied electric field. When these results were compared to those of 1 wt% BSTO-oil and TiO_2-oil dispersions (at same magnitude of electric field), the effective dielectric constant of 5 wt% BSTO-oil was much higher. Therefore, BSTO exhibited the highest effective dielectric constant within the commercially available materials. However, this effective dielectric constant of BSTO was still not high enough for our goal. In order to obtain higher dielectric colloidal-based dispersion, high aspect ratio $BaTiO_3$ nanoparticles were considered.

Although the high aspect ratio BaTiO$_3$ nanoparticles are not commercially available, high aspect ratio BaTiO$_3$ nanowires can be synthesized.
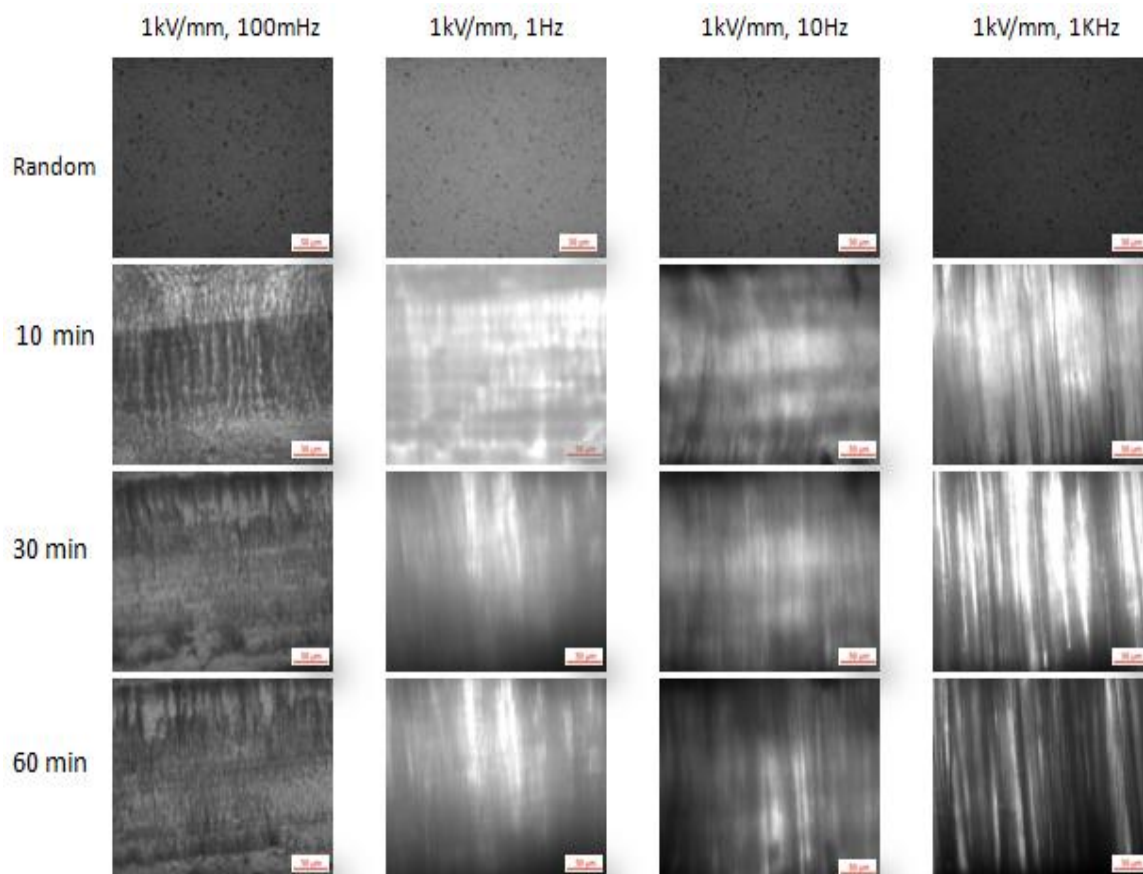
Figure 3.8   Optical microscopy images of 1 wt% BSTO-oil system under an applied electric field of 1000 V/mm, different frequencies (100 mHz to 1 kHz) and different time intervals (0-1 hour). The scale bar is 50 μm.
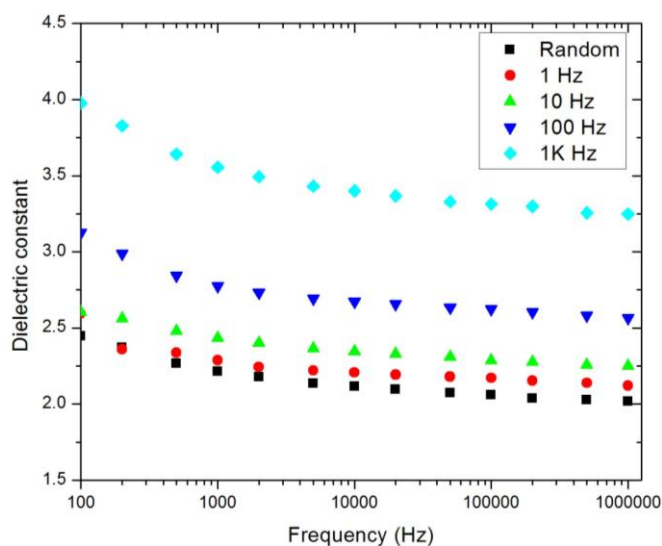
Figure 3.9   In-situ dielectric constant of 1 wt% BSTO-oil system under an applied

electric field of 1000 V/mm, at different alignment frequencies (100 mHz to 1 kHz), at 1

hour. The random case is shown for comparison.
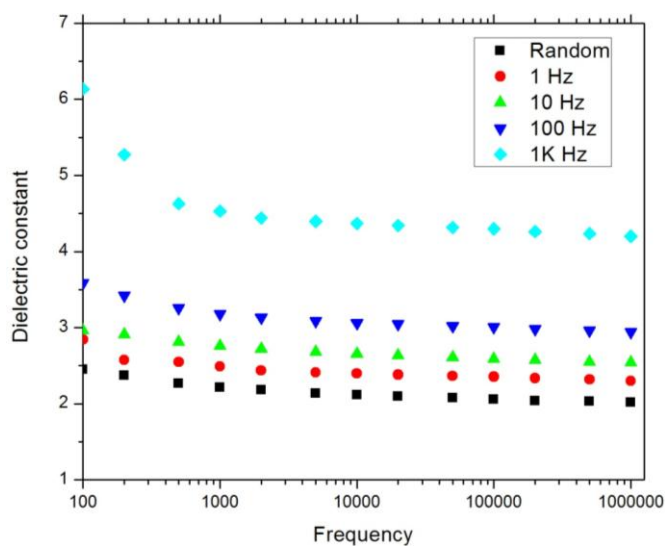
Figure 3.10   In-situ dielectric constant of 5 wt% BSTO-oil system under an applied

electric field of 1000 V/mm, at different alignment frequencies (100 mHz to 1 kHz), at 1

hour. The random case is shown for comparison.

3.4   Synthesis and Characterization of High Aspect Ratio BaTiO3

3.4.1   Synthesis BaTiO$_3$ Nanowires Using Quartz Crucible

Single crystalline, high aspect ratio BaTiO$_3$ nanowires were synthesized using the molten salt method which was developed based on the method reported by Yuanbing et al [56]. The processing technique used was described in detail in Section 2.3. The processing technique was modified to include probe sonication to evenly mix the sample. Also, a centrifuge was used to clean the sample instead of water wash. The purpose for these improvements was to reduce the secondary phase products or impurities, and obtaining better BaTiO$_3$ nanowires. The BaTiO$_3$ nanowires samples (named as BTO #1) were prepared using the method introduced in Section 2.3. As mentioned in Section 2.3, a high temperature crucible was chosen in the synthesis. SEM, XRD, and EDS Mapping were used to characterize the as-prepared products.

The BaTiO$_3$ samples with different cleaning processes were also compared. The SEM images of BTO#1 without any cleaning process employed are compared with those employing centrifuging and water wash are shown in Figure 3.11 (a), (b), (c)and (d). Figure 3.11(a) shows the SEM image of the sample that did not employ any cleaning process. From Figure 3.11 (a), it was hard to see any nanowires, and it seemed most of the samples are impurities. In Figure 3.11 (b), after centrifuging the samples for 10 times, some of the impurities were removed and several nanowires could be observed. However, a large proportion of impurities could be observed in Figure 3.11 (b), which limited the purity of the products. Figure 3.11 (c) shows the SEM of samples centrifuged and water washed for 10 times. The impurities appear reduced compared to the Figure

3.11 (b), and the nanowires could be clearly observed. Finally, the SEM image of the BTO sample centrifuged 10 times and water washed 30 times is shown in Figure 3.11 (d). From 3.11 (d), it can be observed that most of the samples are nanowires with little impurities. The images shown in Figure 3.11 indicate that the cleaning processes, including centrifuge and water wash, played an important role in purifying the sample. High purity samples could be obtained by choosing suitable cleaning processes.

A representative XRD pattern of the as-synthesized BTO#1 (20 times centrifuged and 50 times water washed) is shown in Figure 3.12. The diffraction peaks in Figure 3.12 can be assigned to two different materials: $BaTiO_3$, and Fresnoite, $Ba_2TiSi_2O_8$ (BTS). In Figure 3.12, the black five-pointed star indicates the peak belonging to BTS and the red-cross star indicates the peak that belongs to $BaTiO_3$. It is interesting that the secondary phase of BTS was also created. In the typical reaction, all of the raw materials (BaC_2O_4, TiO_2, NaCl and NP-9) do not contain the element Si. However, the XRD result in Figure 3.12 clearly shows the existence of BTS. Close inspection of the processing technique indicated that the only possible reason was the contribution of the quartz crucible (SiO_2). BTS may be the reaction product of precursors and the quartz crucible. $BaTiO_3$ was created following the reactive chemical formula shown in Equation 3.1. $BaTiO_3$ reacts with SiO_2 at the temperature range 700 ℃-1200 ℃, as shown in Equation 3.2.

$$BaC_2O_4 + TiO_2 \rightarrow BaTiO_3 + CO_2 + CO \qquad (3.1)$$

$$2BaTiO_3 + 2SiO_2 \rightarrow Ba_2TiSi_2O_8 + TiO_2 \qquad (3.2)$$
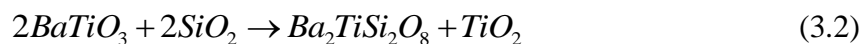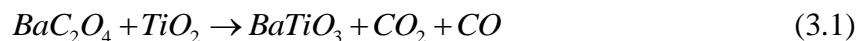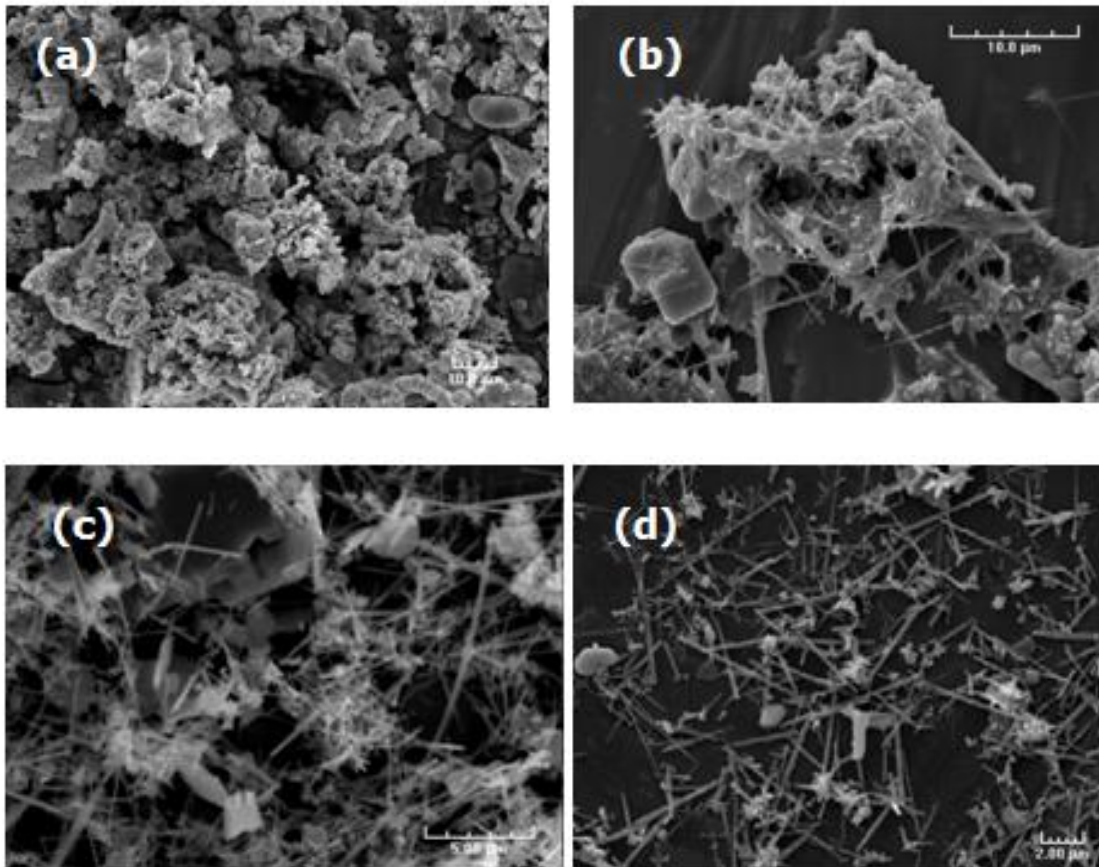
Figure 3.11   SEM images of BTO #1 after different times centrifuge and water wash.

(a) Without any cleaning process, the inset bar is 10 μm, (b) after 10 times centrifuge,

inset bar is 10 μm, (c) after 10 times centrifuge and 10 times water wash, the scale bar is

5 μm, and (d) after 10 times centrifuge and 30 times water wash, the scale bar is 2 μm.
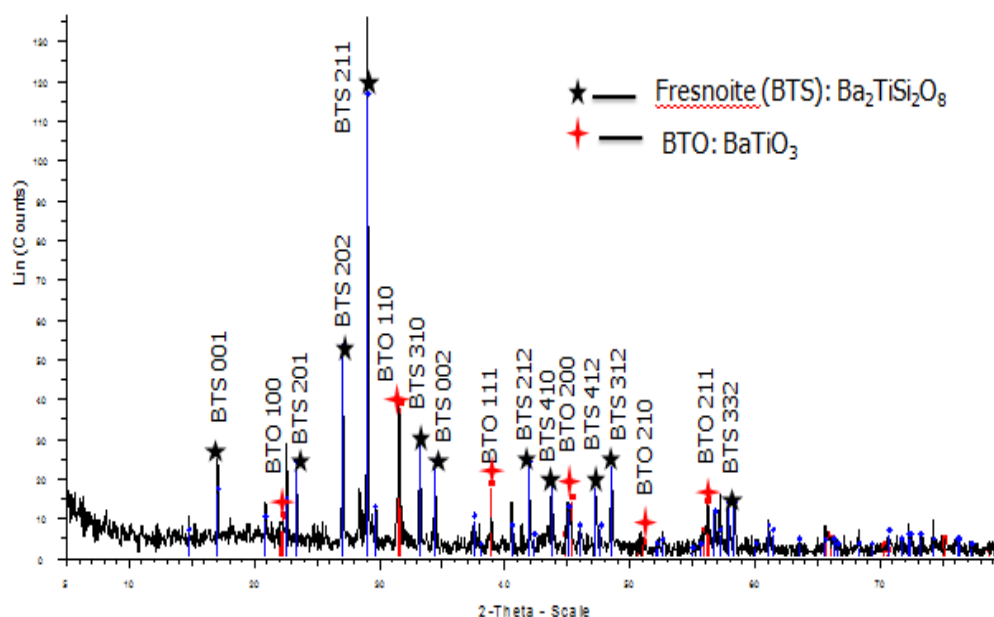
Figure 3.12   XRD pattern of the synthesized BTO #1 products (820 °C, 3.5 h).

For accurate analysis of the BTO #1 composition, EDS mapping was used to understand the distribution of elements in the sample. The SEM image of BTO #1 nanowires shown in Figure 3.13 (a) shows irregularly shaped impurities in BTO #1. Figure 3.13 (b), (c), and (d) show the EDS X-ray maps of barium (Ba), titanium (Ti) and silicon (Si), respectively. Here each pixel is representative of the raw number of counts in the element's region of interest in the EDS spectrum. The maps show the nanowires contain Ba and Ti elements but do not have any Si element. Also, from Figure 3.13 (b), (c) and (d), the impurities contain all elements: Ba, Ti and Si.
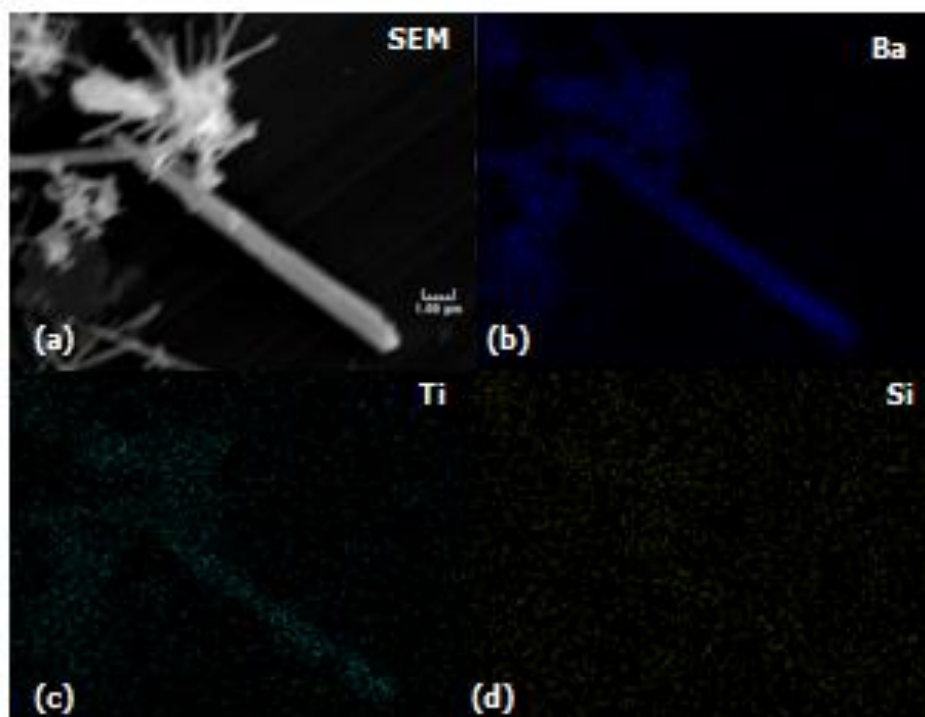
Figure 3.13   SEM image and EDS mapping of nanowires in BTO #1. (a) SEM image

of nanowires, the scale bar is 1 μm. (b) EDS X-ray maps of Ba, (c) EDS X-ray maps of

Ti, and (d) EDS X-ray maps of Si.

Combining the results from SEM, XRD and EDS mapping, we can draw a

conclusion that synthesis process of BaTiO$_3$ nanowires using quartz crucible will lead to

second-phase product BTS except for BaTiO$_3$ nanowires. BTS took large amount of

prepared BTO #1 and existed as irregular shaped impurities in the sample. The reason of

BTS second-phase product is a chemical reaction between quartz crucible and the first

product BaTiO$_3$ at high temperature.
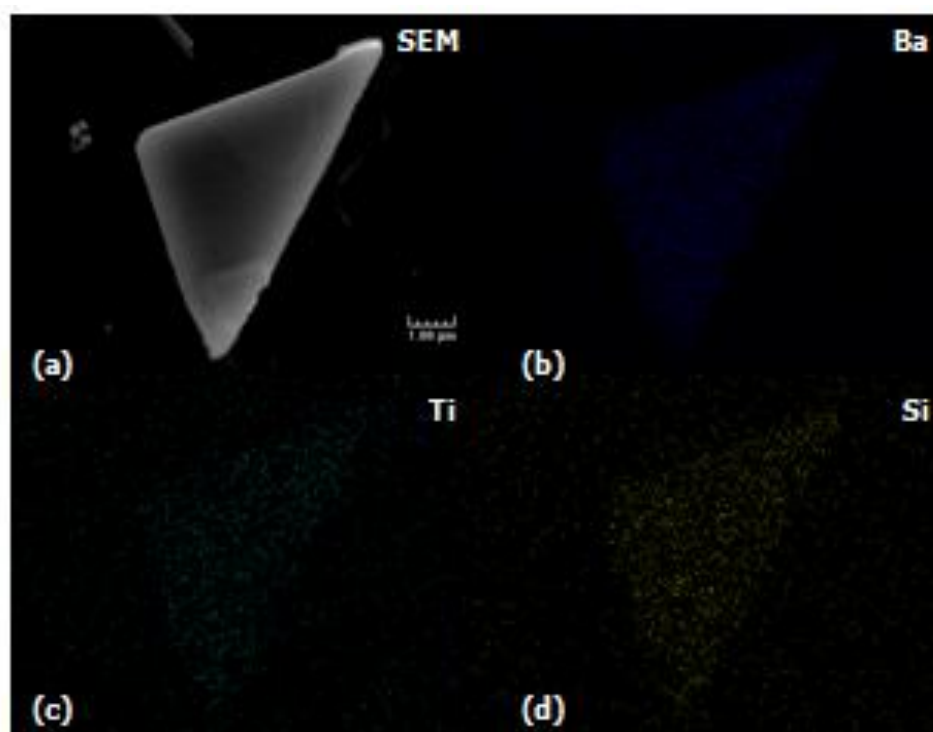
Figure 3.14   SEM image and EDS mapping of impurity in BTO #1. (a) SEM image of

nanowires, the scale bar is 1 μm. (b) EDS X-ray maps of Ba, (c) EDS X-ray maps of Ti,

and (d) EDS X-ray maps of Si.

3.4.2   Synthesis BaTiO$_3$ Nanowires Using Zirconia Crucible

In order to avoid producing second-phase BTS and attain high purity BaTiO$_3$

nanowires in the sample, another high temperature crucible, zirconia crucible (ZrO$_2$,

AdValue Technology, 35ml) was used instead of quartz crucible in our experiments.

New BaTiO$_3$ nanowires samples (named BTO #2) were prepared through the process

introduced in Section 2.3. The as-prepared products (820 °C, 3.5 h) were also

characterized by SEM, XRD, and EDS Mapping. Figure 3.15 shows the SEM image of

the as-prepared BaTiO$_3$ nanowires (BTO #2). From Figure 3.15 (a), it can be clearly seen that the products are quite uniform and mainly consist of well-defined straight, smooth, and crystalline nanowires. The nanowires have diameter ranging from 100 nm to 300 nm, and their lengths range from 1.5 μm to 5 μm. A closer examination of single BaTiO$_3$ nanowire is shown in Figure 3.15 (b).
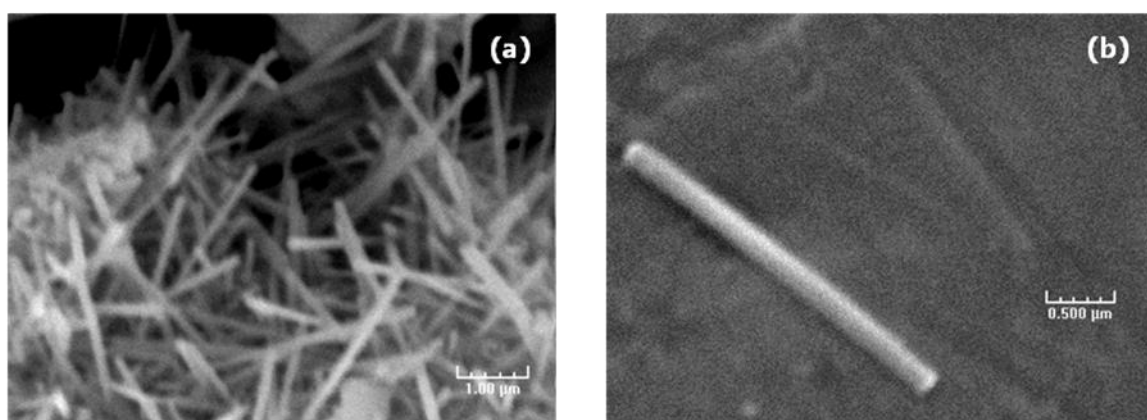
Figure 3.15   SEM images of the synthesized BaTiO$_3$ nanowires (BTO #2). The scale bar is (a) 1 μm, and (b) 0.5 μm.

The purity and crystallinity of the as-prepared BaTiO$_3$ samples were examined using XRD. The XRD data of BaTiO$_3$ sample (BTO #2) is shown in Figure 3.16. Very few peaks attributable to impurities are observed in the sample. All the peaks in the pattern can be well indexed with the JCPDS card (31-0174), which demonstrates that the samples demonstrate a pure cubic phase. The above results illustrate that the high purity of high aspect ratio BaTiO$_3$ nanowires can be successfully synthesized by the molten salt method. Scaling up this process can produce large scale BaTiO$_3$ nanowires.
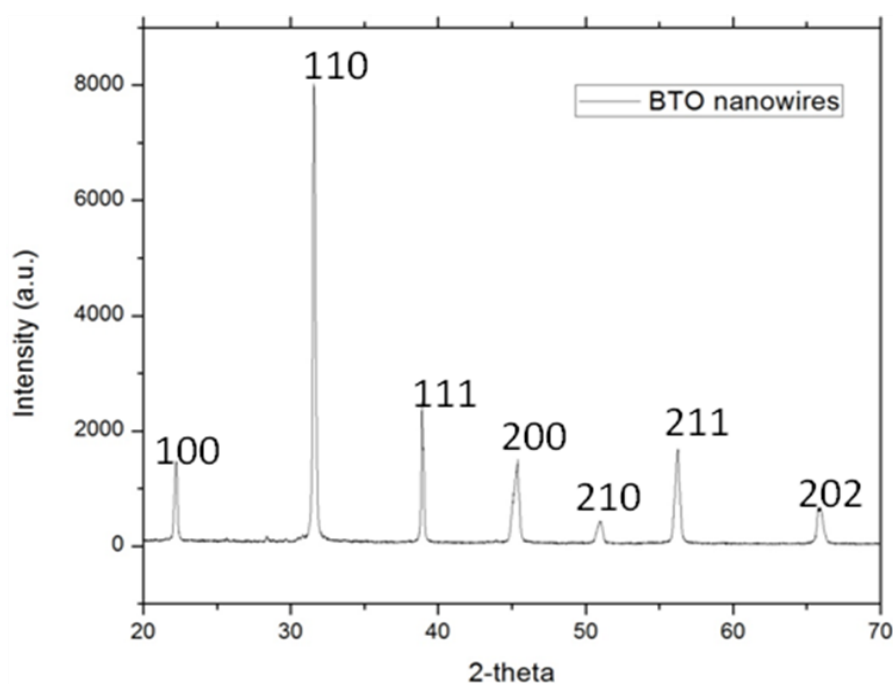
Figure 3.16   XRD pattern of the synthesized BTO #2 products (820 ℃, 3.5 h).

The prepared BTO #2 powders were calcined again in high temperature oven for 2 h at temperatures from 1050 ℃ to 1150 ℃. The calcined powders were characterized using XRD. Figure 3.17 (a) shows the XRD patterns of the prepared BTO #2 calcined at different temperatures and Figure 3.17 (b) shows the enlarge images around 43-48 degree (200). For prepared BTO #2, there is a clear shoulder shown before the diffraction peak at $2\theta=45.4$ ℃ (200). If the sample is all cubic structure $BaTiO_3$, the (200) should be a thin peak; if the sample is all tetragonal structure $BaTiO_3$, the split of diffraction peak should be discriminated to (002) and (200). The shoulder is indicated to be the overlap of (002) and (200), it means the BTO #2 is cubic structure mixed with tetragonal structure. As the annealing temperature increased from 1050 ℃ to 1150 ℃,

diffraction peak at 2θ=45.4 ℃ slightly widens and the shoulder becomes more clear. This implies that BaTiO₃ of tetragonal phase increases as annealing temperature increasing. However, it is still difficult to distinguish between (002) and (200), no split of diffraction peak formed, which means cubic structure still plays a major part of the sample.
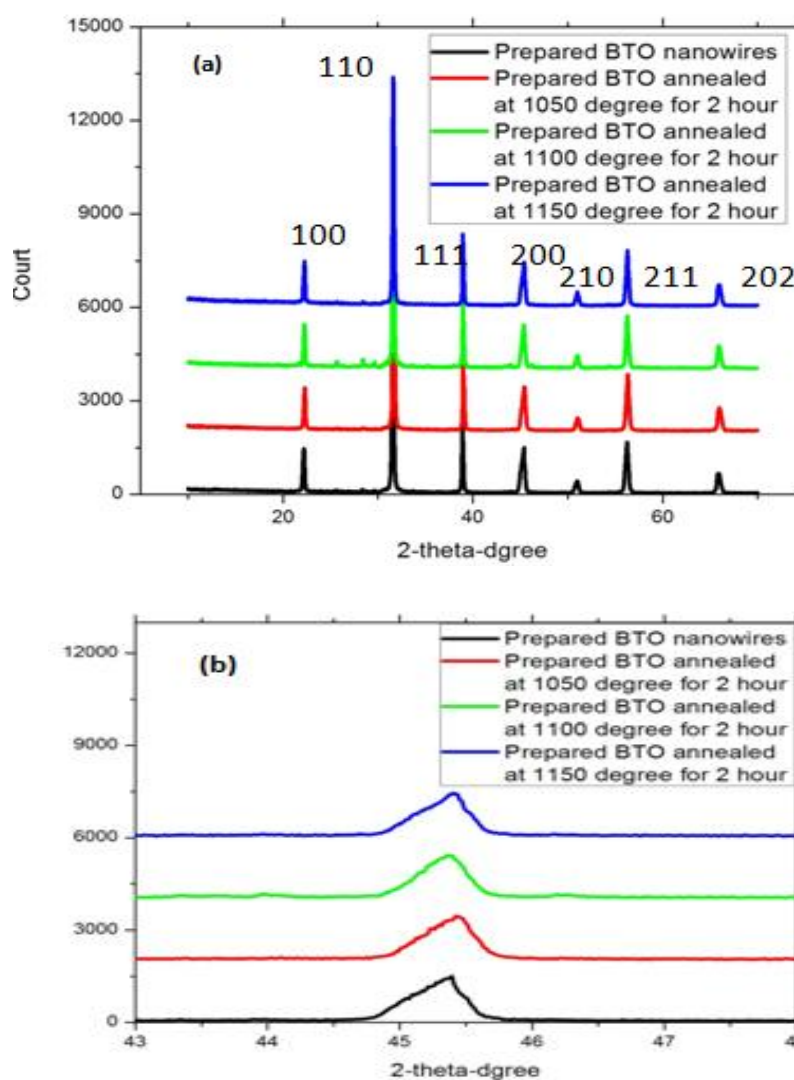
Figure 3.17   (a) XRD patterns of the prepared BTO #2 calcined at 1050 ℃, 1100 ℃ and 1150 ℃, (b) enlarge XRD patterns around 43-48 degree.

3.4.3   Temperature Dependence

Figure 3.18   SEM images of the synthesized BaTiO$_3$ nanowires annealed at different

temperature (BTO #3-BTO #6). (a) BTO #3, annealing temperature 750 ℃, the scale bar

1 μm, (b) BTO #4, annealing temperature 800 ℃, the scale bar 1 μm, (c) BTO #5,

annealing temperature 850 ℃, the scale bar 2 μm, and (d) BTO #6, annealing

temperature 950 ℃, the scale bar 2 μm.

A series of tests were carried out to understand more fundamental properties of

BaTiO$_3$ nanowires. The precursors were heated in a high temperature oven to 750 ℃,

800 ℃, 820 ℃, 850 ℃, and 950 ℃ for 3.5 hours. The precursors consisted of BaC$_2$O$_4$,

TiO$_2$ (anatase, 15 nm) and surfactant NP-9 in molten salt (NaCl). The high temperature Zirconia crucible was used in these tests. The SEM images of the as-prepared BaTiO$_3$ nanowires annealed at different temperatures:750 ℃ (BTO #3), 800 ℃ (BTO #4), 850 ℃ (BTO #5), and 950 ℃ (BTO #6) are shown in Figure 3.18 (a), (b), (c), and (d) respectively.

When the precursors were heated at 750 ℃ for 3.5 h, the obtained BTO #3 consisted of BaTiO$_3$ nanocubes of about 100 nm in diameter, as shown in Figure 3.18 (a). Figure 3.18 (b) shows the SEM image of the product obtained at annealing temperature of 800 ℃. The image indicates that the sample contains a large quantity of BaTiO$_3$ nanowires and a small quantity of BaTiO$_3$ nanorods with 300-500 nm in diameter. Figure 3.18 (c) shows the SEM image of the samples prepared at 850 ℃ annealing temperature. The samples consisted of nanoplates with thickness less than 100 nm. The length and width of nanoplates can go up to 2 μm. The SEM image of the BaTiO$_3$ nanoplates (nanoflowers) obtained at the annealing temperature of 950 ℃ is shown in Figure 3.18 (d). The image reveals that the diameters of the nanoflowers range from 1 to 2 μm at the temperature of 950 ℃. The thickness of the nanoflowers varies from 100 nm to 200 nm. The results shown in Figure 3.18 demonstrate that different BaTiO$_3$ 1D nanostructures can be processed by choosing appropriate annealing temperatures.

3.4.4   Time Dependence

The effect of annealing time on the properties of the as-prepared BaTiO$_3$ nanowires was also studied. SEM images of the as-prepared BaTiO$_3$ nanowires annealed at 820 ℃ for 2.5 hours (BTO #7) and 4.5 hours (BTO #8) are shown in Figure 3.19 (a)

and (b) respectively. Only a few nanowires were produced for annealing time of 2.5 hours (BTO #7), with most of sample consisting of nanocubes with diameter of 100-200 nm. On the other hand for the annealing time of 4.5 hours (BTO #8), the proportion of BaTiO$_3$ nanowires increased significantly compared to BTO #7. The SEM image of BTO #8 shown in 3.19 (b) clearly indicates that BaTiO$_3$ nanowires occupy significant proportion of the sample. Some nanotubes still exist in BTO #8 however their proportion was much lower compared to that in BTO #7. On the other hand, Figure 3.15 shows that very high purity nanowires were processed with annealing time 3.5 hours. The results indicate that the annealing time played an important role in determining the final product states of BaTiO$_3$ particles.
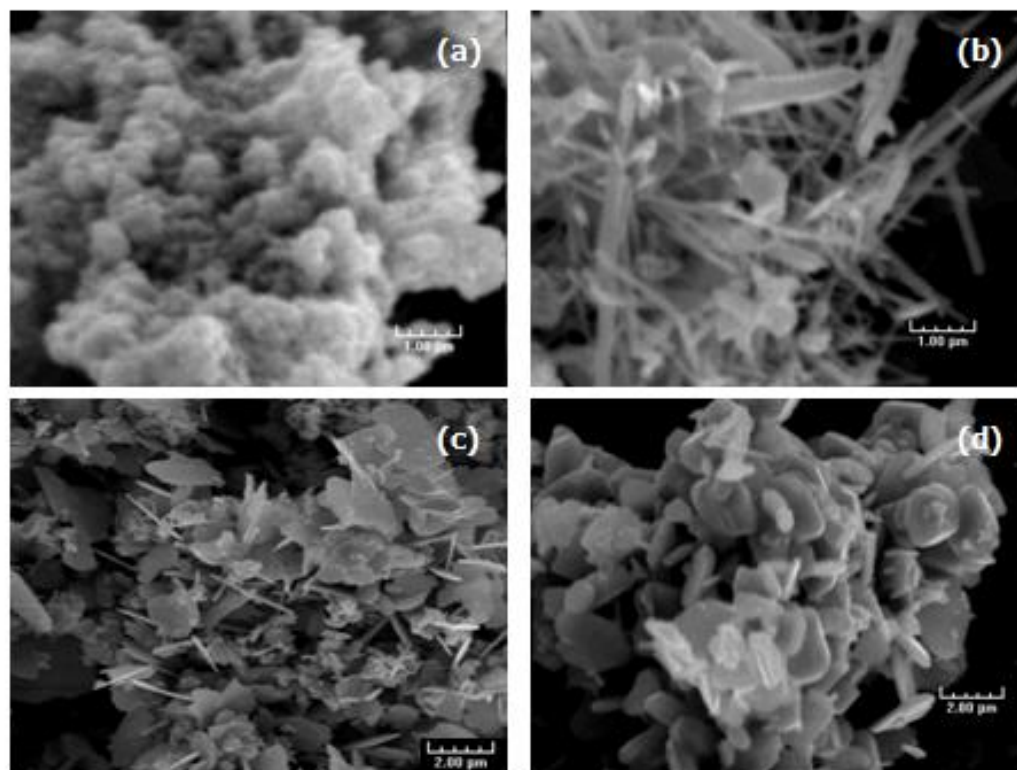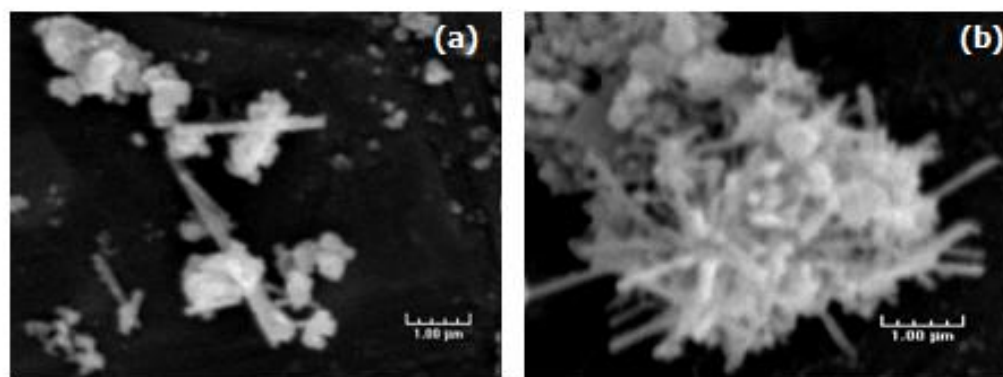

Figure 3.19   SEM images of the synthesized BaTiO$_3$ nanowires annealed at different time (BTO #7-BTO #8). (a) BTO #7, annealing time 2.5 h, the scale bar 1 μm, (b) BTO #8, annealing time 4.5 h, the scale bar 1 μm.

3.4.5   Effect of TiO$_2$ Precursors

Anatase and rutile are the most common observed crystallographic structures in TiO$_2$. The anatase TiO$_2$ nanoparticles were used in previous synthesis processes of BaTiO$_3$ nanowires. In the following studies, several types of rutile TiO$_2$ nanoparticles were used as precursors instead of anatase TiO$_2$ nanoparticles to investigate the effect of TiO$_2$ precursors on the properties of synthesized BaTiO$_3$ nanowires. In order to exclude the influence of other factors, all raw materials and experimental conditions were kept the same. The annealing temperature used was 820 ℃ and annealing time was fixed at 3.5 hours in all the reactions for BaTiO$_3$ nanowires. Two produced BaTiO$_3$ samples, BTO #9 and BTO #10, were prepared using rutile TiO$_2$ with 50 nm diameter and titania nanowhiskers (rutile, 10*40 nm), respectively. The SEM images of BTO #9 and BTO #10 are shown in Figure 3.20 (a) and (b) respectively. From Figure 3.20, both BTO #9 and BTO #10 demonstrate low aspect ratio nanowires and some nanocubes. The diameters of nanowires were between 100 nm to 300 nm and the lengths were typically less than 1 μm. For both BTO samples displayed in Figure 3.20, the aspect ratio of the synthesized BaTiO$_3$ nanowires was around 2-5, which is significantly smaller compared to the 10-20 observed for BTO #2. Therefore, the crystalline phase of precursors could be deterring the shape of the synthesized BTO samples. It can be concluded that the effect of crystalline phase of the precursors should not be ignored in BaTiO$_3$ nanowires processing.
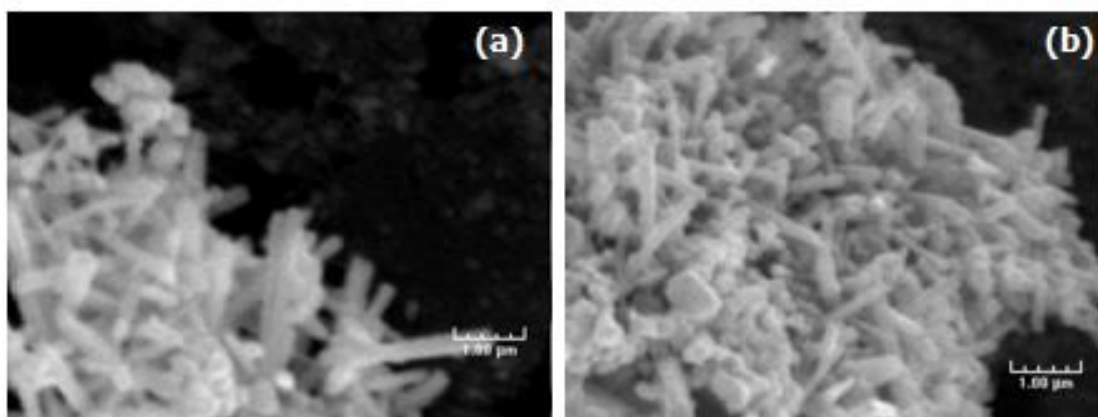
Figure 3.20   SEM images of the synthesized BaTiO$_3$ nanowires using different TiO$_2$ as precursors (BTO #9-BTO #10). (a) BTO #9 (using TiO2, rutile, 50 nm), the scale bar 1 μm, (b) BTO #10(using TiO2, rutile, 10*40 nm), the scale bar 1 μm.

3.4.6   Sensitivity Summary

The XRD patterns of the samples obtained under various reaction conditions are shown in Figure 3.21. From the figures, high purity BaTiO$_3$ nanowires were processed at 820 ℃ for 3.5 hours. A few unapparent impurity peaks were present when the annealing time was decreased to 2.5 hours or increased 4.5 hours. The unidentified peaks might be caused by some other barium titanium oxide materials (Ba$_x$Ti$_y$O$_z$) which were generated in the preparation process. Figure 3.21 also indicates that a second-phase with a composition BaTi$_2$O$_5$ was detected when the TiO$_2$ rutile was used as the precursors. At the same time, some other small peaks from other impurities were also detected in this sample. As the annealing temperature increased to 950 ℃, all the impurity peaks in the pattern of the sample could be well indexed with the Ba$_4$Ti$_{13}$O$_{30}$, which demonstrated that the sample did contain second-phase Ba$_4$Ti$_{13}$O$_{30}$.

From our results we have determined that processing high aspect ratio $BaTiO_3$ nanowires using molten salt method has very high sensitivity to annealing temperature, annealing time and the choice of TiO_2 precursors. A summary of these effects on the $BaTiO_3$ samples and the representative SEM images of the samples are presented in Table 3.1. The highlighted values show the differences of materials or experimental conditions. Single crystal, high purity, and high aspect ratio $BaTiO_3$ nanowires can be synthesized only under certain conditions: by using TiO_2 anatase nanospheres with diameter 15 nm with annealing time of 3.5 hours at 820 ℃. Under these conditions, highest purity of $BaTiO_3$ nanowires could be obtained. Other experiemental conditions resulted in samples with different sizes and shapes which were a function of processing time, processing temperature and the crystalline phase.

From Table 3.1, just nanocubes were synthesized at 750 ℃, since the NaCl melting point is around 800℃, it did not transfer to the liquid state in the reaction of preparing $BaTiO_3$ nanoparticles below this temperature. The crystal state of NaCl hindered the growth of $BaTiO_3$ nanowires from the $BaTiO_3$ nanocubes. It can be predicted that the prepared sample would be $BaTiO_3$ nanocubes when processing temperature is below 800℃. More and more nanowires will be prepared when the temperature is increased from 800℃ and 820℃. As the temperature continues to increase, the nanowires transfer to nanoflowers. It seems that the nanowires form aggregation at high temperature. The diameters and thickness of the nanoflowers increase as the increase of processing temperature. In our current study, the specific mechanism responsible for formation of $BaTiO_3$ nanoflowers is not very clear and

further study is still underway. Moreover, processing time also play an important role in the synthesis. If processing time is not enough, it is hard to ensure the nanocubes can grow up to nanowires. The product will contain large amount of nanocubes. However, overreaction will happen and some nanowires will fracture to short items or nanocubes when the processing time is too long. Furthermore, different TiO_2 precursors also lead to different results. If rutile TiO_2 nanoparticles were used as precursors instead of anatase TiO_2 nanoparticles, the prepared $BaTiO_3$ nanowires will have short aspect ratio. The aspect ratio is just around 2-5, which is significantly smaller compared to the 10-20 obtained using anatase TiO_2 nanoparticles. In a word, high aspect ratio $BaTiO_3$ nanowires processing using molten salt method has very high sensitivity and needs strict control of experimental conditions.
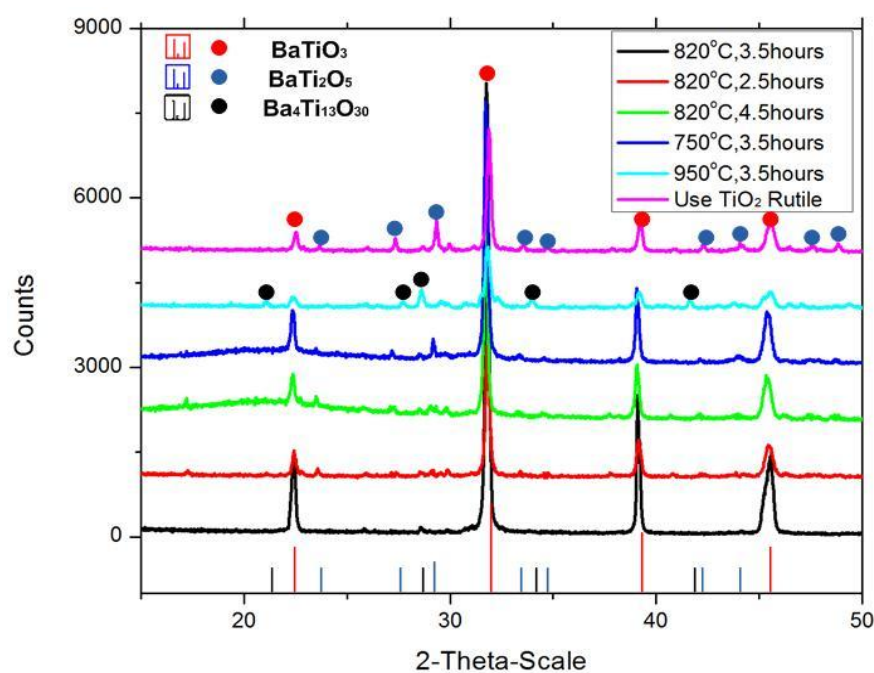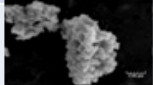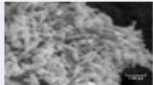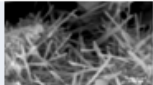
Figure 3.21   XRD patterns obtained under various reaction conditions.

Table 3.1   Sensitivity summary of annealing temperature, time and precursors.

Reaction materials (TiO2)	Pre-heating (Yes/No)	Proces-sing time (hour)	Processing temperature (°C)	Composition (according to XRD pattern)	Shape (Aspect ratio)	SEM
Antanase, 15 nm	Yes	3.5	820	$BaTiO_3$	Nanowires (around 2-10)	
Antanase, 15 nm	No	3.5	750	$BaTiO_3$, $BaTi_2O_5$	Nanocubes (around 1)	
Antanase, 15 nm	No	3.5	950	$BaTiO_3$, $Ba_4Ti_{13}O_{30}$	Nanoflowers (plates)	
Antanase, 15 nm	No	2.5	820	$BaTiO_3$	Nanocubes and Nanowires	
Antanase, 15 nm	No	4.5	820	$BaTiO_3$	Nanocubes and Nanowires	
Rutile, 10*40 nm	No	3.5	820	$BaTiO_3$, $BaTi_2O_5$	Nanowires (around 2-5)	
Rutile, 50 nm	No	3.5	820	$BaTiO_3$, $BaTi_2O_5$	Nanowires (around 2-5)	
Antanase, 15 nm	No	3.5	820	$BaTiO_3$	Nanowires (around 12-15)	

3.5   Characterization of Alignment of $BaTiO_3$ Nanowires

3.5.1   Particle Alignment

The high aspect ratio $BaTiO_3$ nanowires synthesized in our previous experiments were used to prepare dispersion in oil in our study. A summary of OM images of particle alignments in random situation and under different external applied electric fields of 1 wt% $BaTiO_3$ nanowires-oil system are shown in Figure 3.22 and Figure 3.23.

In Figure 3.22, the external AC electric fields which were applied to the sample had the same frequency of 1 kHz, but the magnitudes of the applied fields were changed in the range of 100 V/mm to 1000 V/mm. At low voltage (100V/mm) of the applied electric field, visible chains began to form around 10 mixtures after application of the electric field. More chains were formed as the duration time increased. As the voltage of the applied electric field increased, clearer and denser chains were formed. For all voltages of the applied electric fields, the alignments achieved the equilibrium state after 1 hour application of the electric field. Therefore, the chain formation of the nanoparticles dispersion is dependent on the magnitude and duration of the electric field.

In Figure 3.23, the external AC electric field applied to the sample was 1000 V/mm. The frequencies of the applied electric fields were ranged from 100 mHz to 1 kHz. The chains formed by the nanoparticles became clearer as the electric field duration time increases at all frequencies of the electric fields. From Figure 3.21, it was also indicated that the gap between the chains became thinner and the number of visible chains increased as the frequencies of the electric fields increased. Higher frequency and longer duration of the applied electric fields could improve the alignment orientation under the same applied field magnitude. The overall trend of variation of particle alignments is consistent with the previous results of TiO_2 and BSTO system. The results prove that nanoparticle alignment and chain formation are a function of the magnitude, frequency and duration time of the external applied electric field.
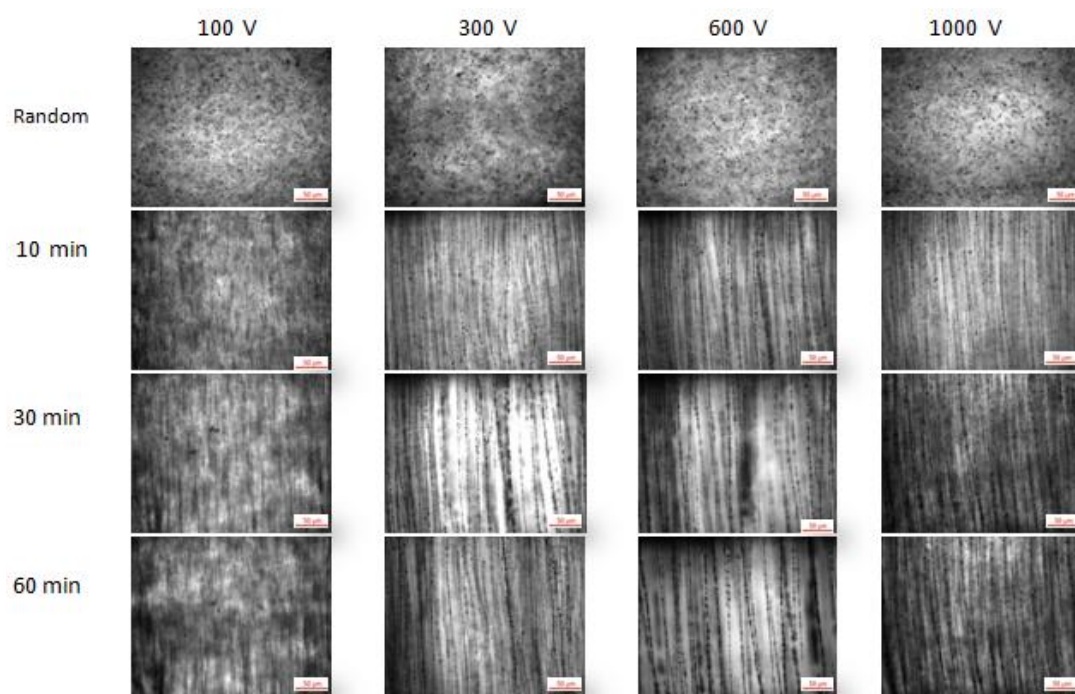
Figure 3.22   Optical microscopy images of 1 wt% BaTiO$_3$ nanowires-oil system under

an applied electric field of 1 kHz, different magnitudes (100 V/mm to 1000 V/mm) and

different time intervals (0-1 hour). The scale bar is 50 μm.
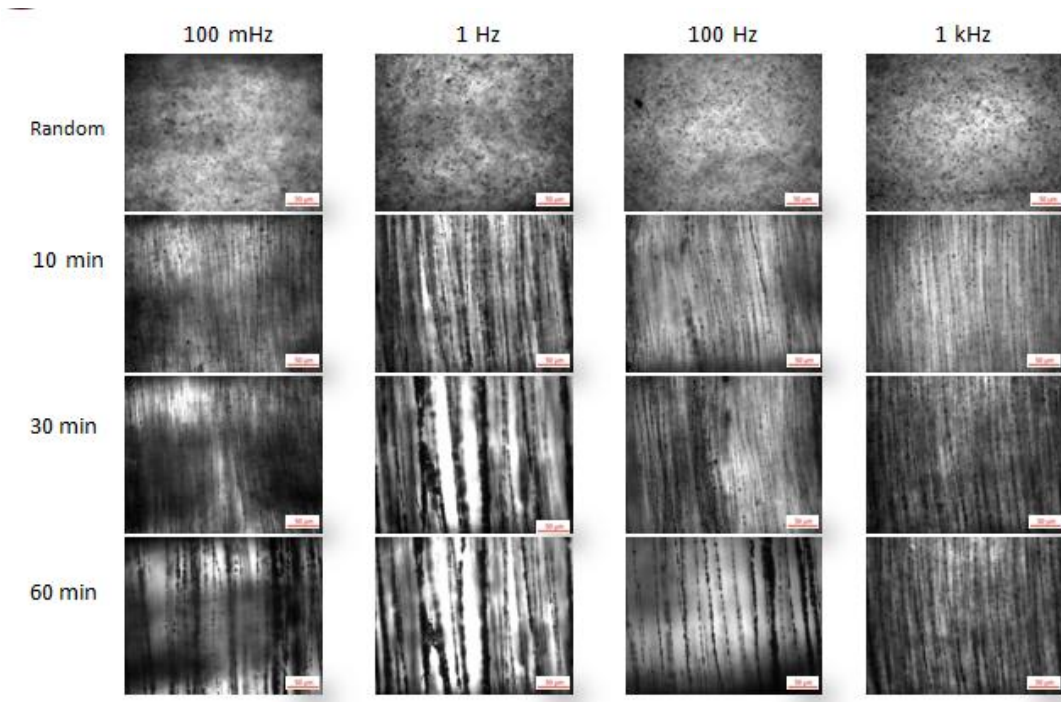
Figure 3.23   Optical microscopy images of 1 wt% BaTiO$_3$ nanowires-oil system under an applied electric field of 1000 V/mm, different frequencies (100 mHz to 1 kHz) and different time intervals (0-1 hour). The scale bar is 50 μm.

3.5.2 In-situ Measurement of Dielectric Constant

Figure 3.24 and 3.25 show the dielectric constant values of 1 wt% BaTiO$_3$ nanowires-oil dispersion in random case and under different applied electric fields. Figure 3.24 shows the dielectric constant values for samples aligned with 100 V/mm to 1000 V/mm electric fields at 1 kHz for 1hour. From Figure 3.25, as the frequency of the measurement field increased, the effective dielectric constant first decreased then kept flat. The effective dielectric constant of the sample in random state was below 3. As

the magnitude of the applied electric field increases, this parameter was enhanced significantly. The results show that the effective dielectric constant of $BaTiO_3$ nanowires-oil dispersion can reach up to 6 for samples aligned at electric field magnitude of 1000 V/mm, and 1kHz frequency. In the results shown in Figure 3.25, the magnitude of the applied electric field was kept as 1000 V, while the frequency of the field was changed from 100 mHz to 1 kHz. From Figure 3.25, the frequency is another important factor to the effective dielectric constant. As the frequency of the applied field increased, the effective dielectric constant increased noticeably. In order to study the dependence of the effective dielectric constant on the concentration of $BaTiO_3$ nanowires-oil dispersion, we repeated the experiment for 5 wt% $BaTiO_3$ nanowires-oil dispersion, whose result is shown in Figure 3.26. The applied field was the same for that in Figure 3.25, with magnitude of 1000 V/mm, at frequency range from 100 mHz to 1 kHz, and with duration time of 1 hour. From Figure 3.26, the effective dielectric constant of high concentration sample was dependent on the measurement field frequency and applied field frequency in the same way as the parameter of the low concentration sample. The maximal effective dielectric constant of the 5 wt% $BaTiO_3$ nanowires-oil dispersion was achieved when applied with 1000 V field at 1 kHz. The maximal parameter is around 10. Therefore, increasing concentration is another possible way to enhance the effective dielectric constant. The maximal effective dielectric constant of 5 wt% $BaTiO_3$ nanowires-oil dispersion is higher than that of 5 wt% BSTO-oil dispersion and much higher than any TiO_2-oil dispersion prepared before. Figure 3.27 shows the dielectric loss of 5 wt% $BaTiO_3$ nanowires-oil dispersion. At low

measurement frequencies (less than 10 kHz), the dispersions had relative high dielectric

loss and the loss was increased as frequency of electric field increased. However, all the

dispersions had very low dielectric loss when the measurement frequency was large than

10 kHz.

This result proves that the shape of colloid particles influences the effective

dielectric constant along with the concentration of particles. High aspect ratio $BaTiO_3$

nanowires could achieve high effective dielectric constant and can satisfy our

requirements for the switchable antenna.
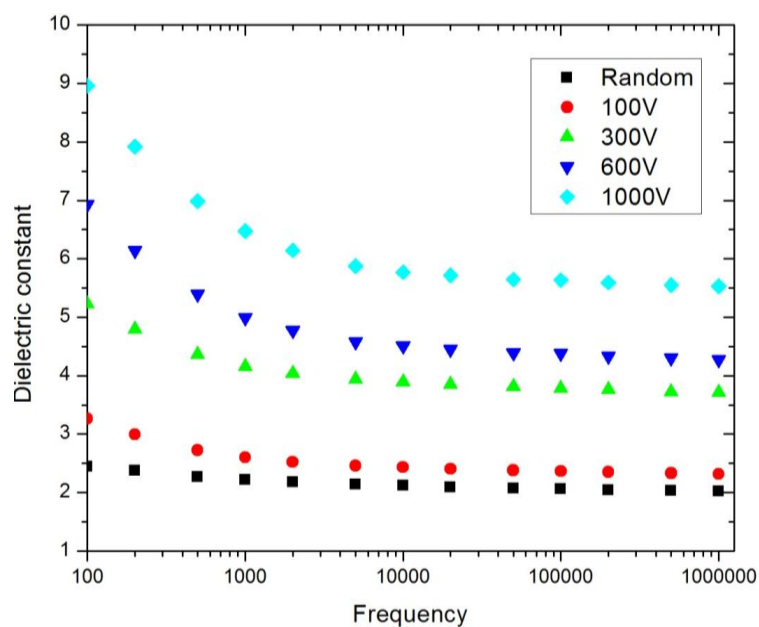
Figure 3.24   In-situ dielectric constant of 1 wt% $BaTiO_3$ nanowires-oil under an

applied electric field of 100 V/mm to1000 V/mm, 1 kHz and 1 hour.
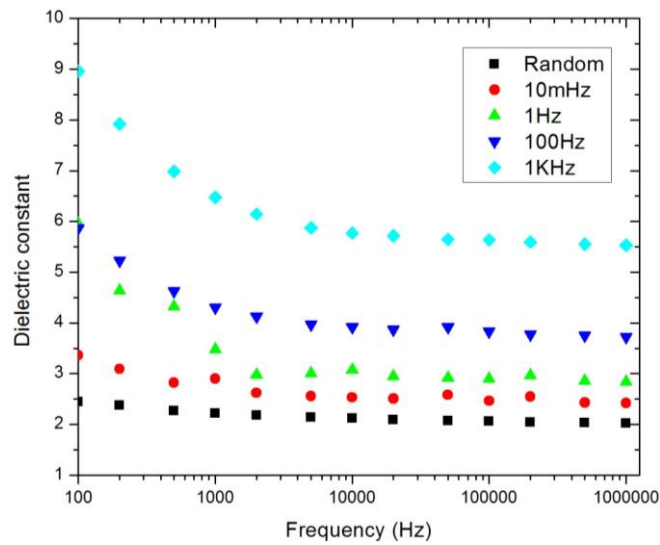
Figure 3.25   In-situ dielectric constant of 1 wt% BaTiO$_3$ nanowires-oil under an

applied electric field of 1000 V/mm, 100 mHz to1 kHz and 1 hour.
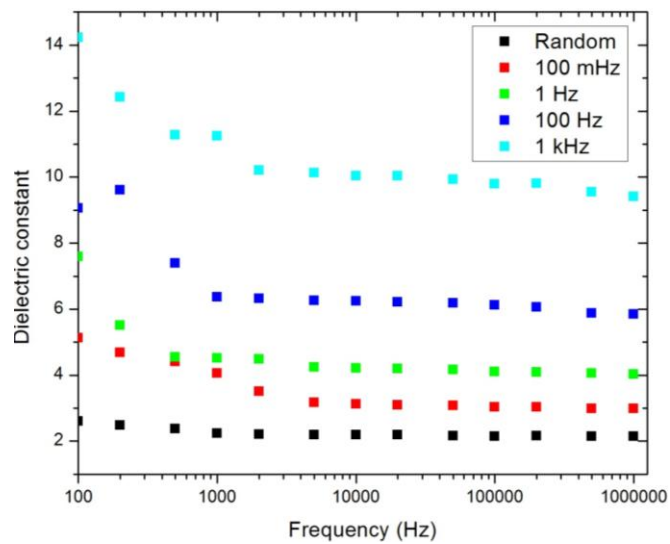
Figure 3.26   In-situ dielectric constant of 5 wt% BaTiO$_3$ nanowires-oil under an

applied electric field of 1000 V/mm, 100 mHz to1 kHz and 1 hour.
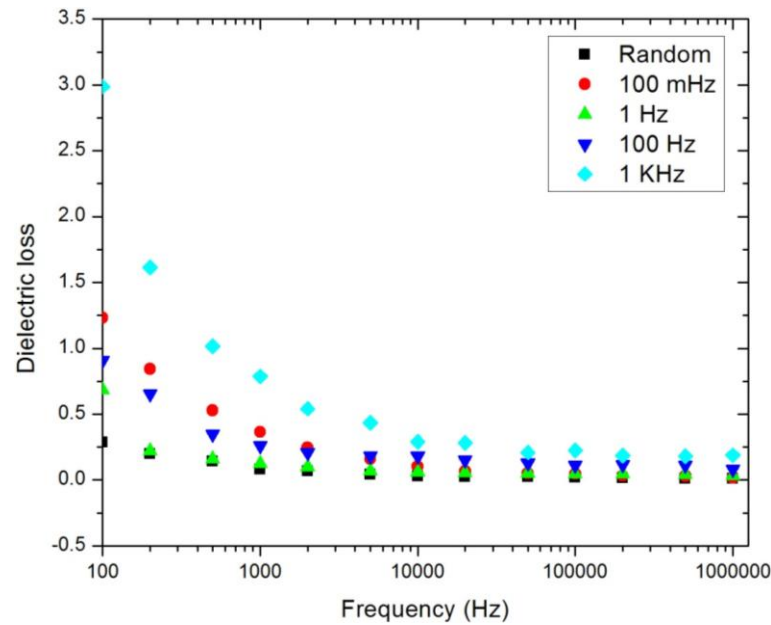
Figure 3.27　　In-situ dielectric loss of 5 wt% BaTiO$_3$ nanowires-oil under an applied

electric field of 1000 V/mm, 100 mHz to1 kHz and 1 hour.

3.6　　Modeling Using Maxwell-Garnett Mixing Rule for BaTiO$_3$

Maxwell-Garnett mixing rule was used to model the dielectric property of the BaTiO$_3$ colloidal base materials. The aligned orientation was considered at the beginning for simple, the schematic map of the simulation in the case of aligned orientation was shown in Figure 2.9 b. The principles presented in Equation (2.2)-(2.8) were used to simulate the effective dielectric constant using Matlab software. The aspect ratio of prepared BaTiO$_3$ nanowires was around 10-20. The initial condition was assumed as, dielectric constant of BaTiO$_3$ was 1500, weight ratio was 0-20%, and aspect ratio was 10-20. The 3-D simulation results for effective dielectric constant of BaTiO$_3$ nanowires are shown in Figure 3.28 (a). Consequently, another set of 3-D simulation was

performed using another group of input variables including dielectric constant of particles in the range of 1000-2000, weight percent 5%, and aspect ratio 10-20. The simulation results for effective dielectric constant of $BaTiO_3$ nanowires based on the second input variables are shown in Figure 3.28 (b). The maximum effective dielectric constant of $BaTiO_3$ nanowires dispersion can be as high as 12. The experimental results performed in previous section showed that the effective dielectric constant of $BaTiO_3$ nanowires-oil dispersion was around 6 when applied with external AC electric field. This value was higher than the simulation result which was less than 4 for 1 wt% dispersion. The reason is that the aligned orientation is an ideal case. Particles in the ideal situation do not touch each other to form chains, which was complicated to realize in the actual situation.

The variation of effective dielectric constant as a function of aspect ratio α (alpha) of particles and volume fraction is plotted in Figure 3.29. The dielectric constant of $BaTiO_3$ was assumed 1500. From Figure 3.29, the relationship between the effective dielectric constant and volume fraction tended to be linear as α increased. The aligned orientation can be equivalent to chain alignment if the infinite cylinder aligned particles were considered or the aspect ratio of nanowires was large enough (at least >100). Schematic diagram of aligned orientation and chain alignment is shown in Figure 3.30. In the case of chain alignment, the effective dielectric constant had simple linear relationship with volume fraction and dielectric constant of $BaTiO_3$ nanowires.

The effective dielectric constant of 1 wt% and 5 wt% $BaTiO_3$ nanowires-oil dispersion from experiments and simulations were compared and are shown in Figure

3.31. Two different dielectric constant of $BaTiO_3$ were used to compare. 500 is dielectric constant of cubic structure $BaTiO_3$, and 1500 is dielectric constant of tetragonal structure $BaTiO_3$. From the results, the simulated results using the chain alignment model (infinite cylinder aligned particles) was significantly higher than that using aligned orientation model, which could be expected because the chain alignment is an optimal extension from the case of aligned orientation, as explained in Figure 3.30. In the concentration of 1 wt% of the $BaTiO_3$ nanowires-oil dispersion, the simulated results using chain alignment model comparable with the experimental results. In opposite, the simulated effective dielectric constant of 5 wt% $BaTiO_3$ nanowires-oil dispersion using chain alignment model is 16, which is higher than the experimental result. The reason is that chain alignment of the $BaTiO_3$ nanowires is an ideal case, which is even harder to realizable in the high concentration sample. Because the chain alignment model didn't consider the effect of diameter of particles, gaps between particles or other factors. Therefore, the experimental result of effective dielectric constant of the high concentration sample is smaller than the simulated result using chain alignment model. The experimental results from both concentration samples were significantly larger than the simulated result using aligned orientation model though.
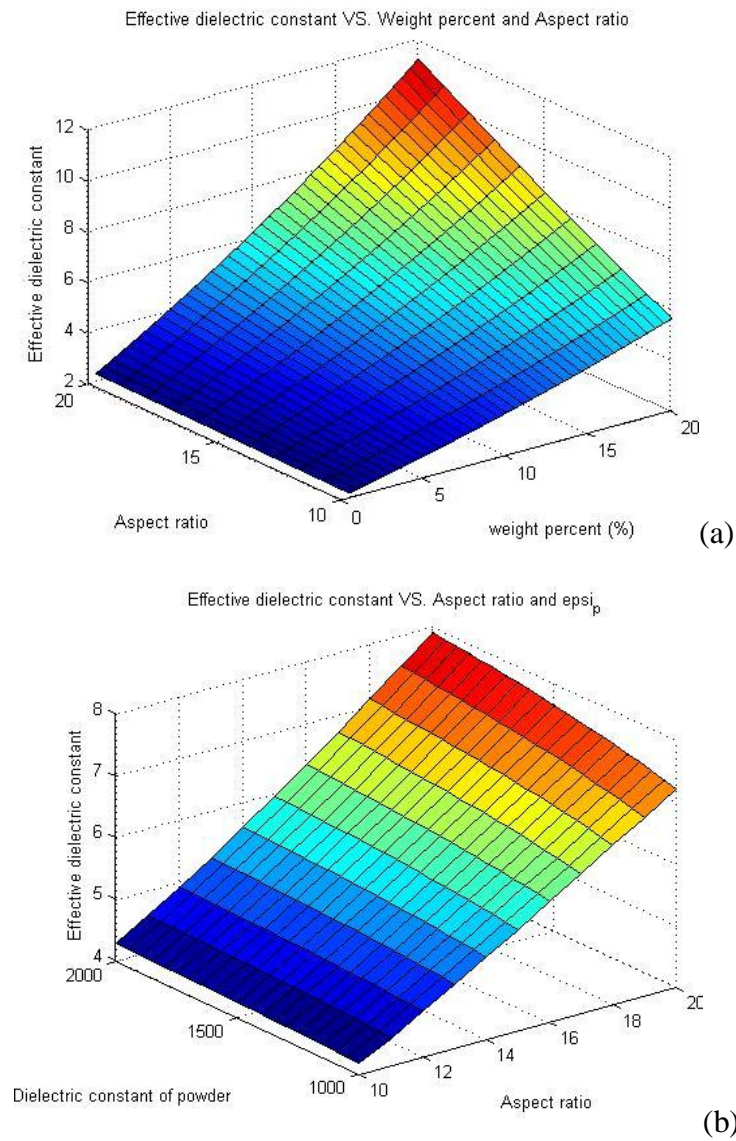
Figure 3.28   3-D simulation of BaTiO$_3$ using Maxwell-Garnett Mixing Rule. (a)

Dielectric constant of particles is 1500, weight percent is 0-20%, and aspect ratio is 10-

20, and (b) dielectric constant of particles is 1000-2000, weight percent is 5%, and

aspect ratio is 10-20.
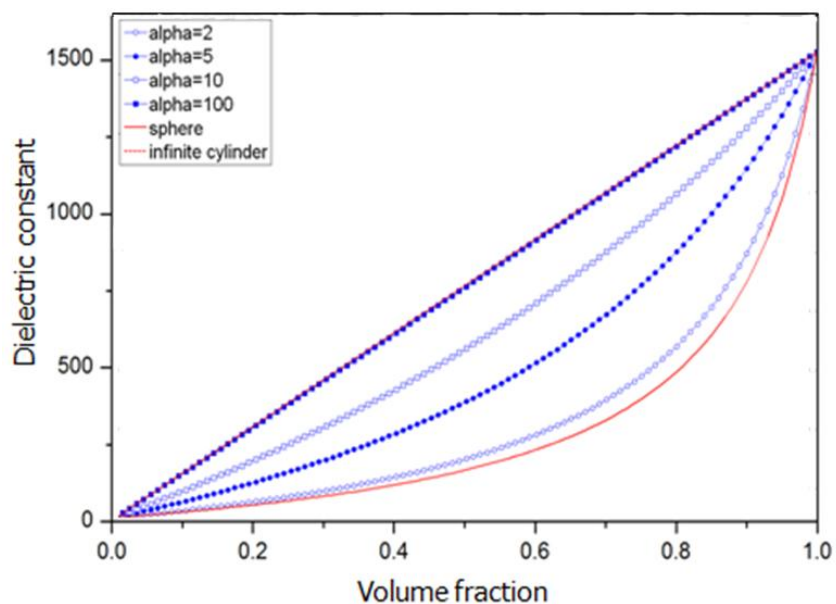
Figure 3.29   Effective dielectric constants as a function of aspect ratio of particles and

volume fraction of dispersion.
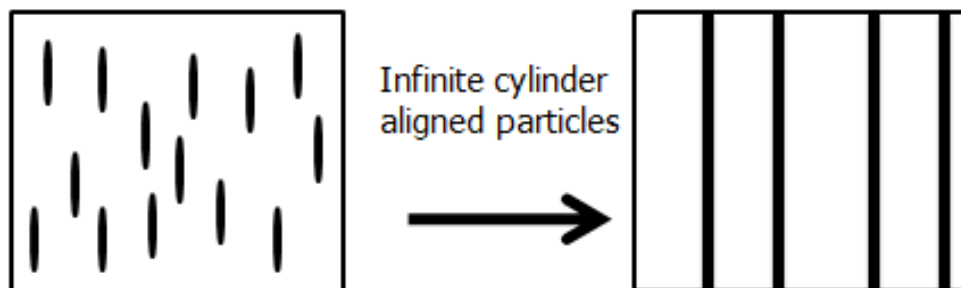
Figure 3.30   Schematic diagrams for aligned orientation and chain alignment.
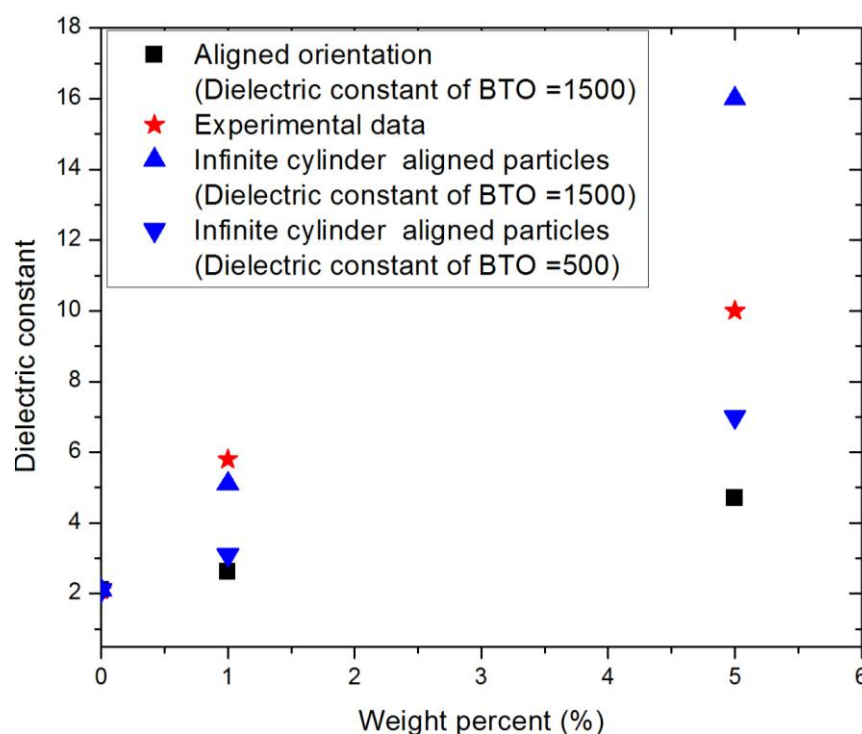
Figure 3.31   Comparison of dielectric constant of experimental and simulation results

3.7   BaTiO$_3$-Epoxy Nanocomposites

The method to disperse BaTiO$_3$ nanowires in epoxy polymer has been described in Section 2.5. The 0.1 wt% BaTiO$_3$-epoxy nanocomposites was prepared using the described method and its OM image is shown in Figure 3.32 (a). From the image shown in 3.32 (a), the BaTiO$_3$ nanowires are evenly dispersed in epoxy polymer, with few if any agglomerates. Using this dispersion method, the BaTiO$_3$ with concentration up to 1 wt% could be dispersed in epoxy polymer evenly. The OM images of 0.25 wt%, 0.5 wt% and 1 wt% BaTiO$_3$-epoxy nanocomposites are shown in Figure 3.32 (b), (c), and (d), respectively. From Figure 3.32 (b), there were only few large agglomerates at 0.25 wt% BaTiO$_3$-epoxy nanocomposites. In Figure 3.32 (c), when the concentration of

BaTiO$_3$ went up to 0.5 wt%, noticeable amount of large agglomerates started to appear. As the concentration of BaTiO$_3$ increased to 1 wt% in the epoxy dispersion, which is shown in Figure 3.32 (d), the size and number of agglomerates increased significantly. Comparing Figure 3.32 (b), (c) and (d), we can conclude that as the concentration of BaTiO$_3$ increased, it was difficult to separate the BaTiO$_3$ agglomerates from the single nanowires and to obtain uniform homogenous epoxy polymer dispersion.

External AC electric field was applied to study the alignment of BaTiO$_3$-epoxy dispersions before curing. A summary of OM images of 0.1 wt% BaTiO$_3$-epoxy dispersions applied with the external electric fields for different duration are shown in Figure 3.33. Applied field was 1000 V/mm, at 1 kHz. From Figure 3.33, after AC electric field was applied for 5 minutes, BaTiO$_3$ particles in epoxy polymer dispersion began to rotate and form short chains parallel to the electric field. After applied with the electric field for 1 hour, the BaTiO$_3$ particles in epoxy polymer dispersion only form short chains were compared to the alignment of the BaTiO$_3$ particles in oil dispersion under external electric field, the chain formation shown in Figure 3.33 is much slower and more difficult. The reason for the difference of the chain formation of the BaTiO$_3$ particles in oil and epoxy dispersions should be the higher viscosity of epoxy dispersion than oil.
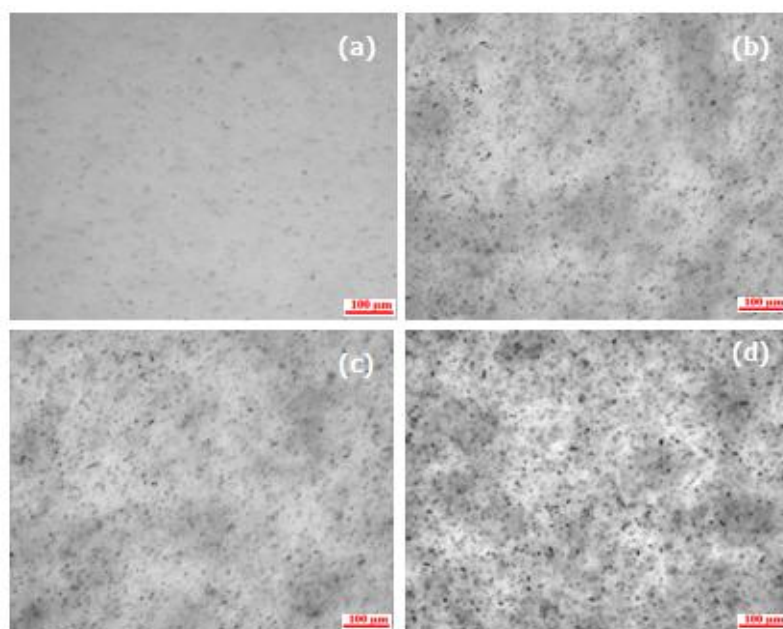
Figure 3.32   OM images of different concentrations BaTiO$_3$-epoxy nanocomposites. (a)

0.1 wt%, (b) 0.25 wt%, (c) 0.5 wt%, and (d) 1 wt%.
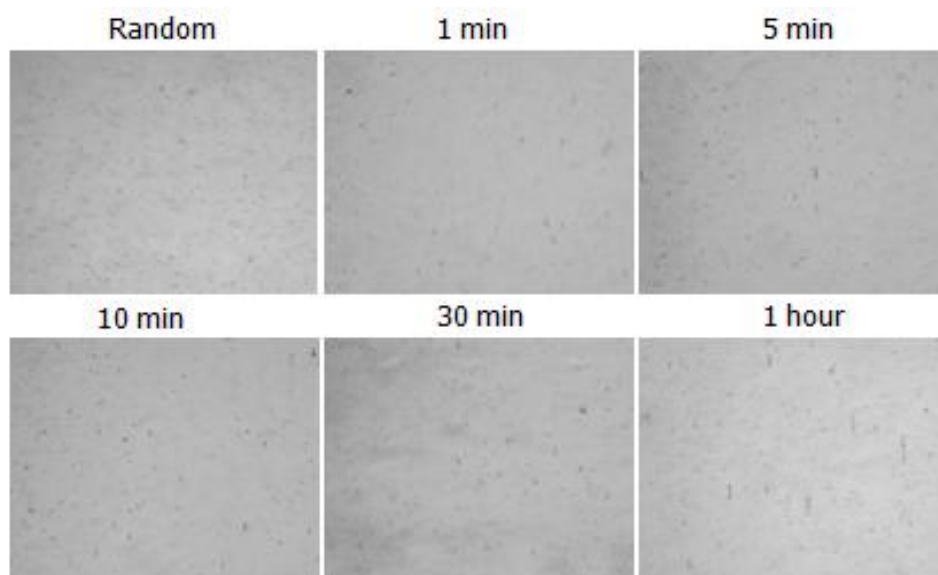
Figure 3.33   OM images of 0.1 wt% BaTiO$_3$-epoxy dispersions under an applied

electric field of 1000 V/mm, 1 kHz and different time intervals (0-1 hour).

In order to further investigate the effect of dispersion viscosity on the alignment of $BaTiO_3$ particles, we measured the alignment of $BaTiO_3$-epoxy dispersions in the environmental chamber at high temperature. It has been proved that the viscosity of epoxy dispersion would be reduced at high temperature. The OM images of 0.1 wt% $BaTiO_3$-epoxy dispersions under applied fields with different magnitude for an hour in chamber at different temperature are shown in Figure 3.34. In Figure 3.34 (a), and (b), the applied field was 100 V/mm for both samples, yet the temperature for alignment were 70 ℃ to 120 ℃, respectively. Comparing the OM images of the samples shown in Figure 3.34 (a), and (b), it seems that as the temperature increased, the chain of particles were easier to form. The change between the chains of particles shown in Figure 3.34 (a), and (b) is not significant, probably because the temperature increase was not sufficient to obviously change the viscosity. From Figure 3.34 (b) and (c), at the same temperature, when the applied field was increased from 1000 V/mm to 2000 V/mm, much more chains of the particles were observed, and the chains became a little longer. Therefore, the increases of both temperature and magnitude of applied field would result in more short chains formation inside $BaTiO_3$-epoxy dispersions. However, there was no long chain alignment formed even in the dispersion applied with electric field of 2000 V/mm at 120 ℃. $BaTiO_3$ nanowires might not obtain chain alignment in epoxy polymer due to the high viscosity.

Figure 3.34   OM images of 0.1 wt% BaTiO$_3$-epoxy dispersions (a) 1000 V/mm, 1 kHz, 70 ℃, and 1 hour, (b) 1000 V/mm, 1 kHz, 120 ℃, and 1 hour, and (c) 2000 V/mm, 1 kHz, 120 ℃, and 1 hour.

CHAPTER IV

SUMMARY AND CONCLUSIONS

The objective of this thesis is to develop high dielectric constant nanoparticle dispersions for switchable aircraft antenna systems. To fulfill this objective, the effect of AC electric field on the alignment of TiO_2 and $BaTiO_3$ in dielectric oil medium was studied.

In order to develop an appropriate nanoparticle dispersion that has high effective dielectric constant to satisfy our requirement, we focused on preparing and characterizing dispersions of TiO_2 in oil because TiO_2 is commercially available and has a relatively high dielectric constant. Two types of TiO_2 were used, titania nanowhiskers (anatase, 10 nm x40 nm) and titania acicular (FTL-100, 200 and 300). For both TiO_2, a combination of mechanical stirring and bath sonication was used to process random colloidal-based dispersions. Different concentrations of even TiO_2 dispersions were prepared. TiO_2 dispersions were successfully manipulated using an AC electric field. Alignment was observed under the transmission OM to monitor the change in microstructure. Under application of electric field, TiO_2 particles rotated and aligned in the direction of electric field. The chain formation of the nanoparticles dispersion was dependent on the magnitude, frequency and duration of the electric field. Dielectric constant was measured to qualify and characterize the alignment of the nanoparticles. Our dielectric results from both TiO_2 samples indicated that the alignment conditions, such as electric field frequency and duration, have substantial impact on the dielectric

properties. For 0.2 wt% titania nanowhiskers-oil dispersion, the maximal effective dielectric constant was around 2.4, which was found at an applied electric field of 1000 V/mm at 1 kHz. For 0.2wt % FTL-100-oil dispersion, the effective dielectric constant increased up to around 2.8 under the same applied field. Compared with titania nanowhiskers-oil system, the same concentration of FTL-100-oil dispersion exhibited higher effective dielectric constant. Consequently, 0.2wt%, 1wt%, 2.5wt%, and 5wt% of FTL-100-oil dispersions were prepared. Under the application of 1000 V/mm electric field at 1 kHz, the dielectric constant increased from 2.8 to 3.4 when the nanoparticles content increased from 0.2wt% to 5wt%. These results indicated that the concentration of dispersions plays an important role in the variation of effective dielectric constant along with magnitude, frequency and duration of applied electric field. Unfortunately, the high concentration of TiO_2-oil dispersion is limited by processing challenges; it is difficult to obtain homogeneous dispersion at concentration higher than 10wt%.

Modeling using Maxwell-Garnett mixing rule was used to estimate the dielectric property of the colloidal-based materials. The results showed that the maximum effective dielectric constant of TiO_2-oil solution is much less than 6 even in the case of 20 aspect ratio, 100 dielectric constant and 20 wt% dispersion. This result demonstrated that TiO_2 cannot provide high enough dielectric constant as is needed for the switchable antenna system. Therefore, we switched our focus to $BaTiO_3$ colloidal-based materials, because $BaTiO_3$was reported to exhibits a much higher dielectric constant than TiO_2. The effective dielectric constants for different shapes of $BaTiO_3$ were then estimated using Maxwell-Garnett mixing rule, and results indicated that the requirements for

colloidal-based materials of high effective dielectric constant could be satisfied by BaTiO$_3$ particles.

BSTO spheres were characterized because they have similar dielectric constant as BaTiO$_3$. 1 wt% and 5 wt% BSTO spheres in oil dispersions were prepared for our experiment. Maximum effective dielectric constants achieved were 3.5 and 5 for 1 wt% and 5 wt% BSTO spheres respectively, under a 1000 V/mm, 1 kHz and 1 hour applied electric field. The values were higher than for the same concentration of titania FTL-100-oil dispersion. Therefore, BSTO exhibits the highest effective dielectric constant within the commercially available materials. However, this effective dielectric constant of BSTO is still not high enough for our goal.

Proving that none of the commercially available materials worked for our requirement of high and tunable dielectric dispersion, we decided to synthesize high aspect ratio BaTiO$_3$ nanowires. Molten salt method was chosen; it is a method similar to that of the solid-state reaction, but the salt plays an important role by intervening in the formation reaction. This method is a relatively easy and low-cost method, and it has other advantages such as processing at relatively low temperatures and resulting in high purity oxides.SEM, XRD, and EDS mapping were used to characterize the as-preparedBaTiO$_3$ nanowires. The images indicated that suitable post-processing, including centrifuge and water wash, played an important role in purifying the product. High purity samples could be obtained by centrifuging 20 times and water washing 50 times. We also learned thatsynthesizingBaTiO$_3$nanowires using a quartz crucible would lead to a second-phase product Ba$_2$TiSi$_2$O$_8$ (BTS). Thus zirconia crucible was used to

avoid producing BTS. At last, single crystalline, high purity and high aspect ratio BaTiO$_3$ nanowires were successfully synthesized. The nanowires had diameters ranging from 100 nm to 300 nm, and lengths ranging from 1.5 μm to 5 μm.High aspect ratio BaTiO$_3$ nanowires using molten salt method exhibit very high sensitivity to annealing temperature, annealing time and the choice of TiO$_2$ precursors. Single crystal, high purity, and high aspect ratio BaTiO$_3$ nanowires could be synthesized only under specific conditions: using TiO$_2$anatasenanospheres with a15 nm diameter, choosing an annealing time of 3.5 hours, and an annealing temperature of 820 ℃. For example, short aspect ratio BaTiO$_3$ nanowires were obtained if TiO$_2$rutile nanoparticles were used as the precursors, while nanocubes, instead of nanowires, would be synthesized if the annealing temperature not high enough or annealing time not long enough. Finally, nanoflowers were produced if the annealing temperature was more than 950 ℃. Therefore, successful production of BaTiO$_3$ nanowires depended on processing time, processing temperature and the precursor crystalline phase.

The effective dielectric constant ofBaTiO$_3$nanowires-oildispersionwas characterized for different alignment conditions. Our results indicated that 1 wt% BaTiO$_3$ nanowires-oil dispersion could reach an effective dielectric constant of around 6, while the effective dielectric constant of 5 wt% BaTiO$_3$ nanowires-oil dispersion reached a value of 10, at 1 kHz, 1000 V/mm and 1 hour applied electric field. This result was higher than that of 5 wt% BSTO-oil dispersion and much higher than any TiO$_2$-oil dispersion. Therefore, BaTiO$_3$ nanowires are good candidates to satisfy our requirements for the switchable antenna. Maxwell-Garnett mixing rule was also used to model the

dielectric property of the $BaTiO_3$colloidal-based materials. It is noted that the aligned orientation can be equivalent to chain alignment if the aligned particles are considered to be infinite cylinders or the aspect ratio of nanowires was large enough (at least >100).With this assumption, the effective dielectric constant had a simple linear relationship with volume fraction and dielectric constant of $BaTiO_3$nanowires. Comparing the calculated results of effective dielectric constant with the experimental results, we found that the experimental results of the high concentration sample were smaller than the calculated results using chain alignment model but larger than the calculated result using aligned orientation model. The differences between the experimental results and calculated results using the two models are reasonable considering the assumption made by each model.

Next, 0.1 wt%, 0.25 wt%, 0.5 wt% and 1 wt% $BaTiO_3$-epoxy nanocomposites were prepared and characterized. The $BaTiO_3$ particles in epoxy polymer dispersion only formed short chains comparing to the $BaTiO_3$ particles in oil dispersion under the same external electric field. Besides, the chain formation in $BaTiO_3$-epoxy nanocomposites was much slower and more difficult to attain. There was no long chain alignment formed even in the dispersion applied with electric field of 2000 V/mm at 120 ℃. The high viscosity of epoxy polymers most likely interfered with the $BaTiO_3$nanowires rotation and translation, preventing proper chain alignment.

Recommendations for future work on this topic are described in the following bullets: 1) the present study has focused on characterization of different alignments of high dielectric particles in oil. A follow-up study can focus on dispersing high dielectric

particles, especially high aspect ratio $BaTiO_3$ nanowires, in other high dielectric mediums, which have higher dielectric constant and lower dielectric loss than oil. 2) Regarding theoretical analysis, the next step should focus on the different mechanisms associated with electric field-driven manipulation and detailed analysis of various electrokinetic and other forces. This will enable us to understand the principle of manipulation more in-depth, and to design materials with specific desired properties. 3) It is advised to focus on processing high concentration $BaTiO_3$-polymer nanocomposites and reduce the viscosity effectively for successful electric field manipulation. Characterization of the materials at high frequency and coaxial line experiment are also needed.

REFERENCES

[1]   Y.X. Leng , P. Yang , J.Y. Chen , H. Suna, J. Wanga, G.J. Wana, Y. Lengc, P.K. Chu, *Thin Solid Films,* **2002**, 420, 408,.

[2]   S. Sankar, K. G. Gopchandran, *Cryst.Res.Technol.,* **2009**, 44, 989.

[3]   J. Winkler, *Titanium Dioxide*. Hannover, Germany, Vincentz Network, **2003**.

[4]   V.P. Godbole, Gil-Sung Kim, M.A. Dar, Hyung-Shik Shin, *Electrochimica Acta,* **2006,** 52, 1781.

[5]   W. Maison, R. B. Heimann, S. Phanichphant, *Journal of the European Ceramic Society,* **2003**, 23, 127.

[6]   G. H. Haertling, *J. Am. Ceram. Soc,* **1999**, 82797, 818.

[7]   L. L. Hench, L. K. West, *Principles of Electronic Ceramics*, John Wiley & Sons, Inc., **1990**.

[8]   G. K. Sahoo, MTech Master dissertation, Department of Ceramic Engineering, National Institute of Technology, Rourkela, India, Rourkela, **2009**.

[9]   H.F. Kay, P. Vousden, *Phil. Mag. Series,* **1949**, 40, 1019.

[10]   B. Jaffe, W. R. Cook, Jr, and H. Jaffe, *Piezoelectric ceramics*, Cleveland, Ohio, William R. Cook, Jr. and Hans Jaffe Gould Inc., **1971**.

[11]   W. J. Merz, *Phys. Rev.,* **1949**, 76, 1221.

[12]   W. Cao, L. E. Cross, *Physical Review B,* **1991,** 44, 5.

[13]   T. J. Shen, Master of Science Master dissertation, Materials Science and Engineering, University of Cincinnati, **2006**.

[14]   W.D. Kingery, H. K. Brown, D.R. Uhlmann, *Introduction to Ceramics, 2nd edition*, New York, John Wiley & Sons, **1976**.

[15]   H. Yanagida, K. Koumoto, M. Miyayama, *The Chemistry of Ceramics*, New York, Wiley, **1996**.

[16]   M. Sitti, "Survey of Nanomanipulation Systems," presented at the IEEE-Nanotechnology Conference, Maui, USA, **2001**.

[17]   M. Sitti, H. Hashimoto, *IEEE/ASME Transactions on Mechatronic,* **2000**, 5.

[18]   A. Kyprianou, N. Loucaides, N. Polydorides, G. Georghiou, C. Charalambous, C. Doumanides, *Int. J. Nanomanufacturing,* **2007**, 1.

[19]   W. J. Li, N. Xi, W. K. Fung, T. S. Wong, *Nanorobotics and. Nanomanipulation* vol. 7, American Scientific Publishers, **2004**.

[20]   M. Trau, D. A. Saville, I. A. Aksay, *Science,* **1996**, 272, 706.

[21]   B. T. Holland, C. F. Blanford, A. Stein, *Science,* **1998**, 281, 538.

[22]   A. A. Zakhidov, R. H. Baughman, Z. Iqbal, C. Cui, I. Khayrullin, S. O. Dantas, J. Marti, V. G. alchenko, *Science,* **1998**, 282, 897.

[23]   T. Mukaiyama, K. Takeda, H. Miyazaki, Y. Jimba, M. Kuwata-Gonokami, *Phys. Rev. Lett.,* **1999**, 82, 4623.

[24]   A. L. Rogach, N. A. Kotov, D. S. Koktysh, J. W. Ostrander, G. A. Ragoisha, *Chem. Mater.,* **2000**, 2721.

[25]   R. W. O'Brien, D.W.Cannon, W.N. Rowlands, *J. Colloid Interface Sci.,***1995**, 406.

[26]   S. Y. Lin, J. G. Fleming, D. L. Hetherington, B. K. Smith, R. Biswas, K. M. Ho, M. M. Sigalas, W. Zubrzycki, S. R. Kurtz, Jim Bur, *Nature,* **1998**, 394, 251.

[27]   A. Yethiraj, A. van Blaaderen, *Nature,* **2003**, 421, 513.

[28]   K. D. Hermanson, S. O. Lumsdon, J. P. Williams, E. W. Kaler, O. D. Velev, *Science,* **2001**, 294, 1082.

[29]   P. Bahukudumbi, W. N. Everett, A. Beskok, M. A. Bevan, G. H. Huff, D. Lagoudas, Z. Ounaies, *Appl. Phys. Lett.,* **2007**, 90, 224102.

[30]   M. Abe, A. Yamamoto, M. Orita, T. Ohkubo, H. Sakai, N. Momozawa, *Langmuir,* **2004**, 20, 7021.

[31]   S. O. Lumsdon, E. W. Kaler, J. P. Williams, O. D. Velev, *Appl. Phys. Lett.,* **2003**, 82, 949.

[32]   S. O. Lumsdon, E. W. Kaler, O. D. Velev, *Langmuir,* **2004**, 20, 2116.

[33]   O. D. Velev, K. H. Bhatt, *Soft Matter,* **2006**, 2, 738.

[34]   O. D. Velev, S. Gangwala, D. N. Petsev *Annu. Rep. Prog. Chem., Sect. C,* **2009**, 105, 213.

[35]   C. Park, J. Wilkinson, S. Banda, Z. Ounaies, K. E. Wise, G. Sauti, P. T. Lillehei, J. S. Harrison, *J. Polym. Sci., Part B: Polym. Phys.,* **2006**, 44, 1751.

[36]   S. Banda, Ph.D dissertation, Aerospace Engineering, Texas A&M University, College station, **2008**.

[37]   I. MacLaren, C. B. Ponton, *J. Eur. Ceram. Soc.,* **2000**, 20, 1267.

[38]   M. M. Vijatović, J. D. Bobić, B. D. Stojanović, *Science of Sintering,* **2008**, 40, 155.

[39]   S. Y. Kihun, K. D. Heon, *Journal of Materials Science,* **1998**, 33, 2977.

[40]   M. Boulos, *Solid State Ionics,* **2005**, 176, 1301.

[41]   L. Simon-Seveyrat, Y. Emziane, B. Guiffard, D. Guyomar, *Ceram. Int.,* **2007**, 33, 35.

[42]   D. K. Kim, *J. Mater. Sci. Technol.,* **2007**, 23, 655.

[43]   L. Wang, D Xue, H. Kang, and C. Liu,, *J. Alloys Compds.,* **2007**, 440, 78.

[44]   L. B. Kong, *Journal of Alloys and Compounds,* **2002**, 337, 226.

[45]   W.S. Cho, *J. Phys. Chem. Solids,* **1998**, 59, 659.

[46]   S.B. Deshpande, Y.B. Khollan, H.S. Potdar, *Journal of Electroceramics,* **2005**, 15, 103.

[47]   M. Cernea, *Journal of Optoelectronics and Advanced Materials,* **2005**, 7, 3015.

[48]   Y. W. Chen, *Ind. Eng. Chem. Res.,* **2003**, 42, 473.

[49]   H.S. Potdar, S.K. Date, *Materials Chemistry and Physics,* **1999**, 58, 121.

[50]   P. K. Gallagher, *J. Mater. Res.,* **1995**, 10, 945.

[51]   F. Fernandez, C. Moure, *Journal of Materials Science Letters,* **1992**, 11, 1188.

[52]   S. Lee, J. Yun, H. Kwon, G.L. Messing, Byungsei Jun, *Materials Letters,* **2004**, 58, 2932.

[53]   V. Gorokhovsky, T. Sa ńches-Monjara ś, G. Vargas-Gutierrez, *Materials Letters,* **2004**, 58, 2227.

[54]   P. Afanasiev, C. Geantet, *Coordination Chemistry Reviews,* **1998**, 178, 1725.

[55]   C. K. Yoon, D. H. Kang, *Journal of Materials Science,* **1998**, 33, 2977.

[56]   Y. Mao, *J. Am. Chem. Soc.,* **2003**, 125, 15718.

[57]   J. Yuh, W. M. Sigmund, *J Sol-Gel Sci Techn,* **2007**, 42, 323.

[58]   J. J. Urban, Q. Gu, H. Park, *J. am. Chem.Soc,* **2002**, 124, 1186.

[59]   C. Jiang, Y. Wang, K. Koumoto, *Crystal Grouth &Design,* **2007**, 7, 2713.

[60]   Z.Y. Liang, C. Zhang, B. Wang, L. Kramer, *Material Science and Engineering: A,* **2004**, 365, 228.

[61]   E. S. Moghbelli, Y. Lu, H. Jiang, W. Boo, H. J. Sue, *Polymer Engineering and Science,* **2009**, 483.

[62]   A. Sihvola, *Electromagnetic Mixing Formulas and Applications*, The Institution of Electrical Engineers, London, **2000**.

[63]   A. Sihvola, *Subsurface Sensing Technologies and Applications,* **2000**, 1, 393.

VITA

Name: Junjia Li

Address: Department of Aerospace Engineering, Richardson Building, Rm
                 1012, TAMU 3141, College Station, TX, 77843-3141

Email Address: lijunjiagreat@gmail.com

Education: B.S., Electrical Engineering, Nanjing University, China, 2005
                 M.S., Electrical Engineering, Nanjing University, China, 2008